

**The roles of intergeneration inheritance and intrageneration molecular dynamics in
shaping living cells**

by

Harsh Vashistha

BS-MS in Physics, IISER Bhopal, India, 2015

MS in Physics, University of Pittsburgh, 2018

Submitted to the Graduate Faculty of the
Dietrich School of Arts and Sciences in partial fulfillment
of the requirements for the degree of
Doctor of Philosophy

University of Pittsburgh

2021

UNIVERSITY OF PITTSBURGH

DIETRICH SCHOOL OF ARTS AND SCIENCES

This dissertation was presented

by

Harsh Vashistha

It was defended on

July 29, 2021

and approved by

Hanna Salman, Associate Professor, Department of Physics and Astronomy

Xiao-Lun Wu, Professor, Department of Physics and Astronomy

David Pekker, Assistant Professor, Department of Physics and Astronomy

Vladimir Savinov, Professor, Department of Physics and Astronomy

Robin E. C. Lee, Associate Professor, Department of Computational and Systems Biology

Thesis Advisor/Dissertation Director: Hanna Salman, Associate professor, Department of
Physics and Astronomy

Copyright © by Harsh Vashista

2021

The roles of intergeneration inheritance and intrageneration molecular dynamics in shaping living cells

Harsh Vashistha, PhD

University of Pittsburgh, 2021

We study two important dynamical processes in the bacterium *E. coli*. The first focuses on understanding how the inheritance of non-genetic components influences cellular properties and restrict heterogeneity in future generations. Heterogeneity in physical and functional characteristics of cells proliferates within an isogenic population due to stochasticity in intracellular biochemical processes and in the distribution of resources during divisions. Conversely, it is limited in part by the inheritance of cellular components between consecutive generations. The aim of this study is to characterize the dynamics of non-genetic inheritance in the simple model organism *E. coli*, and how it contributes to restraining the variability of various cellular properties. We describe the design of a novel microfluidic device that can trap sister cells in the same environment for 10s of generations. We introduce a new method for measuring proliferation of heterogeneity in bacterial cell characteristics, based on measuring how two sister cells become different from each other over time. Our measurements provide the inheritance dynamics of different cellular properties, and the ‘inertia’ of cells to maintain these properties along time. We find that inheritance dynamics are property specific and can exhibit long-term memory (~10 generations) that works to restrain variation among cells. Our results can reveal mechanisms of non-genetic inheritance in bacteria and help understand how cells control their properties and heterogeneity within isogenic cell populations. In the second study, we turn our attention to the specific question of cell size control in bacteria and focus on the role of the Min proteins dynamics in determining cell size. We demonstrate that the Min proteins, known to exhibit

pole-to-pole oscillation responsible for localizing the septal ring to mid-cell in *E. coli*, play a crucial role in setting the cell size. We show that manipulating the concentrations ratio of the Min proteins in the cell destabilizes their oscillation temporarily and leads to a delay in the formation of the division ring until the cell reaches a size that would stabilize the oscillation again. As a result, cells divide at a new stable size which is longer than observed in earlier cell-cycles with the preceding concentrations.

Table of contents

Preface.....	xiii
1.0 Introduction.....	1
2.0 Materials and methods	12
2.1 Fabrication of microfluidic devices.....	12
2.1.1 Mask preparation.....	13
2.1.2 Fabrication of the first layer for mother machine	16
2.1.3 Fabrication of the first layer for sisters machine	20
2.1.4 Second layer preparation for microfluidic devices	22
2.1.5 PDMS device preparation	24
2.2 Chemicals used.....	26
2.3 Bacterial strains and plasmids	27
2.4 Cell preparation for experiments	27
2.5 Image acquisition, and data analysis	28
3.0 Non genetic inheritance restraint of cell-to-cell variation.....	30
3.1 Limitations of the mother machine for measuring cell memory	31
3.2 Sisters machine: a new technique for measuring epigenetic cell memory	33
3.3 Results: Epigenetic inheritance of cell cycle time and cell size	42
3.4 Variance as a new parameter to estimate the nature of restraint on variability	46
3.5 Effect of antibiotics on sisters correlation	57
3.6 Conclusions	60
4.0 The contribution of Min proteins and their dynamics to cell size control.....	63

4.1 Materials and methods	67
4.1.1 Population level measurements of MinE/MinD effect on cell size	67
4.1.2 Single-cell experiments in mother machine	68
4.1.3 Real time RTPCR	69
4.1.4 Image acquisition and data analysis	71
4.1.5 Z ring intensity measurement	71
4.2 Overexpression of Min proteins and their effect on cell size	72
4.3 Single cell experiments	82
4.4 Conclusions	88
5.0 Discussions and conclusions	90
Appendix A Supplementary figures	95
Appendix B Supplementary methods	97
Appendix B.1 Preparation of electrocompetent cells for transformation	97
Appendix B.2 Plasmid extraction	98
Appendix B.3 Transformation of plasmids	98
Appendix C Source codes	100
Bibliography	109

List of tables

Table 1 Chemicals used during the experiments and their sources.	26
Table 2 Bacterial strains and plasmids used in this study.	27

List of figures

Figure 1 Cell size homeostasis models.....	7
Figure 2 Min protein oscillation dynamics.	10
Figure 3 Mask for the first layer of the microfluidic device designed in AutoCAD.....	13
Figure 4 Mask for the second layer of the microfluidic device designed in AutoCAD.	14
Figure 5 Complete mask for the preparation of microfluidic devices.	15
Figure 6 Hotplate, Reactive Ion etcher and Spincoater. Fabrication equipments located at NFCF at University of Pittsburgh. Pictures taken from NFCF webpage.....	16
Figure 7 Speed vs. thickness for various photoresists adapted from Rohm and Haas, 2006⁶⁰. The spinning speed required to achieve different thicknesses for the various photoresist materials. We use the S1805 photoresist.	17
Figure 8 Quntel Q4000 MA mask aligner located at NFCF at University of Pittsburgh. Picture taken from NFCF webpage.....	18
Figure 9 Photoresist interference curve adapted from Rohm and Haas, 2006⁶⁰. Energy dosage to cure photoresist layers of various thickness.	19
Figure 10 Surface Profilometer located at NFCF at University of Pittsburgh.	20
Figure 11 Nanoscribe Photonic Professional (GT).	22
Figure 12 Spin speed vs. layer thickness for SU8 photo resist. Picture adapted from Exposure (2000)⁶¹.	23
Figure 13 HMDS oven, MLA100 Direct Write Lithographer and Microscope.	24
Figure 14 PDMS device preparation.....	25
Figure 15 The ACFs of individual lineages measured in separate traps.	32

Figure 16 Microfluidic device to trap sister cells.	33
Figure 17 Example measurement of sister cells.	34
Figure 18 Individuality of cellular growth dynamics in different microenvironments in microfluidic device	36
Figure 19 The effect of the v-shaped channel on the distribution of the different cellular characteristics between SCs during division.	37
Figure 20 Distributions of different cell parameters.	39
Figure 21 Three types of pairs used for calculating PCF.....	41
Figure 22 PCF of cell cycle time measured in cell pairs as a function of number of generations.....	42
Figure 23 The PCF of cell cycle time (T) for SCs in different growth conditions.....	43
Figure 24 PCF of cell size measured in cell pairs as a function of number of generations. .	44
Figure 25 PCF values of cell size and cell cycle duration as a function of time for NCs with different starting size.	45
Figure 26 Cell-cycle time variance ($\sigma^2\delta T$) as a function of time.	48
Figure 27 Cell size variance ($\sigma^2\delta L_0$) as a function of time.	49
Figure 28 Exponential elongation rate difference ($\delta\alpha$) as a function of time.	50
Figure 29 Variance ($\sigma^2\delta\alpha$) as a function of the time.	51
Figure 30 Variance ($\sigma^2\delta\alpha$) as a function of the time.	52
Figure 31 Average growth rate difference between sister cells in first cell cycle.....	53
Figure 32 Variance of protein concentration.	55
Figure 33 Mean fluorescence variance ($\sigma^2\delta f$) as a function of time.....	56

Figure 34 Optical density(O.D.) of bacterial cultures as a function of time at different antibiotic concentrations.	58
Figure 35 PCF of cell cycle durations at different antibiotic concentrations.....	59
Figure 36 Added size as a function of Intial size.	64
Figure 37 Difference in added size of sister cells as a function of difference in their fractions.	64
Figure 38 Time averaged concentration of MinC in growing <i>E. coli</i> cells.....	66
Figure 39 Estimation FtsZ ring intensity in growing <i>E. coli</i> cell.....	71
Figure 40 The Min system oscillation.....	73
Figure 41 Average population size of cells overexpressing MinD.Average population size increases almost linearly with inducer concentration.	74
Figure 42 Average population size of cells overexpressing MinE. Average population size increases with inducer concentration before getting saturated to a fixed value.	75
Figure 43 Fluorescence image of cells over expressing MinD. Cells over expressing MinD at 0.2% arabinose show irregular attachment pattern.....	76
Figure 44 Mean fluorecence intensity of cells over expressing MinD. Similar to cell size, cells over expressing MinD show increase in mean fluorecence intensity with increase in inducer concentration.	77
Figure 45 Mean fluorecence intensity of cells over expressing MinE.....	78
Figure 46 Mean fluorecence intensity of MinE overexpressing cells during cell cycle.	79
Figure 47 Mean fluorecence intensity of MinE overexpressing cells as a function of size.	79
Figure 48 Ratio(R) of MinE to MinD in cells overexpressing MinE relative to the ratio (R ₀) in WT cells.	80

Figure 49 Average cell length as a function of ratio of Min proteins.....	81
Figure 50 Example trace of cell size during single cell experiment.....	83
Figure 51 Average cell size as a function of generations with overexpression of MinE.	84
Figure 52 Snapshot of a growth channel at different time points in an experiment.	85
Figure 53 FtsZ ring intensity during cell cycle.....	86
Figure 54 Stable Z ring timing traces as a function of generations after induction.	87
Figure 55 Average stable Z ring timing as a function of generations.....	88
Appendix Figure 1 Correlation in cell cycle times (T) for SCs at 32°C was verified by calculating slopes of best fits to the plots of normalized TimeA vs TimeB for the two cells.	95
Appendix Figure 2 Raw data of PCF of cellsize for SCs, NCs and RPs.	96

Preface

I am indebted to many people for their support and encouragement in the past 6 years during my doctoral research in Pittsburgh.

Firstly, I would like to express my sincere gratitude to my advisor, Dr. Hanna Salman, for his continuous support, invaluable advice and supervision towards my PhD dissertation. His persistent motivation, guidance and immense knowledge have encouraged me in all times of academic research and towards the successful completion of my PhD. Even during struggling instances in my PhD, Hanna was always very patient, positive and supportive, which has always inspired me to bring out the best in me. His optimistic attitude, enthusiasm and passion towards academic research influenced me to pursue postdoctoral research.

Apart from my advisor, I would also take this opportunity to thank my thesis committee members: Dr. Xiao-lun Wu, Dr. Vladimir Savinov, Dr. Robin Lee and Dr. David Pekker for their insightful comments and persistent encouragement on my graduate research.

I would like to acknowledge my colleague, Dr. Maryam Kohram, for all fruitful discussions and together we made significant advancements to the research in our lab. I would also like to thank Dr. Zhicheng Long, for mentoring me in the first year in learning the basics of the microfluidics and for building up the foundations for my future research.

I am thankful to the staff at Nanoscale Fabrication and Characterization Facility (NFCF) at University of Pittsburgh, mainly to Dr. Jun Chen, for their assistance in developing my microfluidic device.

My sincere gratitude also goes to Dr. Joanna Jammal, who helped me in the past few months in various experiments and for stimulating discussions. It would have been a valuable experience if I could spend some more time with her.

I gratefully acknowledge all contributions from our collaborator Dr. Naama Brenner, for putting her expertise and effort in broadening my understanding of my research and for offering critical comments which enhanced the quality of my work to new standards.

To my friends, Namitha, Meheli and Aditi, who always made sure of my well-being here and made my life in Pittsburgh memorable and fun, especially the weekend dinners, hangouts and karaoke sessions. I am also thankful to Abrajith, Raj and Sushma for all hangouts which resulted in deep discussions and debates regarding politics/history, which I always loved. I will definitely miss Sushma's delicious cooking. Lots of love to Nirali and Keshav, for all the little happiness and love you brought into my life, despite of being miles away.

Finally, I am forever indebted to my parents and my elder sister for believing in me and for being a constant support throughout my life. It wouldn't have been possible without them and the gratitude and love for them can't be just expressed in mere words. I dedicate this thesis to my late father who always inspired me to search for the truth.

1.0 Introduction

Dynamical processes in biology have been extensively studied by physicists as they play a pivotal role in shaping both physical and functional properties of the cells. These processes occur on a wide range of timescales that can be as short as milliseconds, such as in the case of firing action potentials in neurons^{1,2}, and as long as several generations, such as adaptive responses of cells to environmental changes through genetic mutations or epigenetic modifications³⁻⁵. Understanding how the dynamics of different processes contribute to the role they play in performing certain tasks in a quantitative manner is an essential first step that will help us move from a descriptive level to a more realistic account of biological processes. This will allow us to develop accurate mathematical models to describe living organisms that would allow prediction of outcomes. One of the earliest examples of success in this regard is the role of dynamic instability of microtubules assembly in morphogenesis, locomotion and cell division⁶⁻⁸. The erratic growth dynamics of microtubules has been shown to play a crucial role in separating copies of sister chromatids in opposite directions during cell division⁹. In this thesis, I investigate the dynamics of two such processes that occur at long and short timescales in the bacterium *E. coli* and quantify how they influence cell properties at different levels.

The first dynamical process I study is the epigenetic (non-genetic) inheritance and how it contributes to maintaining cellular properties over time. Epigenetics, refer to cellular processes and components, excluding the DNA, that influence the cell's properties and function. These include all the proteins, RNAs, and chemicals in the cell, as well as chemical and conformational modifications of the DNA, which bears the code for producing all proteins and RNA in the cell. Living cells maintain their phenotype, i.e., physical and functional properties, through a myriad of

complex interactions between all these components, which are passed on from one generation to the next. The transfer of cellular components between generations ensures that cells conserve their characteristics along time. Extensive research has been dedicated to understand how genetic information is inherited and decoded by cells to grow, develop and perform tasks¹⁰, which has allowed us to achieve important and fundamental understanding of genetic inheritance and evolutionary processes. On the other hand, the role of inheritance of non-genetic components in cell growth and function is much less understood despite increasing interest in recent decades. Nevertheless, the important role of epigenetics and their inheritance has been demonstrated in many studies. For example, Adam *et al.* showed that bacteria can evolve antibiotic resistance by epigenetically inheriting variant gene expression profiles, mediated by DNA methylation patterns or by chromatin modifications, for multiple generations¹¹. Another example comes from interspecies nuclear transfer experiments, where a nucleus from common carp was transferred into enucleated egg of a goldfish¹². The vertebral number of the resultant cloned fish were found to correspond to that of the egg donor goldfish rather than to that of nucleus donor carp. This demonstrates the importance of non-genetic material in determining the characteristics of cells and organisms (in this case). Several studies have shown that in bacteria, the transfer of genetic information through DNA is a very robust process, and any changes happening to it occur only on the scale of several 10s of generations through rare processes like genetic mutations or gene acquisition or loss¹³⁻¹⁵. However, the non-genetic components are subject to different levels of noise due to the stochastic nature of intracellular biochemical processes and of the distribution of resources during cell division¹⁶⁻¹⁸. For example, In a recent study it was shown that asymmetric partitioning of efflux pumps during cell division results in heterogeneity in antibiotic resistance in genetically identical bacterial cells¹⁹. Also, stochastic effects in gene expression have been shown

to produce huge cell-to-cell variation in an isogenic population^{20,21}. This randomness can play important roles in biological processes and lead to large variability in almost all measurable properties among individual cells in a very short period of time. In other words, cells that inherit similar characteristics can develop over time into different phenotypic states despite having identical DNA, experiencing homogeneous environmental conditions, and starting their life with the same initial conditions (same mother). This raises the question: how reliable and stable is the inheritance of non-genetic components? And over what timescale do cellular properties change due to stochasticity of biochemical processes and cell division? In Chapter 3, we obtain answers to these questions by quantitatively measuring the inheritance dynamics of cellular phenotypes along generations and determining their stability and persistence in the face of molecular noise and environmental fluctuations.

Non-genetic inheritance mechanisms and dynamics have been at the center of biological-physics research for decades. However, the lack of proper tools that would allow quantitative measurement of this dynamics has hindered its progress and prevented us from understanding the mechanism controlling it. Conventionally, researchers have used methods like agar pads or liquid culture to study cell growth^{22,23}. These methods can provide information about average population behavior but fail to capture subtle phenotypic differences between individual cells. Another limitation of these methods is that they cannot provide constant growth environment for an extended time. Since subtle changes in growth conditions can affect the non-genetic components on a very short time scale, it is very crucial to maintain a constant environment to extract the long-term memory effect associated with inheritance of non-genetic components in the cells. This necessity led to the invention of a new device known as the “mother machine” that utilizes microfluidic technology to trap and monitor growth dynamics of 100s of bacterial cells for an

extended period of time in constant environmental conditions^{24,25}. This device provides high throughput single cell data of various cellular properties such as cell size, protein content, and growth rate as a function of time in very long cellular lineages. These data have been used to gain insight into non-genetic inheritance and cellular memory and results obtained have consistently showed that non-genetic memory in bacteria is almost completely erased within two generations²⁵⁻²⁸. This consensus is based on calculation of average autocorrelation function (ACF) of different cellular properties. Nevertheless, such short memory fails to explain several phenomena including the long time a single cell requires to explore the entire range of variability covered by the population²⁵, or the long-term memory of antibiotic resistance that bacteria acquire epigenetically upon exposure to antibiotics¹¹. This we speculate is due to the fact that different cells in the microfluidic traps of the mother machine experience different environments at different times resulting from the dynamic interaction of the cells with their surroundings, which in turn creates diverse microniches in these traps. Each of these microniches exhibits distinct dynamics over time resulting from the individuality of the cell-environment interaction. Thus, averaging over many traps erases the dynamics of cellular memory. In order to understand how heterogeneity in physical and functional characteristics of cells proliferate within an isogenic population and how it is limited in part by the inheritance of non-genetic cellular components between consecutive generations, we need new methods that can separate cellular factors from the environmental ones.

To solve this problem, we have developed a new microfluidic device that enables us to simultaneously trap two cells immediately after they divide from a single mother and sustain them right next to each other for tens of generations, while removing their offspring from the trap²⁹. This allows us to compare the cellular properties of these two sister cells for several generations and estimate the time scale over which two identical cells become different from one another.

Since the sister cells have the same DNA and are also growing in the same environment, differences that we observe between them are non-genetic and not associated with variations in environmental conditions as both cells are maintained in the same environment throughout the experiment. I describe the design and fabrication process of the device in Chapter 2. The measurements done using this device provide the inheritance dynamics of different cellular properties, and the ‘inertia’ of cells to maintain these properties along time. Our results reveal several important features of cellular memory. The first is that different traits of the cell exhibit different memory patterns with distinct timescales. In addition, we find that some features exhibit complex dynamics and not a simple exponential decay of memory over time. These results indicate that cells exhibit different levels of restraints in controlling the divergence of their properties over time, which clearly refute the claim of the nonexistence of non-genetic memory in bacteria. These results can reveal mechanisms of non-genetic inheritance in bacteria and help understand how cells control their properties and heterogeneity within isogenic cell populations. I discuss this new method and results in detail in Chapter 3.

Bacteria have been able to survive for millions of years without getting extinct due to their remarkable capability of adapting to changing environmental conditions^{30,31}. There are predefined regulatory pathways to establish adaptive gene expression states that get activated when cells face familiar changes in their environments. However, cells often encounter novel stressful conditions that cannot be alleviated by these pre-defined pathways. In this situation, individual genes achieve new gene expression levels through a stochastic search for improved fitness^{32,33}. To test the extent of non-genetic inheritance influence over cellular properties in the presence of novel stressful situations, we subject bacterial sister cells to various degrees of environmental stress and examine

the dynamics of their phenotypic correlations over time. This is discussed in detail as well in Chapter 3.

The dynamical process of inheritance of non-genetic components influences cell properties over a timescale of multiple generations. On the other hand, there are many cellular processes happening on shorter timescales that play an important role in determining cellular properties in each generation. In chapter 4, I turn my attention to a process happening at a such short timescale and focus on the specific question of cell division and size control in bacteria. Thus, the second dynamical process I investigate is the oscillation of the Min-system proteins, which act to position the septal ring responsible for dividing a bacterial cell into two daughter cells. This oscillation is an essential process, without which cells cannot divide and thus will eventually die. It is also fundamental in maintaining cell size stable and prevent size divergence over time.

Microorganisms like bacteria exist in diverse shapes and sizes. Despite this great variety observed between different species of bacteria, size and shape are uniformly maintained within each species. This implies that there is a significant value in maintaining the specific shape and size, which is best suited for a given environment and therefore, cells must have in place mechanisms to set this size. The bacterium *E. coli* has a relatively simple cell cycle during which it duplicates its DNA and accumulates cell mass approximately exponentially. At the end of each cell cycle, it divides into two equal-size daughter cells. This process of cell growth and division is subjected to different levels of noise that can lead to deviation from the stable size suited for a given condition. This suggests that these cells must have mechanisms to correct the aberration in the size introduced due to stochasticity of the involved processes. How cell size homeostasis is achieved is an important question and several models have been proposed to explain this apparent simple cell cycle and size dynamics. The most popular among these models are “timer”, “sizer”

and “adder” models. The timer model proposes that cells grow for a fixed time in each cell cycle irrespective of their birth size. This fixed time model cannot provide size homeostasis as the cells born smaller or larger than the desired size can never reach the stable size. The sizer model, on the other hand, proposes that cells aim to reach a specific size in each generation before they divide into daughter cells³⁴. This suggests that the correction to the size aberration happens in just one generation. A more recent model popularly known as the “adder model” proposes that cells, irrespective of their initial size, add a fixed amount of cell volume in each cell cycle to achieve size homeostasis^{26,27,35}. This implies that the cells born smaller or larger than the desired size will exponentially converge to the steady state size. Figure 1 summarizes the three most popular size homeostasis models.

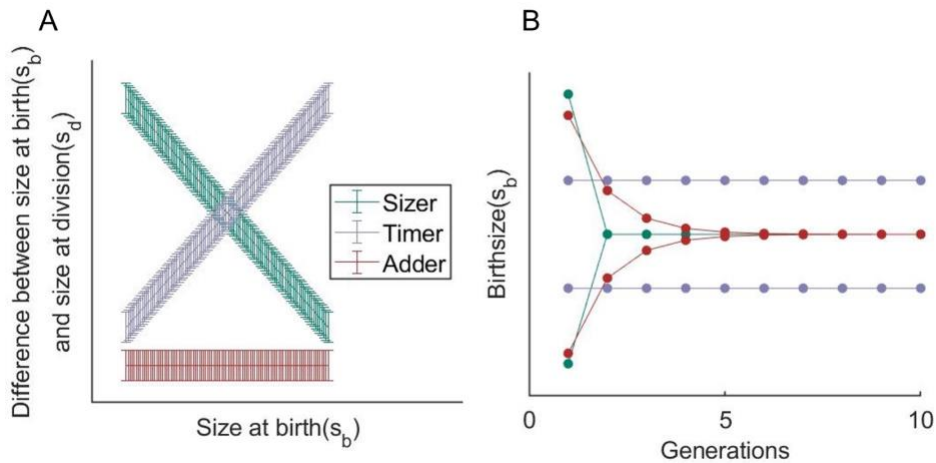


Figure 1 Cell size homeostasis models. (A) Size added during cell cycle as a function of birth size. According to sizer model, cells divide after reaching a fixed size in each cell cycle, thus volume added by cells in each cycle is inversely proportional to their birthsize. Hence it shows a slope of -1. Assuming exponential growth of the cells, timer model proposes that cells grow for a fixed time in each cell cycle, hence it gives a slope of +1. Adder model proposes constant size addition in each cell cycle and gives slope of 0. (B) Convergence of cell size to the target size in subsequent generations according to the three models. Figure adapted from Facchetti et. Al, 2017³⁴.

While some of the correlations predicted by these phenomenological models, can indeed be found in the size dynamics measurements at the average population level, they do not reflect the mechanism of cell division and size homeostasis at the single-cell level. Even after extensive research, the exact mechanism of size control is still unknown and no model has been successful in capturing the complex features of the bacterial growth and division comprehensively. Recently, a mechanism has been proposed in support of the adder model. According to this mechanism, size homeostasis can be exclusively driven by balanced biosynthesis and accumulation of division proteins to a fixed number to facilitate cell division³⁶. This simple mechanism explains adder behavior well but requires a stringent control on biosynthesis and cells to count a fixed number of molecules in each generation rather than their concentration. The buildup of division protein to a threshold to trigger division has been suggested by previous studies³⁷ as well but it cannot serve as the sole driving force for cell size homeostasis. For example, in Chapter 4 I show that at the single cell level when we compare the size added by two daughter cells during the first generation after cell division, the smaller daughter tends to add more volume than its bigger sister. If division is controlled by the buildup of the division protein alone, then both cells should add the same amount of volume irrespective of their relative initial sizes. To address the question of size homeostasis and advance our understanding of the underlying control mechanism(s), I study the process of cell division at the molecular level and examine the dynamical processes that play an important role in determining cell size.

To determine their size, cells must have mechanisms that control the frequency of cell division and the position at which they divide to produce the “right” size daughter cells. In 1974, Teather *et al.* observed the division pattern of cells and suggested that there must be a substance that triggers cell division at a given site³⁷. In early 90s, Bi *et al.*³⁸ suggested that this molecule

controlling the division frequency is the FtsZ protein, a tubulin homologue, and later using immunoelectron microscopy confirmed that in each cell cycle a division site is generated at the mid-cell plane where FtsZ forms a ring-like structure with other divisome proteins³⁹⁻⁴¹. Later, Tetart & Bouche showed that a reduction in FtsZ amount in cells results in a delay in cell division and produces a culture with larger cell size at steady state⁴². These studies confirmed that FtsZ plays an essential role in controlling the frequency of cell division in *E. coli*. The selection of division site and localization of FtsZ in *E. coli* is regulated by a complex dynamics of the MinCDE system through a negative regulatory mechanism⁴³⁻⁴⁶. The MinCDE system inhibits assembly of FtsZ ring near the polar regions through a self-organized gradient of MinC, the FtsZ inhibitor. The concentration of MinC remains high at the polar regions and minimal at the middle of the cell allowing FtsZ to bind only near the midplane. This concentration gradient is generated by complex dynamics of the MinCDE system. MinD-ATP binds to the cell membrane near one of the polar regions and recruits MinC at that site. MinE removes MinCD complex through hydrolysis of MinD-ATP. Unbound MinD-ADP converts back to MinD-ATP and goes to the other polar region and bind again to the cell membrane. This results in pole-to-pole oscillations of these proteins. Figure 2 summarizes the complete MinCDE system dynamics. It has been shown that these oscillations have a typical wavelength that depends on the relative concentrations of these proteins, reaction rates and cell geometry⁴⁷⁻⁵¹.

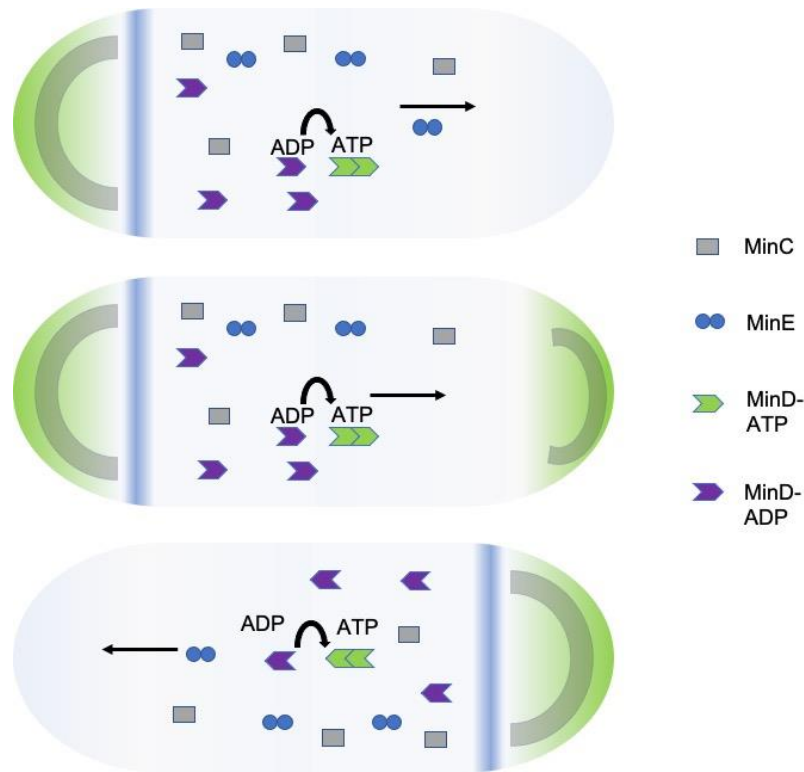


Figure 2 Min protein oscillation dynamics. MinD-ATP binds to the cell membrane near the polar region and recruits MinC. MinC being the inhibitor of FtsZ, prevents the binding of FtsZ in that region. Another protein, MinE chases MinCD complex and dissociates it from the membrane by converting MinD-ATP to MinD-ADP. Free MinD-ADP converts back to MinD-ATP and bind to the other polar region and recruits MinC. This results in pole to pole oscillations of MinCDE system that helps in correct placement of division septum in growing *E. coli* cells. Figure adapted from Lutkenhaus J., 2007⁴⁶.

In Chapter 4, I propose that the optimum cell size for division changes with the change in frequency of oscillations of Min proteins determined by their relative concentrations. The combination of cell length and oscillation frequency determine the shallowness of MinC gradient at the division site and affects the timing of the FtsZ ring formation. I give experimental evidence to support the proposed mechanism by changing the relative concentrations of the Min proteins,

which in turn affects the timing of the FtsZ ring formation and consequently the bacterial cell size at division. I detail my experimental methods and results further in Chapter 4.

2.0 Materials and methods

In this chapter, we present the design and fabrication of microfluidic devices used in this study. We also explain the experimental methods and list the sources of the materials in terms of chemicals, plasmids and bacterial strains used in this study.

2.1 Fabrication of microfluidic devices

Standard experimental methods like agar pads and batch cultures are excellent tools for population level studies but do not tell us much about the dynamics at the single cell level. As a result, the important information about the phenotypic differences among individual cells is often lost. In order to understand how the population behavior emerges from the behavior of single cells, it is essential to quantify phenotypic differences among cells and study growth dynamics at the single-cell level for extended periods of time. Therefore, there is a need for new and advanced methods to address these questions. Recent advantages in technology have enabled researchers to overcome these barriers and obtain long-term single cell data by developing excellent microfluidic devices. These devices are micro-scale machines that have highly parallel system of micron-size channels that allow successful trapping and tracking of thousands of individual cells at the same time. These devices also allow for real time change and control of the experimental conditions. Due to their high throughput and faster output time compared to conventional methods, these devices have been very successful in several different areas like point of care diagnostics⁵², single cell analysis⁵³, chemical analysis⁵⁴ and sequencing⁵⁵.

To prepare these microfluidic devices, first the desired pattern of the micro-channels is fabricated on a substrate using photolithography. Then, the elastomers like polydimethylsiloxane (PDMS) are used to create the prototypes of the devices used in the experiments. PDMS is a preferred choice for making these devices because it is inexpensive, non-toxic and easy to mold. It is transparent, bio-compatible and permeable to gases which makes it ideal for experiments involving long-term microscopy with living cells^{56,57}.

In this study we have designed two microfluidic devices namely “Mother machine” and “Sisters machine” to perform bacterial growth analysis at single cell level. The design and fabrication process of these microfluidic devices is detailed in the following sections.

2.1.1 Mask preparation

Masks for the microfluidic devices used in this study were designed using AutoCAD software (Autodesk) and then printed and purchased from Photo Sciences, Inc. (Torrance CA).

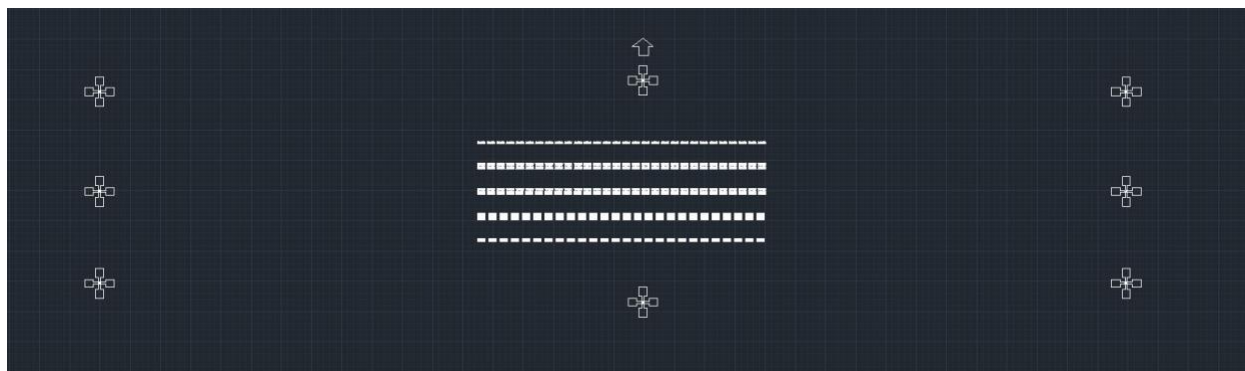


Figure 3 Mask for the first layer of the microfluidic device designed in AutoCAD. The first layer consists of arrays of growth channels designed to trap 100s of bacterial cells at the same time. Each row in the image contains 200 channels (1 μm width \times 30 μm length). The distance between neighboring channels is 4 μm .

These microfluidic devices have microchannels of different heights and widths that allow us to trap bacterial cells for extended period of time and feed liquid medium to maintain constant growth conditions. To create different heights channels within the same device, the fabrication is carried out in two steps. The growth channels, which are $1\ \mu\text{m}$ high \times $1\ \mu\text{m}$ wide and used to trap the bacterial cells, are fabricated first (Figure 3). This is followed by fabrication of the second layer of the larger channels, which are $30\ \mu\text{m}$ high \times $30\ \mu\text{m}$ wide and used to pump in fresh medium to feed the trapped bacteria (Figure 4).

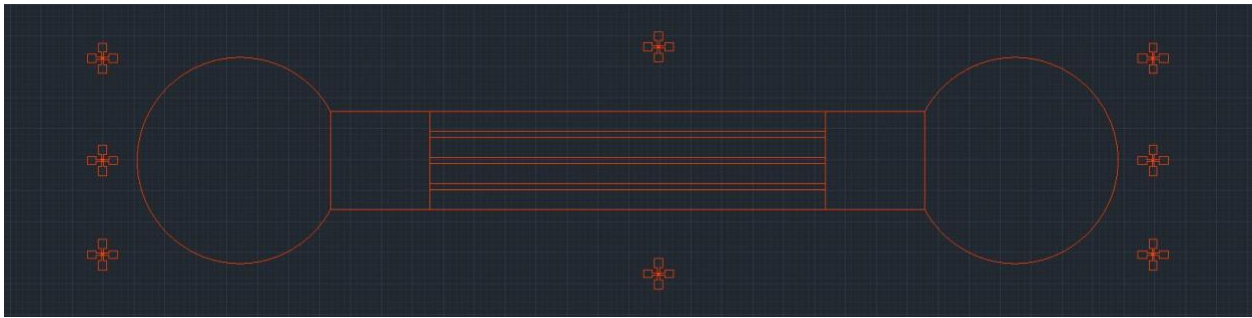


Figure 4 Mask for the second layer of the microfluidic device designed in AutoCAD. The second layer consists of $30\ \mu\text{m}$ high \times $30\ \mu\text{m}$ wide big channels to supply fresh medium to the trapped cells and wash excess cells coming out of the narrow channels.

Two different photolithography techniques were used to fabricate the two layers of the devices used in this study. Standard photolithography^{58,59} was used to create the first layer containing the growth channels of the “Mother machine” (Figure 5) (see section 2.1.2 for details), while 3D printing was used to fabricate the first layer of the “Sisters machine” (see section 2.1.3 for details). The second layer for both devices was fabricated using standard photolithography

techniques (Section 2.1.4). All the steps of the fabrication were carried out in the clean room at the Nanoscale Fabrication and Characterization Facility (NFCF) of the University of Pittsburgh.

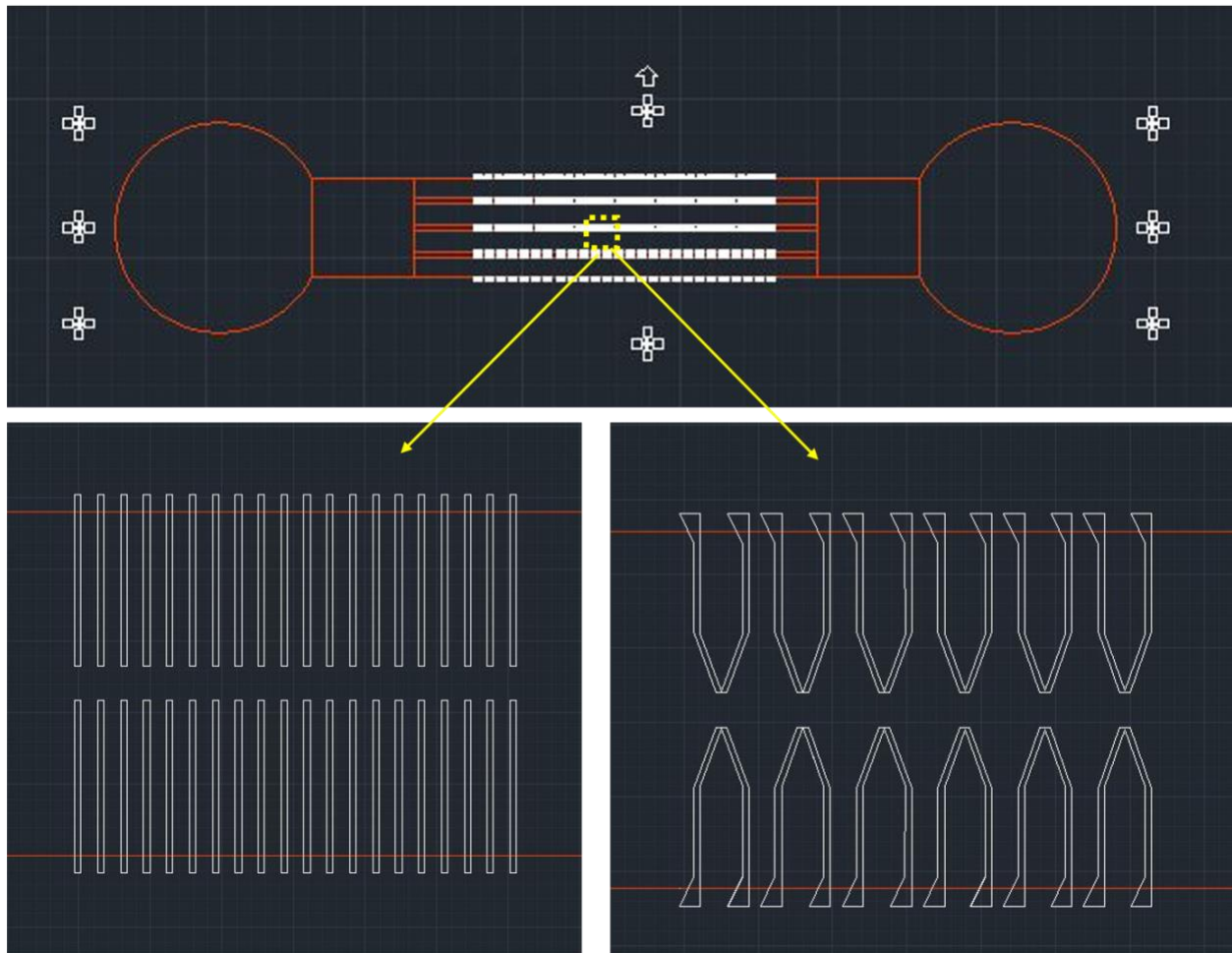


Figure 5 Complete mask for the preparation of microfluidic devices. Top panel shows masks for both the layers overlapping on top of each other. Bottom left shows closeup of growth channels of mother machine. Bottom right shows growth channels of sisters machine. Growth channels of the sisters machine are open at one end like mother machine but joined together in a V-shape at the other end to facilitate trapping of the sister pairs.

2.1.2 Fabrication of the first layer for mother machine

The first layer of mother machine consists of $30\ \mu\text{m}$ long and $1\ \mu\text{m}$ wide straight channels to trap the bacterial cells (Figure 5). The height of these traps is also kept at $1\ \mu\text{m}$ to restrict the free movement of the cells once they get inside the traps. This allows us to trap bacterial cells for extended periods of time and measure their growth dynamics.

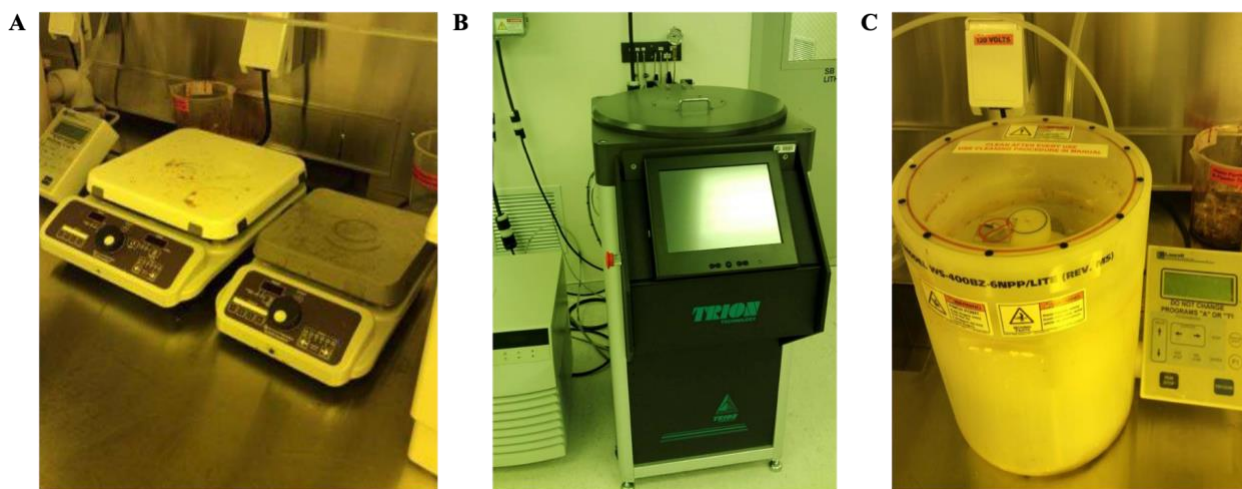


Figure 6 Hotplate, Reactive Ion etcher and Spincoater. Fabrication equipments located at NCF at University of Pittsburgh. Pictures taken from NCF webpage.

To fabricate this layer, a 3-inch circular silicon wafer was baked at $200\ ^\circ\text{C}$ for 5 mins by placing it on a hot plate (Barnstead Super-Nuova) (Figure 6A). Next, the wafer was cleaned with oxygen (O_2) plasma for 5 minutes using a Reactive ion etcher (Trion Phantom III LT RIE) (Figure 6B). The wafer was then spin-coated with a very thin ($\sim 1\text{-}2\ \mu\text{m}$) layer of S1805 optical photoresist using a spin coater (Laurell WS-400B) (Figure 6C) at 2000 rpm for 50 seconds (Figure 7).

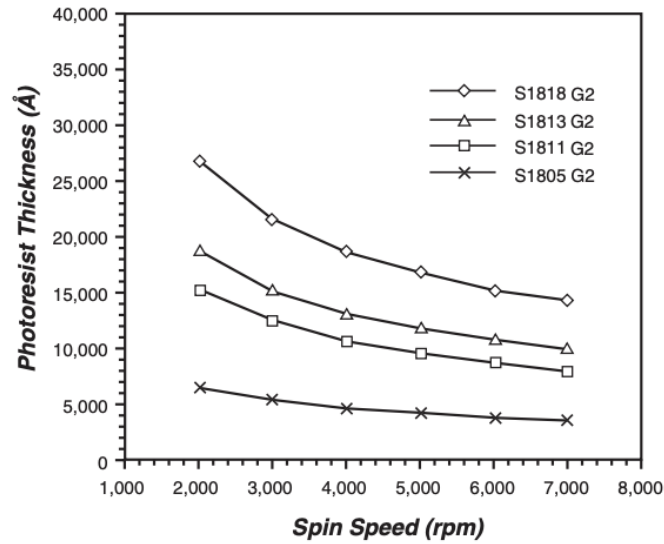


Figure 7 Speed vs. thickness for various photoresists adapted from Rohm and Haas, 2006⁶⁰. The spinning speed required to achieve different thicknesses for the various photoresist materials. We use the S1805 photoresist.

Following the coating step, the wafer was soft baked at 110°C by placing it on a hotplate for 1 minute. Next, the wafer with the photoresist coat was placed on the Quintel Q4000 MA mask aligner (Figure 8) and aligned using the alignment marks. The mask aligner was set to vacuum contact mode with a wavelength of 365 nm and the wafer was exposed to an energy dose of 100 mJ/cm² for 20s as calculated from Figure 9. After the exposure, the wafer was baked again at 115°C for 1 minute by placing it on a hotplate.



Figure 8 Quntel Q4000 MA mask aligner located at NFCF at University of Pittsburgh. Picture taken from NFCF webpage.

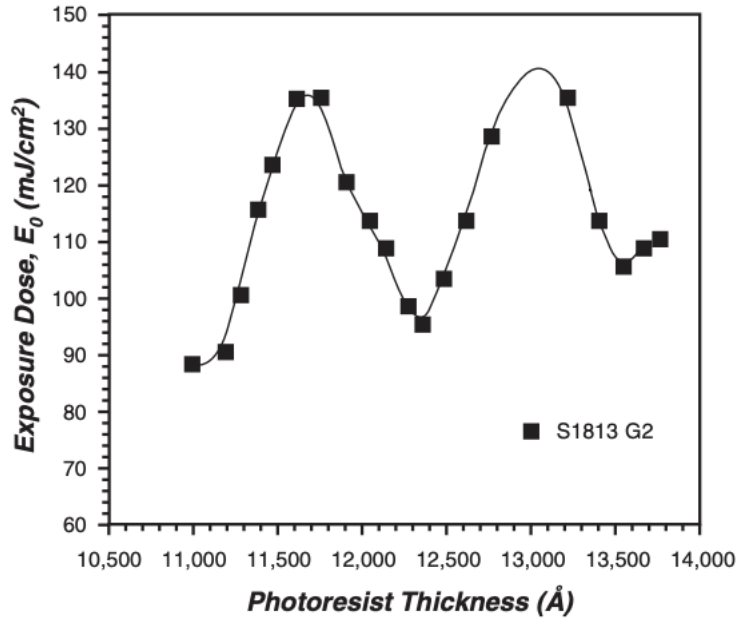


Figure 9 Photoresist interference curve adapted from Rohm and Haas, 2006⁶⁰. Energy dosage to cure photoresist layers of various thickness.

To wash the photoresist and develop the first layer mold, the substrate was washed with 351 developer (15% conc. in H₂O) for 30s. To create the permanent pattern, the wafer was etched using Reactive Ion Etcher (Trion Phantom III LT RIE) (Figure 6B) with the following recipe: $SF_6 = 25$, $O_2 = 4$, $CHF_3 = 10$, for 100 seconds. Following the etching process, the height of the channels was measured using surface profiler (KLA-Tencor AlfaStep IQ Surface Profilometer) (Figure 10). The etching process was repeated until the desired height of the channels was obtained. Next, the wafer was cleaned with Piranha solution (3 H₂SO₄ : 1H₂O₂) for 10 mins to get rid of any excess photoresist. Following the piranha etch, the substrate was washed with water to remove any residue of the Piranha solution.

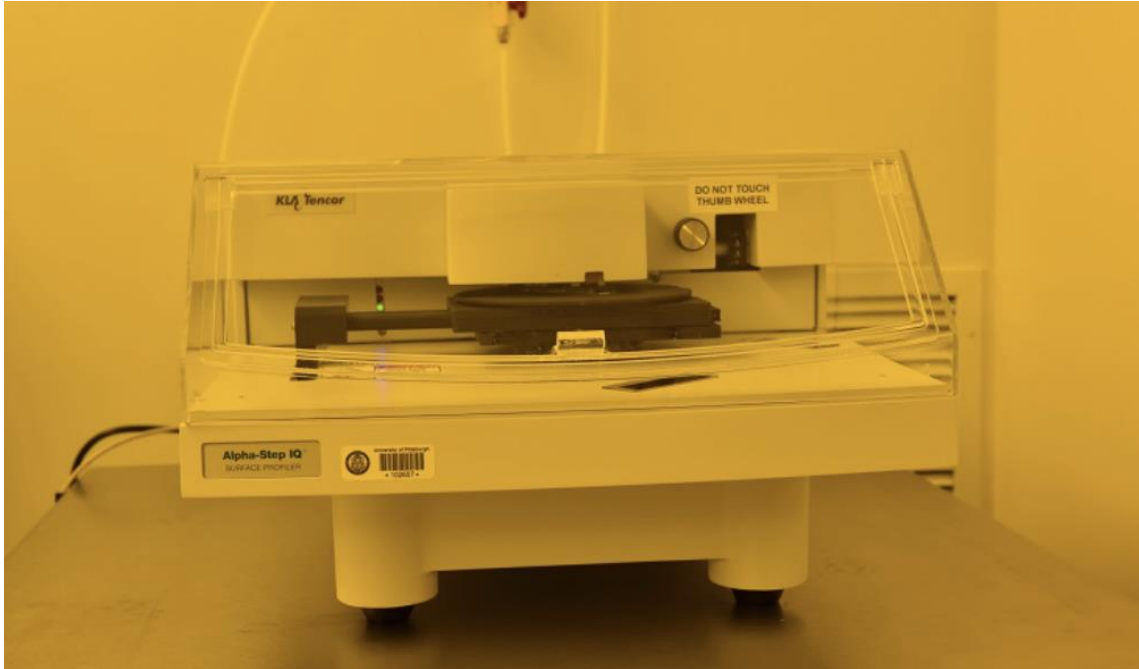


Figure 10 Surface Profilometer located at NCFE at University of Pittsburgh. Picture taken from NCFE webpage.

2.1.3 Fabrication of the first layer for sisters machine

The first layer of the "sisters machine" consists of 30 μm long and 1 μm wide trapping channels similar to the mother machine (Figure 5). However, in this new device, every two neighboring trapping channels are joined via a v-shaped connection of the same width. The tip of the v-shaped connection is made 0.5 μm narrower than the rest of the channel to reduce the likelihood of cells passing from one side to the other. The height of these channels was also kept at 1 μm similar to the mother machine. Since the first layer of the sisters machine has some features with dimensions less than 1 μm , we used 3D printing on a silicon substrate to achieve the required high accuracy in channel widths and heights. First, a 1 mm x 1 mm silicon substrate was cleaned with acetone and Isopropyl alcohol (IPA) in an ultrasonic sonicator (Branson) for 5 mins each to

get rid of any dirt on the surface. Next, it was cleaned with oxygen plasma in Reactive ion etcher (Trion Phantom III LT RIE) for 5 min to make sure the surface is clean of any kind of impurity before using it for 3D printing. The substrate was then immersed in surfpass 3000 in a 50 ml beaker. After 5 min it was taken out and blow-dried using high pressure N₂ gun. This step was done to achieve better bonding with the photoresist material used in the 3D printing step. A small drop (0.5ml) of IP-dip resist was put at the center of the substrate, which was then loaded onto the 3D printer stage using a substrate holder. The printing process was executed using Nanoscribe Photonic Professional (GT) (Figure 11) operating on 63x objective lens to achieve better feature resolution. Upon completion of the printing process, the substrate was unmounted and dipped in SU8 developer to remove excess IP-dip resist. After 8 mins it was taken out and dipped in IPA for 2 mins to remove excess SU8 developer. Following this step, the substrate was left to air dry for 5-7 mins. At this point, the substrate was ready with the growth channels molded onto it. It was left for a day to allow the bonding to stabilize before proceeding to following steps.

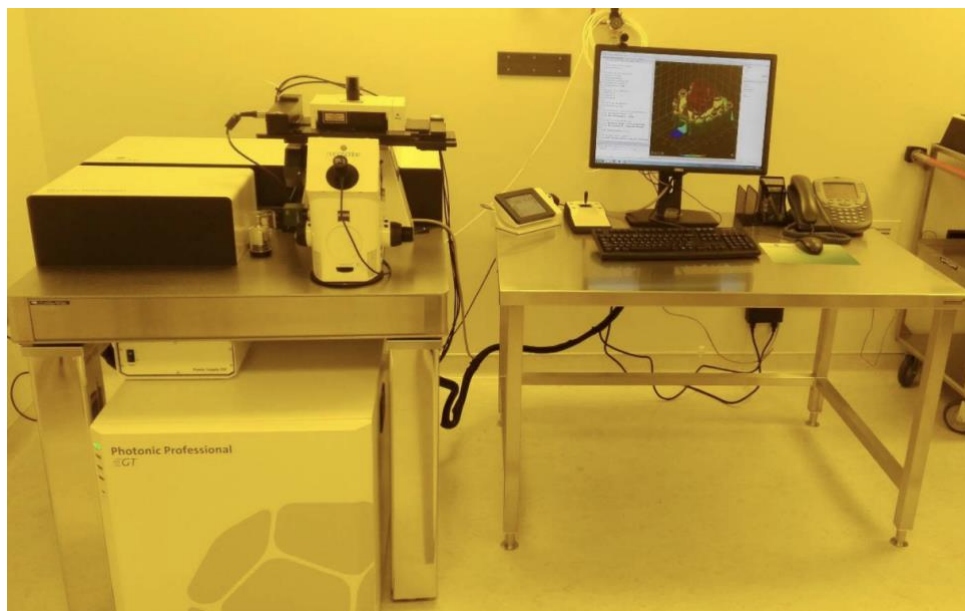


Figure 11 Nanoscribe Photonic Professional (GT). 3D printer located at NCF at University of Pittsburgh. Picture taken from NCF webpage.

2.1.4 Second layer preparation for microfluidic devices

The second layer of both microfluidic devices is identical. It consists of several 1mm long \times 30 μm high \times 30 μm wide main flow channels, used to supply nutrients to the trapped bacteria and wash out the excess cells (Figure 4). It was fabricated using the standard photolithography process. The sister machine substrate containing the 3D printed growth channels or the mother machine substrate, with the etched growth channels, were first coated with a thin layer of HMDS using HMDS oven (YES 3TA HMDS Vapor Prime Oven) (Figure 13A). Next, each of the substrates was spin-coated with SU8 2015 photoresist using the spin coater for 10 seconds at 500 rpm followed by 60 seconds at 1500 rpm to achieve a 30 μm thick layer (Figure 12).

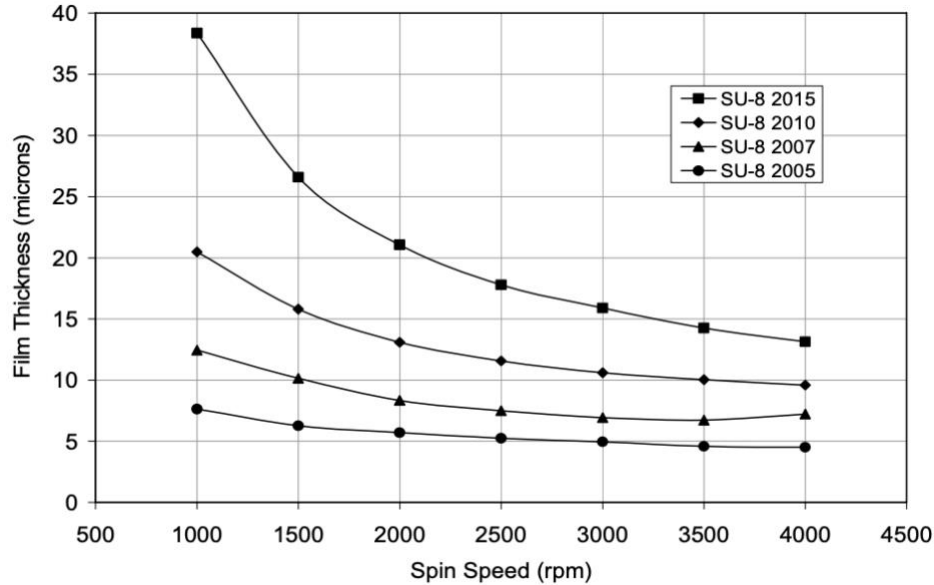


Figure 12 Spin speed vs. layer thickness for SU8 photo resist. Picture adapted from Exposure (2000)⁶¹.

The coated substrate was then baked at 65°C for 5 minutes, followed by 50 minutes at 95°C using a hotplate. This was followed by exposing the substrate to a LED light (390 nm – 10000 mW) using MLA100 Direct Write Lithographer (Heidelberg Instruments) (Figure 13B). After the exposure, the substrate was baked at 65°C for 3 minutes, and then at 95°C for 15 minutes on a hot plate. To wash the excess photoresist and reveal the features of the second layer, the substrate was developed in SU8 developer for 1:45 minutes. The substrate was then examined under the Zeiss Axio Imager Motorized Optical microscope (Zeiss) (Figure 13C) for proper development of the features and developed again for a few more seconds if needed. Finally, the resulting mold with all the features was hard baked at 200°C for 20 minutes using a hot plate.

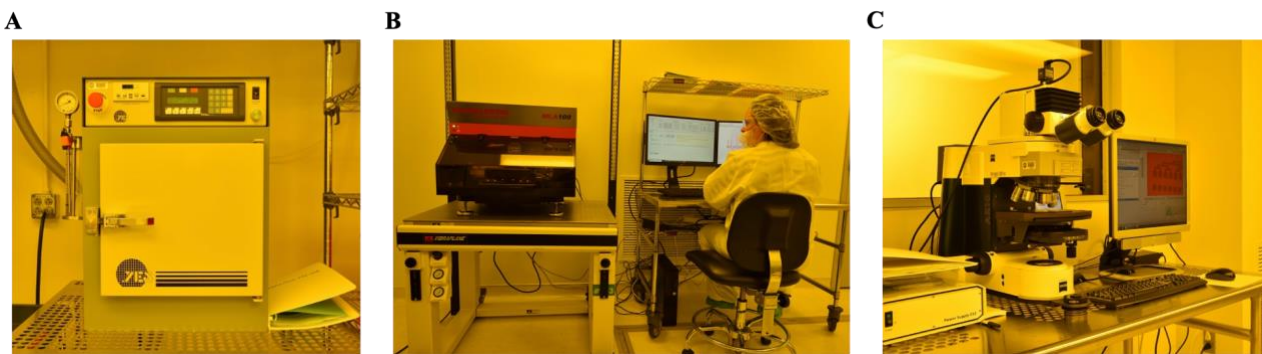


Figure 13 HMDS oven, MLA100 Direct Write Lithographer and Microscope. Located at NFCF at the University of Pittsburgh. Pictures taken from NFCF webpage.

Following the hard bake step, the master mold was silanized by placing it with a small amount (~1 ml) of trichlorosilane 99% (Gelest Inc., USA) in a vacuum chamber for 30 mins. Silanization creates a monolayer of silane over the substrate and makes sure that the PDMS does not stick to the wafer and can be easily peeled off without damaging the mold features.

2.1.5 PDMS device preparation

PDMS (Polydimethylsiloxane) was prepared by mixing silicon elastomer base and curing agent (Dow Corning, Sylgard 184 Silicone Elastomer) in 9:1 ratio (w/w) respectively. The mixture was stirred vigorously for 5-7 min to ensure even mixing. PDMS mixture was then poured over the silanized master mold placed in a 100 mm diameter Petri dish with its base covered with Aluminum foil. The Petri dish was then moved into a vacuum chamber for 35-45 min to degas the PMDS mixture and remove air bubbles introduced during the mixing process. The Master mold with the PDMS was then incubated in an oven at 65°C for 8–10 hr to solidify. Next, the PDMS was peeled off and cut in a rectangular shape suitable to be fixed on top of a glass cover slip

(24×60mm, 0.16 to 0.19 mm thick). Two small pieces of PDMS were also cut and tiny holes were punctured in them to insert the inlet and outlet tubes. To bind the PDMS with glass coverslip/PDMS, glass coverslip and PDMS were placed in a Plasma cleaner PDC-32G (Harric Plasma) for 2 mins and then the exposed surfaces were placed in contact to allow the PDMS to bind with the glass/PDMS (Figure 14). The bound device was then incubated at 70°C on a hot plate for 1 hr to strengthen the bonds.

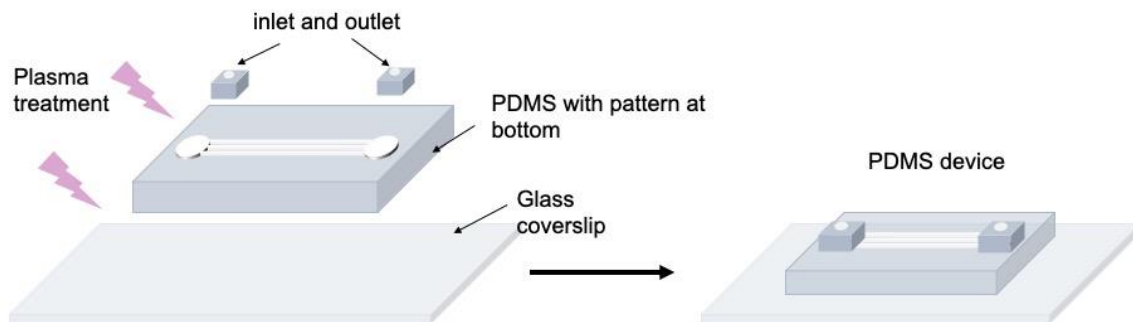


Figure 14 PDMS device preparation. Cut PDMS parts and glass cover slip are treated with oxygen plasma and then attached together to form working PDMS device.

2.2 Chemicals used

Table 1 Chemicals used during the experiments and their sources.

Chemical	Source	Chemical	Source
Ampicillin	Sigma-Aldrich Co.	Luria Broth (LB)	Sigma-Aldrich Co.
Arabinose	Sigma-Aldrich Co.	M9 salts	MP Biomedical, LLC.
Bacto agar	Becton Dickinson	MgSO ₄	Sigma-Aldrich Co.
CaCl ₂	Sigma-Aldrich Co.	Monobasic K ₂ HPO ₄	EMD Chemicals
Casamino acids	MP Biomedical, LLC.	NaCl	Fisher Scientific
Chloramphenicol	Sigma-Aldrich Co.	PDMS	Dow Corning
Glucose	MP Biomedical, LLC.	Tris	BIO-RAD
Glycerol	EMD Chemicals	Ultrapure Agarose	Invitrogen

2.3 Bacterial strains and plasmids

Table 2 Bacterial strains and plasmids used in this study.

Strain/Plasmid	Description	Resistance/Induction	Source
pZA3R-GFP	Green fluorescent protein expressed from λ Pr promoter	Chloramphenicol	Salman
pZA32wt-GFP	Green fluorescent protein expressed from LacO promoter	Chloramphenicol	Salman
pZA3R-mcherry	Red fluorescent protein expressed from λ Pr promoter	Chloramphenicol	Salman
mEos-minE/ minD	a photoactivatable green to red fluorescent protein fused with MinE/MinD	Ampicillin/arabinose	Huang
MG1655	Wild type <i>E. coli</i> strain		Salman
MG1655, ftsZ::ftsZ-mVenus	Strain with mVenus fused in an internal site of FtsZ gene.	Kanamycin	Huang

2.4 Cell preparation for experiments

The cultures for all the experiments performed in this study were initiated from glycerol stock stored at -80°C and grown overnight at 30°C, in either LB or M9CL medium depending on the intended experimental conditions. The following day, the cells were diluted in the same medium and regrown to early exponential phase, Optical Density at 600 nm (OD_{600nm}) between

0.1 and 0.2. When the cells reached the desired OD_{600nm} , they were concentrated into fresh testing medium to an $OD_{600nm} \sim 0.3$. The microfluidic device was washed with 20mg/ml Bovine Serum Albumin (BSA) in water for 15 mins, and then with fresh medium for 10 mins. The concentrated cells were then loaded into the microfluidic device. Once enough cells were trapped in the channels, fresh testing medium was pumped through the wide channels of the device to supply the trapped cells with nutrients and wash out extra cells that are pushed out of the channels. The cells were allowed to grow in this device for several days, while maintaining constant temperature, using a microscope top incubator (Okolab, H201-1-T-UNIT-BL), and a continuous flow of fresh medium to feed trapped cells. The wild type MG1655 *E. coli* bacteria were used in all experiments described. Soluble protein content was measured through the fluorescence intensity of fluorescent proteins (FP) inserted into the bacteria on the medium copy number plasmid pZA⁶². The expression of FP was controlled by one of two different promoters. The Lac Operon (LacO) promoter was used to measure the expression level of a metabolically relevant protein, while the viral λ –phage Pr promoter was used to measure the expression level of a constitutive metabolically irrelevant protein. Two testing media were used in our experiments. M9 minimal medium supplemented with 1g/l casamino acids and 4g/l lactose (M9CL) was used for measuring the expression level from the LacO Promoter, and LB medium was used for all other experiments.

2.5 Image acquisition, and data analysis

Images of the bacterial cells growing in the channels were acquired, unless stated otherwise, every 3 minutes (in LB medium) or 7 minutes (in M9CL medium) in DIC and fluorescence modes using a Nikon eclipse Ti2 microscope with a 100x objective. The size and

protein content of the cells were measured from these images using the image analysis software Oufiti⁶³. The data were then used to generate lineage traces and for further analysis as detailed in Chapter 3.0 and Chapter 4.0. Single-cell measurements were analyzed using MATLAB. Sample autocorrelation functions, Pearson correlation coefficients, sample distributions and curve fitting were all calculated by their implementations in MATLAB toolboxes.

3.0 Non genetic inheritance restraint of cell-to-cell variation

One of the main challenges in biological physics today is to quantitatively predict the change over time in cells' physical and functional characteristics, such as cell size, growth rate, cell-cycle time, and gene expression. All cellular characteristics are determined at all times by the interaction of genetic and non-genetic factors. While genetic information passed from generation to the next is the main scheme, by which cells conserve their characteristics, non-genetic cellular components, such as all proteins, RNA and other chemicals, are also transferred between consecutive generations and thus influence the state of the cell's characteristics (or its phenotype) in future generations^{64,65}. The mechanism of genetic information transfer between generations, as well as how this information is expressed, are mostly understood⁶⁶⁻⁶⁸. This information can be altered by rare occurring processes such as mutations, lateral gene transfer, or gene loss^{69,70}. Therefore, changes resulting from genetic alterations emerge over very long timescales (several 10s of generations). On the other hand, inheritance of non-genetic cellular components, which are subject to a considerable level of fluctuations, can influence cellular characteristics at shorter timescales⁷¹⁻⁷⁴.

Here we focus on understanding how robust cellular characteristics are to intrinsic sources (stochastic gene expression and division noise) and extrinsic sources (environmental fluctuations) of variation, and how cells that emerge from a single mother develop distinct features and over what time scale. While our understanding of variation sources has increased significantly over the past two decades^{17,75,76}, progress in understanding non-genetic inheritance and its contribution to restraining the proliferation of heterogeneity has been extremely limited. Extensive studies have been dedicated to revealing the different non-genetic mechanisms that influence specific cellular

processes and how they are inherited over time⁷⁷⁻⁸¹. However, the cell's phenotype is determined by the integration of multiple processes. Thus, to predict the inheritance dynamics of a cellular phenotype, we need to measure the inheritance dynamics directly rather than characterizing the effect of individual inheritance mechanisms separately. Progress in this research has been drastically hindered by the limited experimental techniques that can provide reliable quantitative measurements. Here we have developed such a method that can allow us to measure the inheritance dynamics of the cellular phenotype directly and we utilize mathematical methods to estimate the time scales of the inheritance dynamics.

3.1 Limitations of the mother machine for measuring cell memory

The recent development of the microfluidic device named “mother machine”^{24,82}, has provided valuable data of growth and division, as well as protein expression dynamics. These data have been used to gain insight into non-genetic inheritance and cellular memory. The results obtained have consistently showed that non-genetic memory in bacteria is almost completely erased within two generations^{24,25,83}. This has been also the conclusion of theoretical calculations of cell size autocorrelation^{25,28}; which are based on the adder model for size homeostasis^{26,27,35}. The consensus of previous experimental studies is founded on the calculation of the autocorrelation function (ACF) for the different measurable cellular properties, such as cell size, growth rate, cell cycle time, and protein content. It is important to note that in calculating the ACF, measurements of cells from different traps of the mother machine are averaged together. However, small variation in the traps sizes can manifest during the fabrication process, which can lead to distinct environments in different traps⁸⁴. In addition, cells might experience slightly different

environments at different times resulting from thermal fluctuations and their dynamic interaction with their surroundings, i.e., environmental fluctuations can influence the cell's growth and division dynamics, which in turn can change the cell's micro-environment through consumption of nutrients and/or secretion of other chemicals. As a result of the individuality of the cell-environment interaction, different micro-niches can be created in different traps (as we demonstrate later), which give rise to diverse patterns of growth and division dynamics and therefore distinct ACFs (Figure 15)^{25,83,84}. Averaging over many traps, with such various ACFs, will thus erase the dynamics of cellular memory.

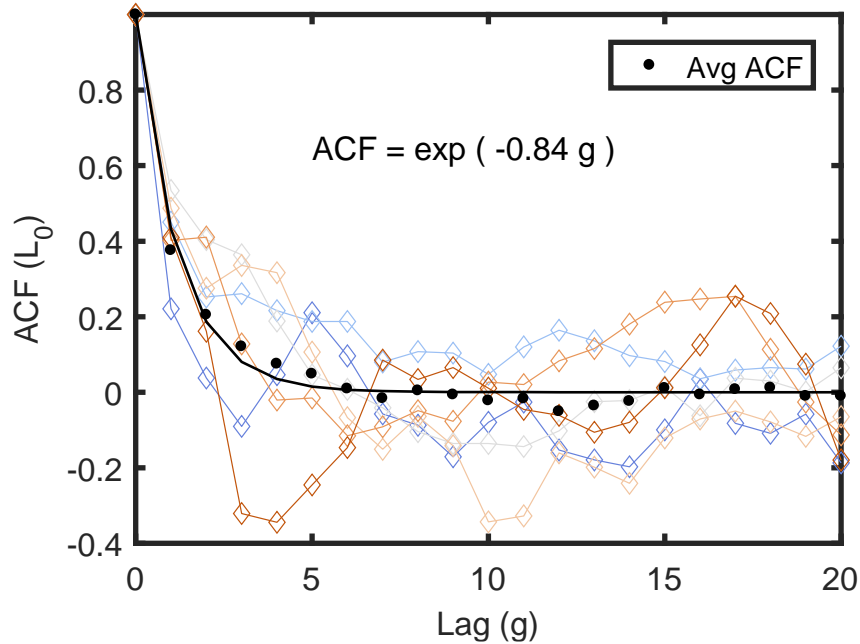


Figure 15 The ACFs of individual lineages measured in separate traps. The ACFs of individual lineages, measured in the same experiment in separate traps in the mother machine, are presented in different colors. Each ACF was calculated from a lineage longer than 150 generations to maximize the statistics. Note that each ACF exhibits distinct dynamical pattern. Averaging all ACFs results in a simple exponentially decaying function with a decay time of ~ 2 generations depicted by the black line in the graph.

3.2 Sisters machine: a new technique for measuring epigenetic cell memory

To overcome this hurdle, we have developed a new measurement technique, which enables us to separate environmental effects from cellular ones. The technique is based on a new microfluidic device that allows trapping two cells immediately after they divide from a single mother simultaneously and sustain them right next to each other for extended time. Thus, with this technique we track the lineages of the two sister cells (SCs) from the time of their birth and follow them as they age together for tens of generations. This enables us to measure how two cells that originate from the same mother become different over time, while experiencing exactly the same environment.

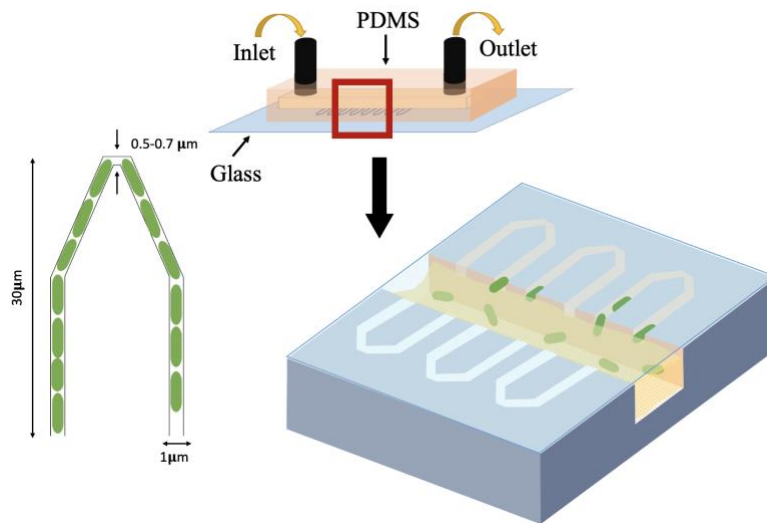


Figure 16 Microfluidic device to trap sister cells. Long ($30\mu\text{m}$) narrow traps ($1\mu\text{m} \times 1\mu\text{m}$) are connected on one end and open on the other to wide ($30\mu\text{m} \times 30\mu\text{m}$) perpendicular flow channels through which fresh medium is pumped. The traps are bent in a Vshape and joined together for successful trapping of sister bacterial cells. The tip is made $\sim 0.5\mu\text{m}$ smaller than the width of the arms to restrict cells from moving from one arm to the other.

Our new microfluidic device, dubbed the "sisters machine" (Figure 16), consists of $30\ \mu\text{m}$ long narrow trapping channels ($1\ \mu\text{m} \times 1\ \mu\text{m}$) open at one end to a wide channel ($30\ \mu\text{m} \times 30\ \mu\text{m}$), through which fresh medium is continuously pumped to supply nutrients to cells in the traps and wash away cells that are pushed out of them (see Chapter 2 for the fabrication details). Here however, every two neighboring trapping channels are joined on the closed end through a v-shaped connection of the same width and height. The tip of the v-shaped connection is made $0.5\ \mu\text{m}$ narrower than the rest of the channel to reduce the likelihood of cells passing from one side to the other (Figure 17A and B).

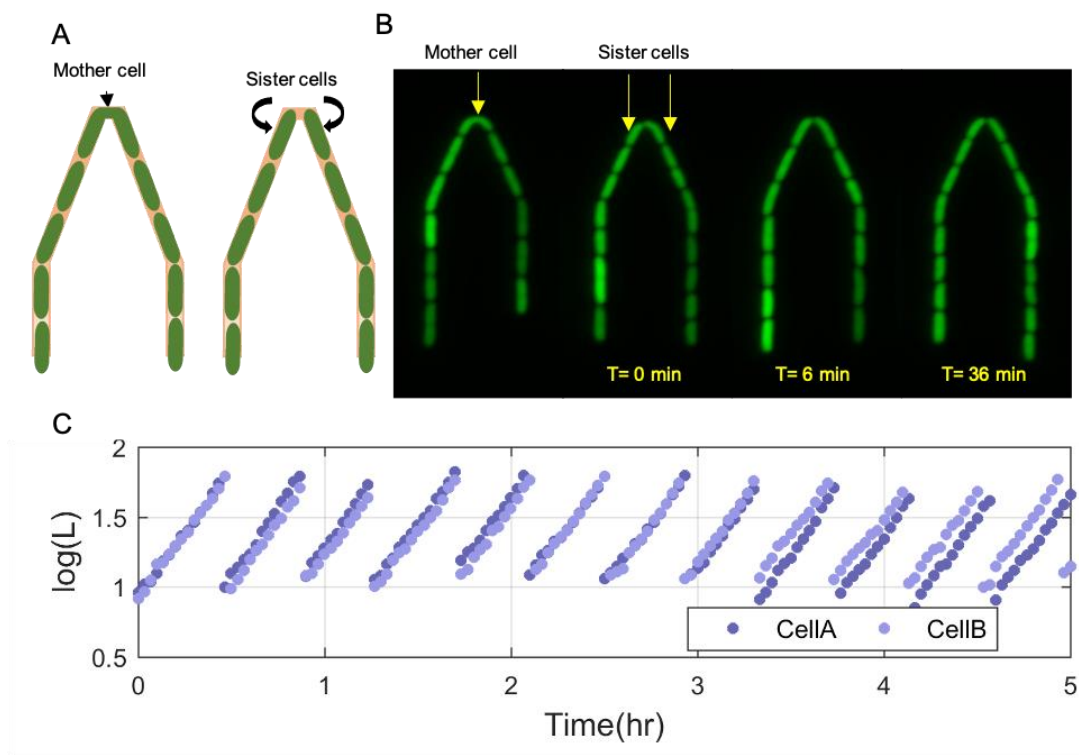


Figure 17 Example measurement of sister cells. (A) Sister cells are formed in two separate arms of the traps when a mother bacterial cells elongates in v-shaped tip. (B) Time lapse images of sisters growing in separate arms of the trap. (C) Lengths of two sister cells growing in the microfluidic device.

Therefore, once it happens, the cells at the tip will remain there, while we track their growth and division events, and measure their size and protein expression (Figure 17C), until the next cell passage occurs, which can take 10s of generations. The environment in this setup is identical for both cells at the tip of the v-shaped connection, as they are kept in close proximity to each other. This ensures that differences observed between the two cells are due to internal cellular factors only.

A comparison of the growth patterns of two pairs of SCs measured in the same experiment, where each pair share a common trap, reveals that while the growth dynamics of SCs are strikingly similar, they are significantly different between the two pairs (Figure 18A). This is further confirmed by comparing the distribution of the difference between the average growth rates of SCs to that of pairs of cells residing in different channels (Figure 18B). These results highlight the significance of the contribution of environmental fluctuations to cellular growth dynamics, and support the existence of different environmental micro-niches within our, and similar, microfluidic setups as mentioned earlier.

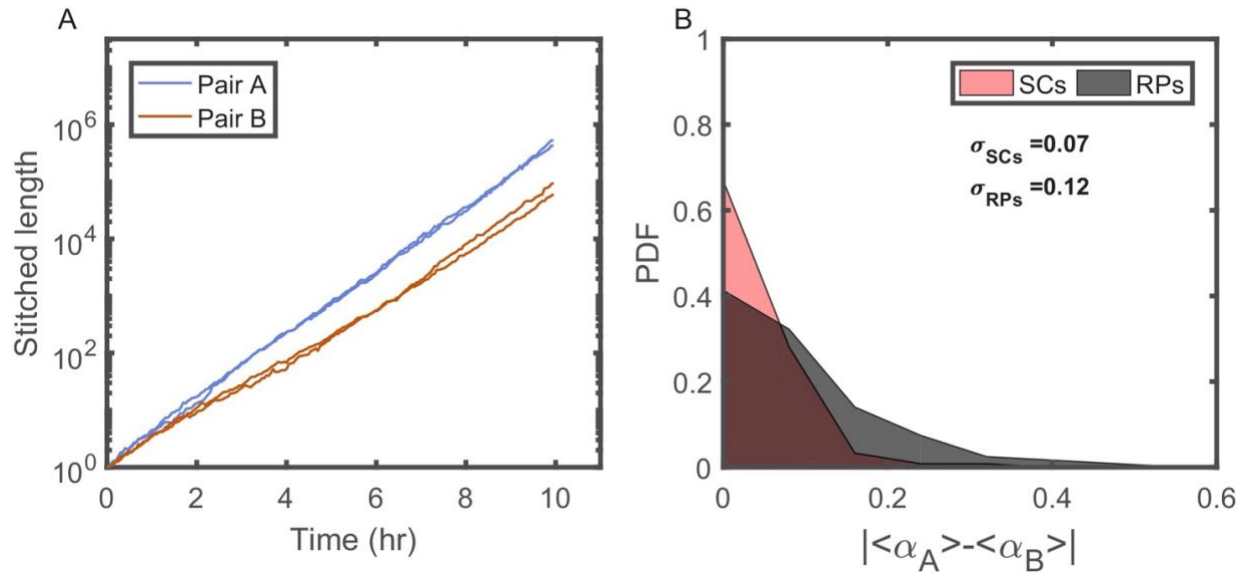


Figure 18 Individuality of cellular growth dynamics in different microenvironments in microfluidic device (A) Depicts the cell length of two pairs of SCs measured in two different V-Shaped traps as a function of time. The length of each cell is presented in a "stitched" form, where the length of the cell in each cell cycle is adjusted to start from the length of the cell at the end of the previous cycle, ignoring by this the division events. This is done by dividing the length in each cycle by the starting length and multiplying it by the length of the cell at the end of the previous cycle. This presentation emphasizes the difference in the average growth rates measured in different traps. Note however, that each pair of SCs exhibits similar average growth rate. **(B) Probability Distribution Function (PDF) of the absolute difference in the average growth rate of two SCs is compared with the absolute difference in the average growth rate of two randomly paired cells (RPs) growing in separate traps in the same device (see Figure 21 for further elaboration on random pairing of cells).** The standard deviation of the difference for SCs (σ_{SCs}) is almost half of the calculated value for RPs (σ_{RPs}). This shows that cells grow with different average growth rate in different traps and supports the idea of micro-niche formation in the microfluidic device.

Note however, that cell division in the new v-shaped channels does not alter the statistics of SCs' relative sizes, growth rates, or generation times, in comparison to that observed in the case of division in straight channels (Figure 19).

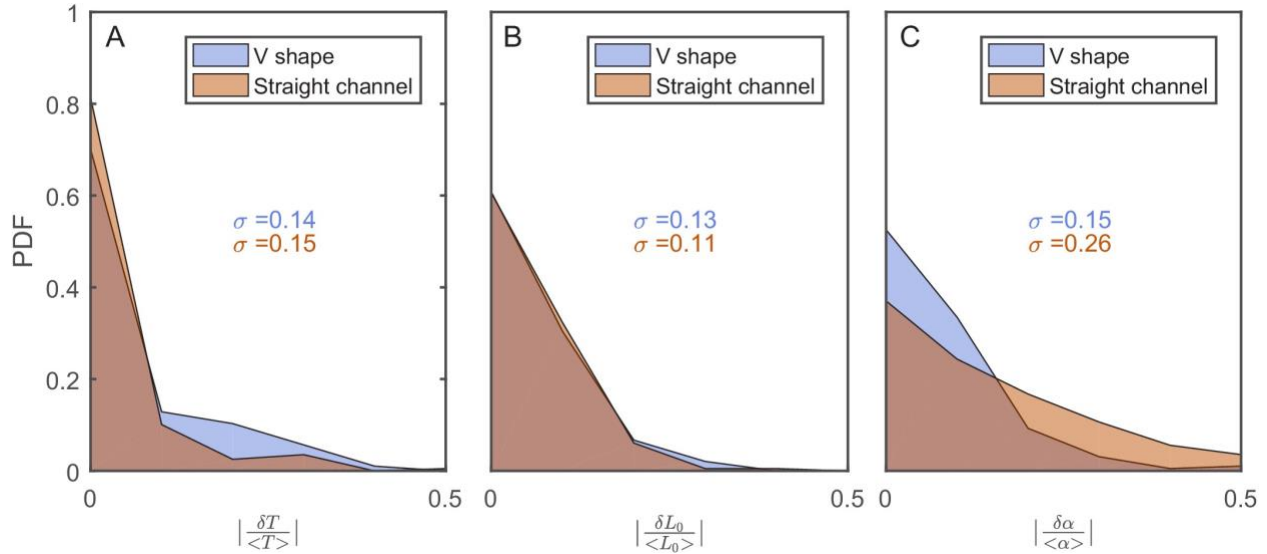


Figure 19 The effect of the v-shaped channel on the distribution of the different cellular characteristics between SCs during division. (A) Probability Distribution function (PDF) of the difference in the first cell cycle time of two sister cells after separation relative to the population's average cycle time under the same experimental conditions. (B) PDF of the difference in cell length between the sister cells immediately after division relative to the population's average length at the start of the cell cycle. (C) PDF of the difference in the growth rate of the two sister cells after separation relative to the population's average growth rate. The difference measured in the straight channels here is larger than that measured in the v-shaped channels. This could be due to the fact that the two cells in the mother machine trap are at different distance from the nutrients diffusing from the flow channel into the traps. This has been shown before to result in variation in the cells growth rate⁸⁴. In all graphs the blue curves represent the distributions measured in our new device with the v-shaped channels using 194 pairs, while the brown curves were measured in the straight channels of the mother machine using 198 pairs.

Using this setup, we successfully trapped pairs of cells next to each other for 20 – 160 generations. Images of the cells in both DIC and fluorescence modes were acquired every 3 minutes. Under our experimental conditions (cells growing in LB medium at 32 °C) the average generation time was 34 ± 7 minutes, which provided ~11 images every generation. The acquired images were used to measure various cellular characteristics as a function of time, including cell size, protein concentration, growth rate, and generation time.

To avoid artifacts arising in our calculations due to slight differences between experiments carried out on different days, we standardized the parameters by subtracting the mean and dividing by the standard deviation for each experiment before proceeding with the desired calculations (Figure 20).

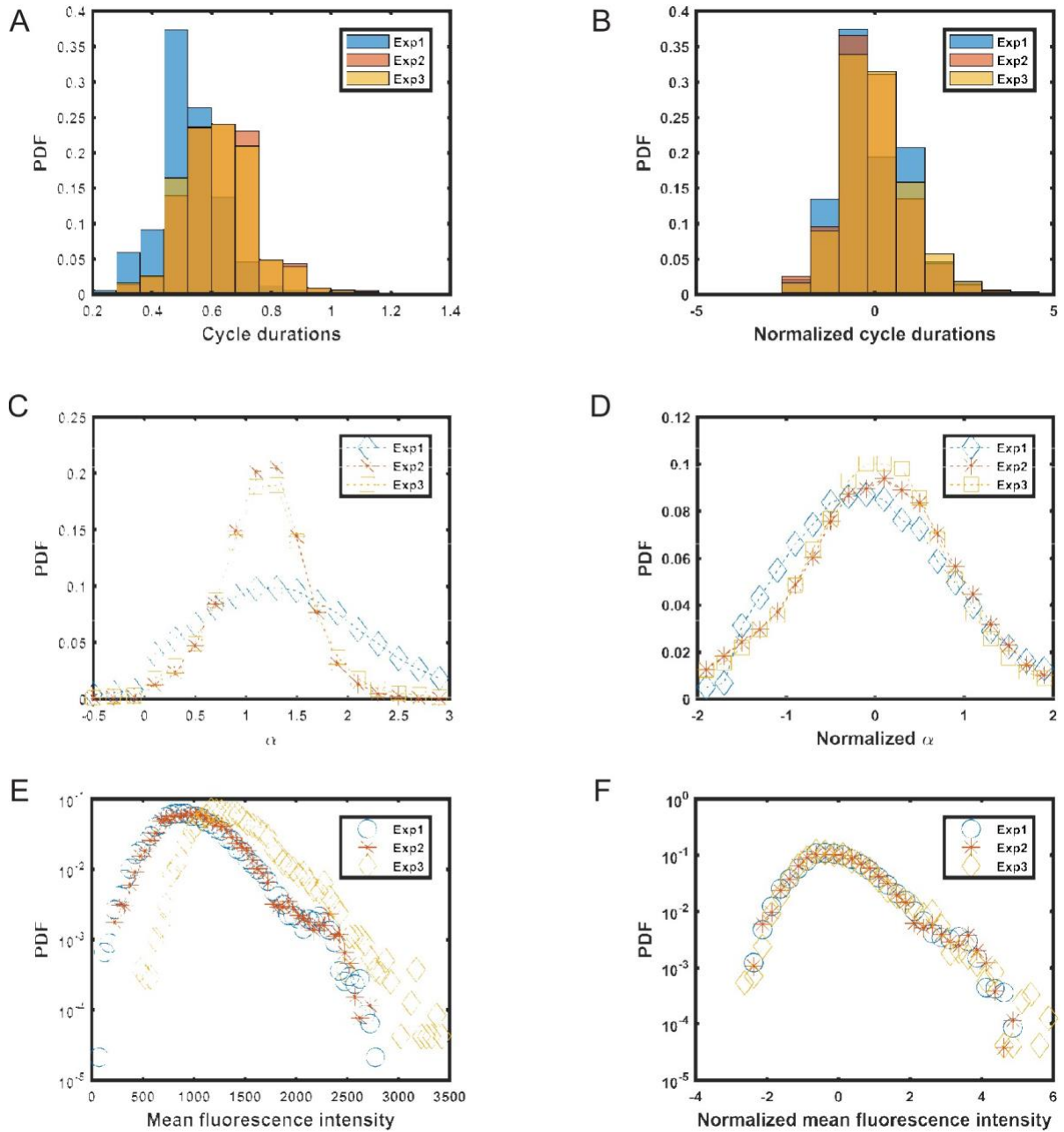


Figure 20 Distributions of different cell parameters. To avoid artifacts arising in calculations due to differences between experiments, raw data from each experiment were normalized by subtracting the mean (μ) and dividing by the standard deviation (σ). (A-B) distributions of cell cycle times (T) before and after normalization. (C-D) distributions of elongation rate (α) before and after normalization. (E-F) distributions of mean fluorescence intensity (f) before and after normalization.

Using this new setup, we were able to measure the cell memory of the different cellular traits. Memory reflects the cell's tendency to pass on its traits to its offspring, and therefore measuring cell memory would allow us to determine how epigenetic inheritance restrain variation in cellular properties over time. To measure cellular memory, we replace the ACF, used in previous studies, with the Pearson correlation function (PCF) between pairs of cells:

$$PCF^y(t) = \frac{1}{\sigma_{y^{(1)}} \cdot \sigma_{y^{(2)}}} \sum_{i=1}^n (y_i^{(1)}(t) - \langle y^{(1)} \rangle) \cdot (y_i^{(2)}(t) - \langle y^{(2)} \rangle)$$

where y is the cellular property of interest, t is the measurement time, n is the number of cell pairs measured, σ_y the population standard deviation of y and (1) and (2) represent the two cells being considered $PCF^y(t)$ is therefore a measure of the correlation between the values of a specific cellular property at time t . We use this correlation function to compare three types of cell pairs (Figure 21): 1) Sister cells (SCs) are cells that originate from the same mother at time 0, and therefore the value of PCF at time 0 is 1. 2) Neighbor cells (NCs) are cells that reside next to each other at the tip of the v-shaped connection. However, NCs are cells that do not originate from the same mother. They are cells that happen to enter into both sides of the same v-shaped channel from the start of the experiment. We initiate their tracking though, only when they happen to divide at the same time, such that at time 0 they are both at the start of a new cell cycle, and if their length is almost identical at that point in time. This choice is to ensure that any long-term correlation measured in SCs does not stem from a size homeostasis mechanism, which would maintain the size of both cells similar for several generations if they start similar. 3) Random cell pairs (RPs) are cells that reside in different traps and their lineages are aligned artificially even though they can be measured at different times. In this case, t is measured relative to the alignment point, which is chosen to be at the start of the cell cycle for both cells. Since NCs and RPs do not originate from

the same mother at time 0, the PCF is measured from the first generation only, and we set it to be 1 at time 0. Comparing the correlation of NCs, which experience the same environmental conditions at the same time, with that of RPs allows us to determine the effect of the environment on the correlation. On the other hand, the comparison of SCs with NCs provides the effect of cellular factors (i.e., epigenetics) that are shared between SCs, on the correlation function. This in turn allows us to determine the cellular memory of a specific property resulting from shared information passed on from the mother to the two sisters.

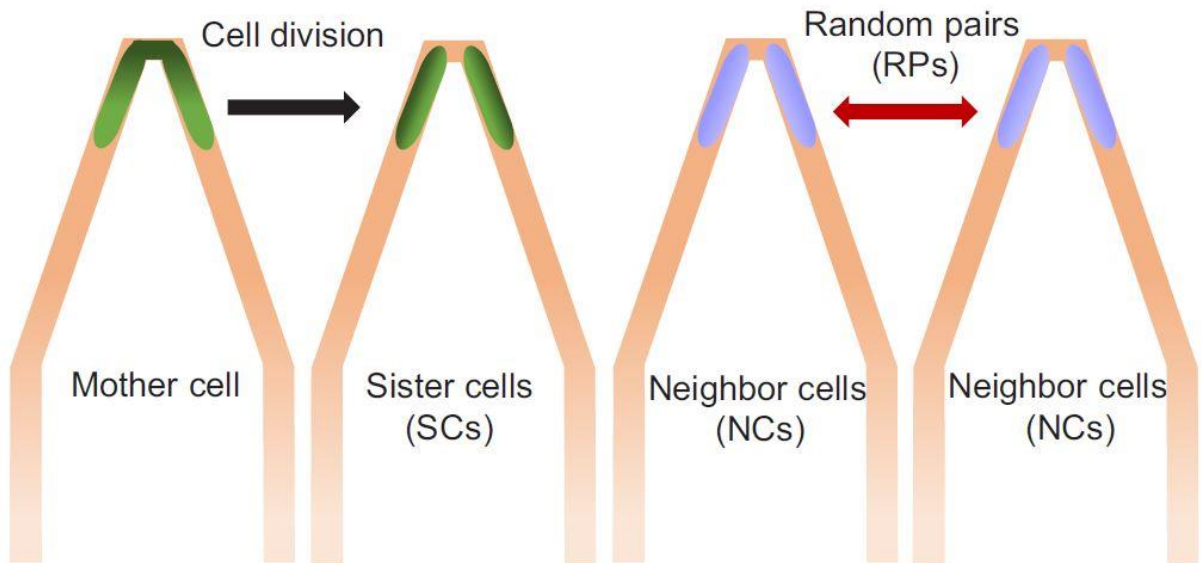


Figure 21 Three types of pairs used for calculating PCF. Sister cells (SCs) are the cells that originate from the same mother and reside in the same trap. Neighbor cells (NCs) do not originate from same mother but reside in the same trap. Random pairs (RPs) neither reside in same traps nor do they have same mother.

3.3 Results: Epigenetic inheritance of cell cycle time and cell size

Using the above-described method, we measured the correlations between the different pair types for cell cycle time (T). We find that T of SCs remain strongly correlated for up to 8 successive cell divisions when measured in LB (complex rich) medium at 32°C (Figure 22 see also Supplementary figures). On the other hand, the NCs correlation decays to zero within 3 generation under the same experimental conditions (Figure 22). These results clearly reveal the effects of epigenetics and environmental conditions on cellular memory when compared to the RPs correlation, which as expected decays to zero within one generation similar to the ACF (dashed red line Figure 22).

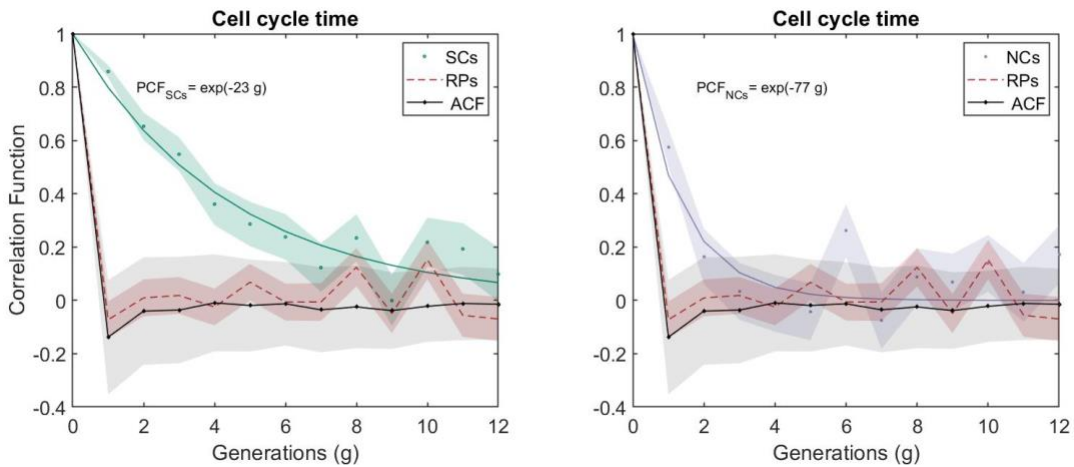


Figure 22 PCF of cell cycle time measured in cell pairs as a function of number of generations. PCF of cell cycle time for SCs (122 pairs from 3 separate experiments) exhibit memory that extends for almost 9 generations (half lifetime ~ 4.5 generations). This is $\sim 3.5x$ longer than the half lifetime of NCs PCF (calculated using a 100 pairs from 3 separate experiments), which is comparable to the ACF (half lifetime ~ 1 generation). Shaded area represents the standard deviation of the average. The equations in the graphs represent the best fit to the PCF depicted in each graph with g is generation number.

Note that this long memory observed here was independent of the environmental conditions of the experiments. Similar correlation between the cell-cycle times of SCs was also observed when the temperature is changed to 37°C, and when the LB medium is replaced with a minimal medium supplemented with lactose (M9CL) at the same temperature as before (32°C) (Figure 23).

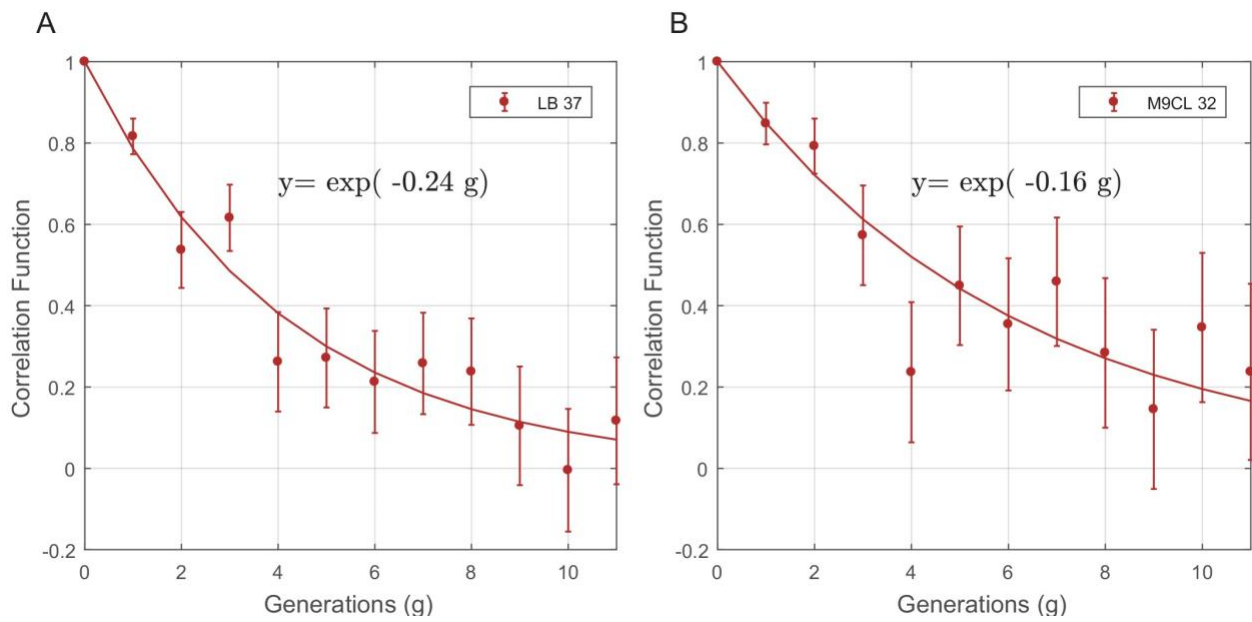


Figure 23 The PCF of cell cycle time (T) for SCs in different growth conditions. The PCF of SCs cell-cycle time in LB at 37°C (57 pairs from 2 separate experiments) (A) and in M9CL at 32°C (29 pairs from 2 separate experiments) (B). Existence of strong correlation between cell cycle duration in both (A) and (B) demonstrates the robustness of non-genetic restraint in different experimental conditions. The lines in both graphs are the best fits to the data depicted in the graphs. The decay rate of the correlation in both cases is very similar to that observed in LB medium at 32°C described in the main text ($y = \exp(-0.23g)$).

Next, we applied our method to cell size. Also, here our measurements show that SCs correlation decays slowly over ~ 7 generations (Figure 24, see also Supplementary figures), while the correlation of NCs exhibit fast decay to zero within 2 generations similar to the ACF (Figure 24). Note that RPs exhibit no correlation from the start of the measurement (dashed red line Figure 24). These results further demonstrate the existence of strong non-genetic memory that restrains the variability of cell size between SCs for a long time. Unlike the cell cycle time however, the effect of both epigenetic factors and environmental conditions on the cellular memory, appears to extend for a slightly shorter time.

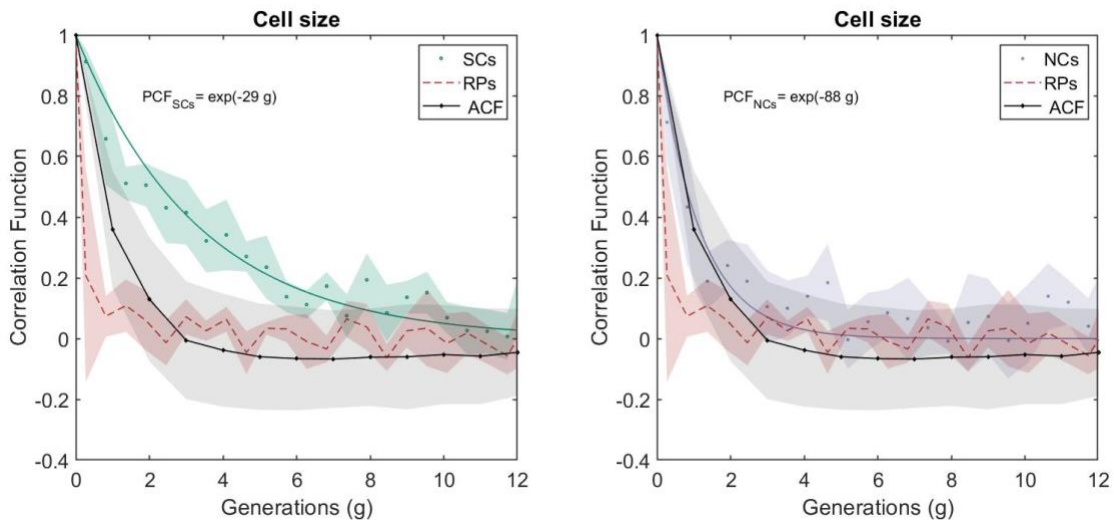


Figure 24 PCF of cell size measured in cell pairs as a function of number of generations. SCs exhibit strong cell size correlation that decays slowly over a long time (half lifetime ~ 3.5 generations), while NCs show almost no correlation in cell size similar to ACF of initial sizes (half lifetime ~ 1 generation). PCF values for cell size were calculated in similar way to cell-cycle time, and were then averaged over a window of six consecutive time frames (15 minutes time window). Shaded area represents the standard deviation of the average. The equations in the graphs represent the best fit to the PCF depicted in each graph with g is generation number.

We also measured the correlation between NCs which do not start from the same initial size to understand whether the correlation that we are observing in the first generation is arising from size homeostasis mechanism. PCF of cell-cycle time (Figure 25A) and cell length (Figure 25B) for NCs starting from random initial sizes are compared in both graphs with ACF and PCF for RPs. NCs starting with random initial sizes show almost no correlation in cell size or cell cycle time similar to RPs.

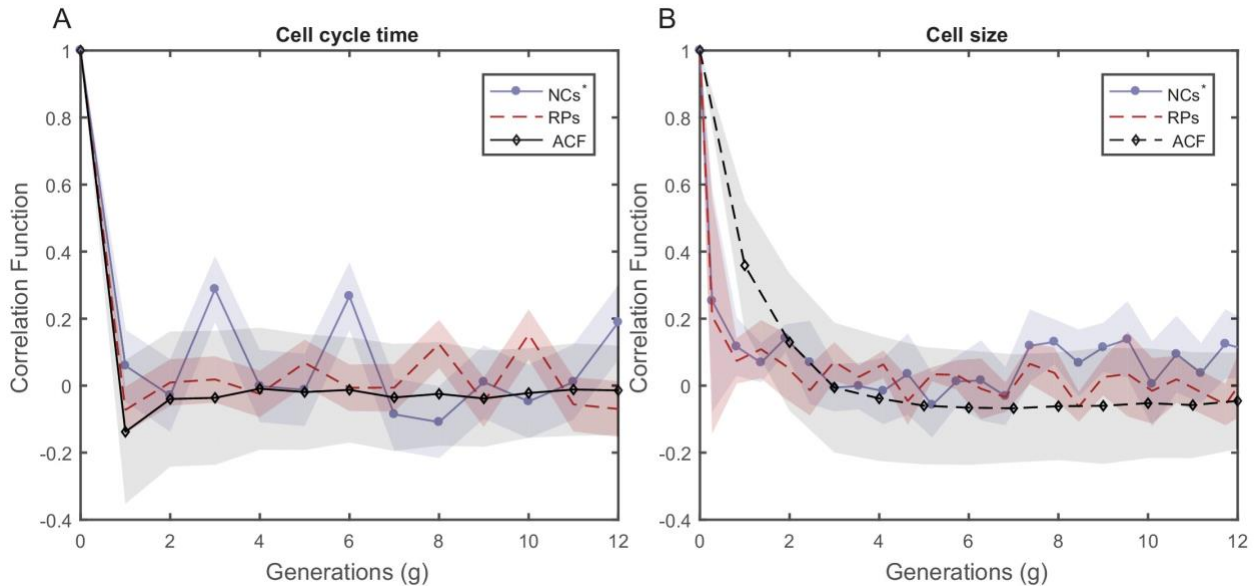


Figure 25 PCF values of cell size and cell cycle duration as a function of time for NCs with different starting size. PCF of cell-cycle time (A) and cell length (B) for NCs starting from random initial sizes are compared in both graphs with ACF and PCF for RPs. NCs starting with random initial sizes show almost no correlation in cell size or cell cycle time similar to RPs.

3.4 Variance as a new parameter to estimate the nature of restraint on variability

To quantify the increase in variability among cells along time differently, we measured the change in the variance of a cellular property as time advances, which is expected to reach an equilibrium saturation value at long timescales. Measuring how the variance reaches saturation, provides information about cellular memory and the nature of forces acting to restrain variation. Assuming that $x(t)$ is a measurable cellular property, such as cells size, or growth rate, etc. We can present it as:

$$x(t) = \bar{x} + \delta x(t)$$

Where \bar{x} is the average of $x(t)$ over time, and $\delta x(t)$ is its fluctuations around \bar{x} . The difference of this measured property between two cells:

$$\Delta x(t) = x_1(t) - x_2(t)$$

Where 1 and 2 represent the two different cells, will average to zero, i.e. $\langle \Delta x \rangle = 0$. Its variance on the other hand will be:

$$\sigma_{\Delta x}^2(t) = \langle \Delta x^2(t) \rangle - \langle \Delta x(t) \rangle^2 = 2 \langle \delta x^2(t) \rangle - 2 \langle \delta x_1(t) \delta x_2(t) \rangle$$

Where $\langle \delta x^2(t) \rangle = \langle \delta x_1^2(t) \rangle = \langle \delta x_2^2(t) \rangle$ is the variance of x , which is the same for all cells, and $\langle \delta x_1(t) \delta x_2(t) \rangle$ is the covariance of the fluctuations in both cells, which when normalized by $\sigma_{\delta x_1} \cdot \sigma_{\delta x_2}$ would give the correlation, i.e. the Pearson Correlation Function (PCF), between the two variables.

On the other hand, if we assume that x is determined by two factors, internal cellular composition $I(t)$ and external environmental conditions $E(t)$ such that:

$$x(t) = I(t) + E(t)$$

Then $\sigma_{\Delta x}^2(t) = \langle [(I_1 - I_2) + (E_1 - E_2)]^2 \rangle$ would depend on whether the two cells share the same environment and/or the same cellular compositions. Therefore, random pair of cells (RPs), which reside in different channels and thus do not share neither the environment nor the internal composition would exhibit a variance:

$$RPs: \sigma_{\Delta x}^2(t) = 2\sigma_I^2 + 2\sigma_E^2 + 4cov(I, E)$$

Where $\sigma_I^2 = \langle I^2 \rangle - \langle I \rangle^2$ is the variance in the internal composition of the cell (similar for all cells and constant over time), $\sigma_E^2 = \langle E^2 \rangle - \langle E \rangle^2$ is the variance in the environmental conditions (also the same for all cells in the same experiment), and $cov(I, E)$, is the covariance of the environment and the internal composition of the cell, which as discussed earlier can influence each other in a trap-specific manner. However, averaging many measurements from different traps erases this effect²⁵ as clear from Figure 15

For cells that share the environment but not their internal composition, i.e., neighboring cells (NCs), the variance would be:

$$NCs: \sigma_{\Delta x}^2(t) = 2\sigma_I^2$$

Note that when the NCs are chosen to have similar size and divide simultaneously at time zero, this variance for cell size would be small initially but its increase would not be constrained by the epigenetic similarity between the two cells as in the case of sister cells (SCs).

And finally, for SCs, which share both the environment and their internal composition, which means that I_1 and I_2 can be correlated, then:

$$SCs: \sigma_{\Delta x}^2(t) = 2\sigma_I^2 - 2cov(I_1, I_2)$$

Where $cov(I_1, I_2)$ is the covariance of the internal states of the cells as a function of time, i.e. the non-genetic memory of the cell.

Using the definitions above, it is easy to see the relationship between the variance and the PCF. It is also clear that the difference between NCs and RPs variances would provide the contribution of the environment, while the difference between SCs and NCs variances would give the contribution of the internal composition of the cell to the variance, or the epigenetic memory.

The cellular memories of cell cycle time and length, measured using this method, agree well with our previous PCF results (Figure 26 and Figure 27).

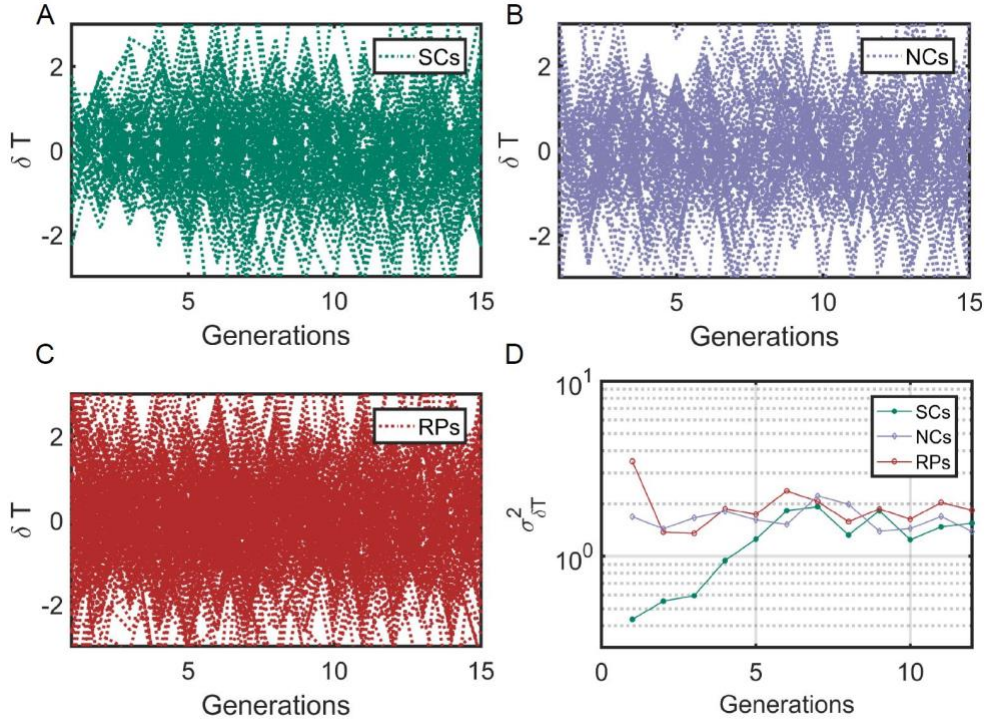


Figure 26 Cell-cycle time variance ($\sigma^2_{\delta T}$) as a function of time. (A-C) Individual traces showing difference in cell cycle times (δT) for SCs, NCs and RPs respectively. The variance (σ^2) of cell cycles times differences (δT) as a function of time (D) represent the variance of the plots in (A-C) calculated at different time points using $\sigma^2_{\delta T} = \langle \delta T^2 \rangle - \langle \delta T \rangle^2$ for SCs starts from a small value in first generation and saturate to a constant value after ~ 7 generations (similar to the timescale obtained from the PCF ~ 8 generations), while $\sigma^2_{\delta T}$ for NCs and RPs remain constant over time.

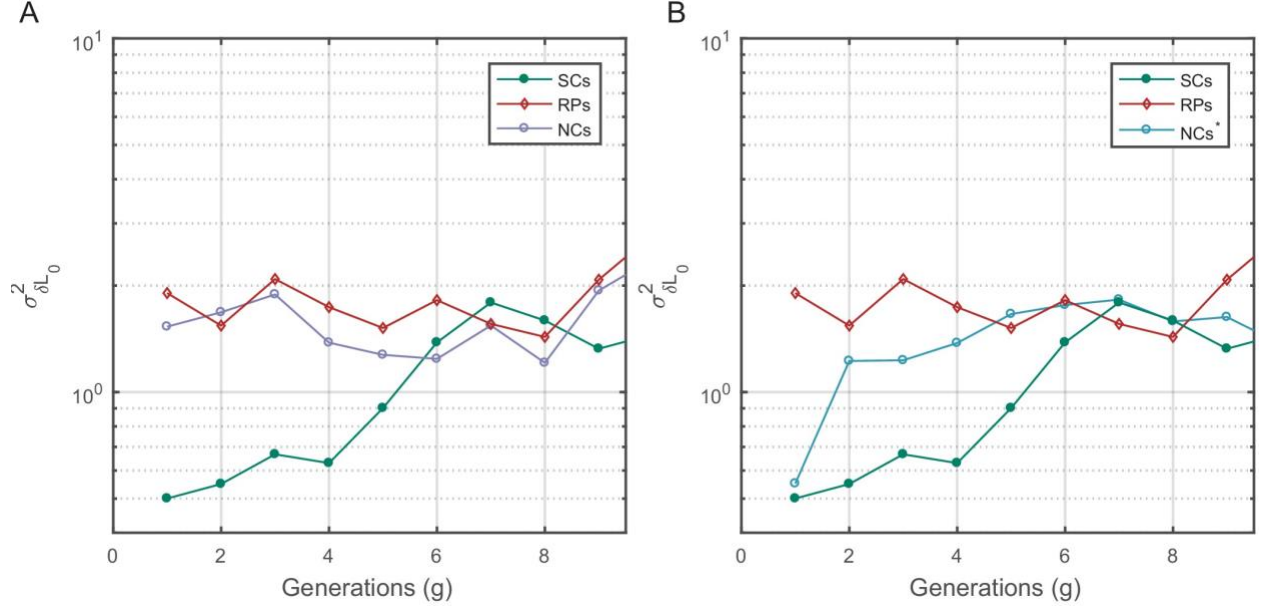


Figure 27 Cell size variance ($\sigma^2_{\delta L_0}$) as a function of time. Birth size variance was calculated similar to $\sigma^2_{\delta T}$ in Figure 26. $\sigma^2_{\delta L_0}$ for SCs increases slowly and saturates at a fixed value after ~ 7 generations (mean lifetime ~ 3.5 generations) similar to the time scale observed in the PCF. For NCs with random initial sizes (A), $\sigma^2_{\delta L_0}$ remains constant similar to RPs. $\sigma^2_{\delta L_0}$ for NCs with similar birth sizes starts from a value similar to SCs but shoots up to the saturation value within 1 generation.

Thus, we have measured the relative fluctuations in the exponential elongation rate of cell pairs $\delta\alpha$ defined as:

$$\delta\alpha(t) = \alpha_1(t) - \alpha_2(t)$$

Where $\delta\alpha(t) = \frac{d \ln L}{dt}$ is the exponential elongation rate of the cell, $L(t)$ is the cell length at time t , and (1) and (2) distinguish the cell pair (Figure 28 A-C). As expected, $\delta\alpha(t)$ for all pairs of lineages is randomly distributed with $\langle \delta\alpha(t) \rangle = 0$, (Figure 28D), as the elongation rate of all cells fluctuate about a fixed value identical for all cells in the population and depends on the experimental conditions.

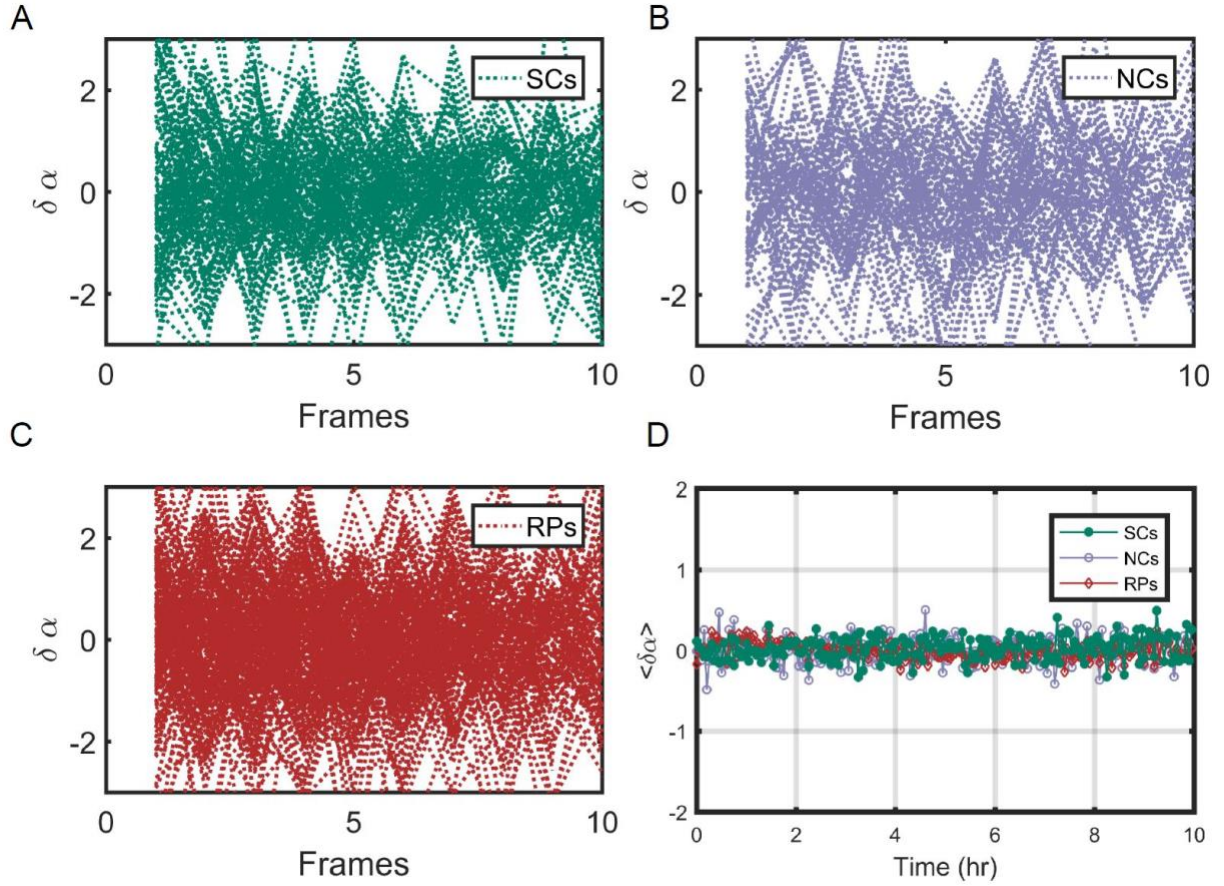


Figure 28 Exponential elongation rate difference ($\delta\alpha$) as a function of time. Individual traces showing the difference between the exponential elongation rates for SCs (A), NCs (B), and RPs (C). (D) The mean of ($\delta\alpha$) for all cell pairs remain zero along time as expected. For details of ($\delta\alpha$) calculations, please refer to the main text.

The variance of $\delta\alpha(t)$ for both RPs ($\sigma_{\delta\alpha_{RPs}}^2$) and NCs ($\sigma_{\delta\alpha_{NCs}}^2$) was found to be constant over time and is similar for both types of cell pairs (Figure 29). However, the variance of $\delta\alpha(t)$ for SCs ($\sigma_{\delta\alpha_{SCs}}^2$) exhibits a complex pattern, which eventually converges to the same value as RPs ($\sigma_{\delta\alpha_{RPs}}^2$) and NCs ($\sigma_{\delta\alpha_{NCs}}^2$).

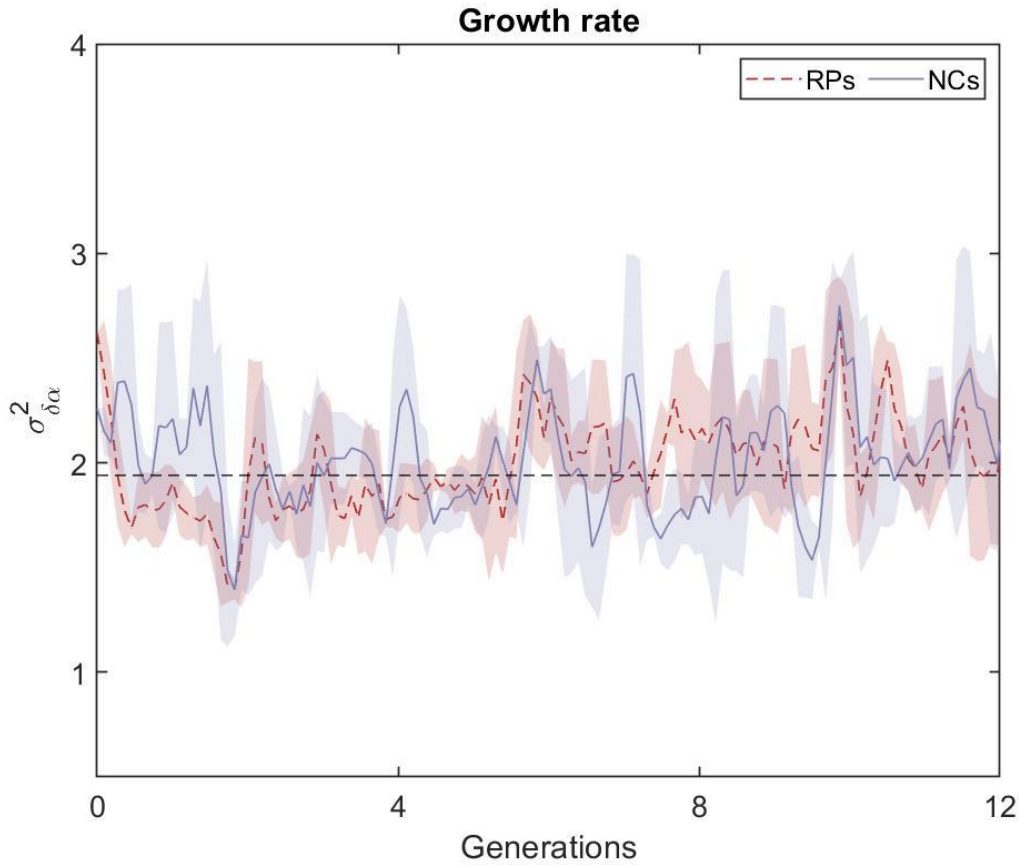


Figure 29 Variance ($\sigma_{\delta\alpha}^2$) as a function of the time. (A) Variance of the growth rate difference between cell pairs for NCs and RPs as a function of time (see main text for the details of the calculation). The variance remains constant for both the pairs.

Figure 30 shows that unlike cell cycle time and cell length, the elongation rates of SCs immediately after their division from a single mother exhibit the largest variation. This variation decreases to its minimum value within a single cell cycle time (~30 min). Following this decrease, the variance increases slowly to reach the same saturation value measured for NCs and RPs. The time it takes for $\sigma_{\delta\alpha_{SCs}}^2$ to reach saturation extends over almost 8 generations, which again reflects a long memory resulting from epigenetic factors.

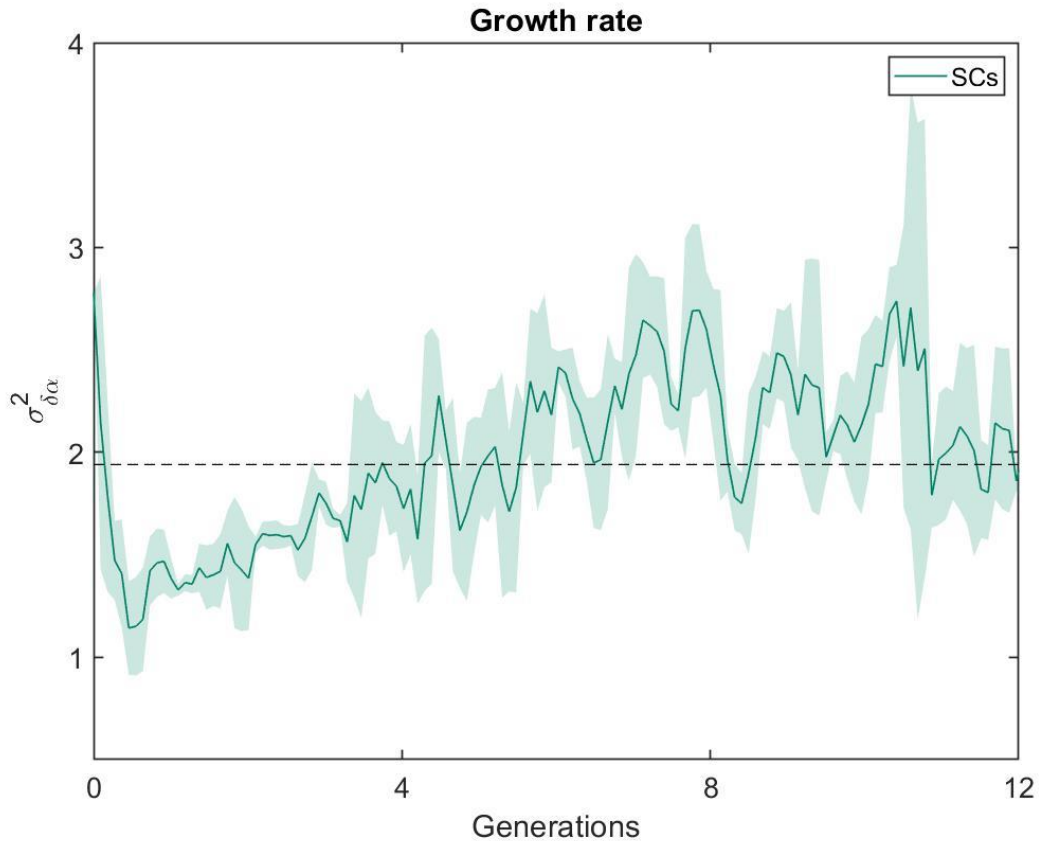


Figure 30 Variance ($\sigma^2_{\delta a}$) as a function of the time. Variance of SC exhibits large variance immediately after separation (~50percent higher than NCs and RPs) and rapidly drops to its minimum value within one generation time(~30 minutes), and increases thereafter for 4 hours (~8 generations) until saturating at a fixed value equivalent to that observed for NCs and RPs. Each point is the average over 3 frames moving window, and the shaded area represent the standard deviation of that average.

To understand the source of this large variation immediately following separation, we have measured the growth rate over a moving time window of 6 minutes throughout the cell cycle, and compared the results between SCs. Our comparison clearly shows that a sister cell that receives a smaller size-fraction from its mother exhibits a larger growth rate immediately after division. The growth rate difference between the small and large sisters, decreases to almost zero by the end of

the first cell cycle after separation (Figure 31). This result reveals that the exponential growth rate of a cell immediately after division inversely scales with the size-fraction the cell receives from its mother⁸⁵. It also demonstrates that the difference in the growth rates between SCs changes during the cell cycle indicating that they are not constant throughout the whole cycle as has been accepted so far^{24,86,87}. Note that similar results have been reported recently for *Bacillus subtilis*⁸⁸, where it was observed that the growth rate is inversely proportional to the cell size at the start of the cell cycle, and changes as the cell cycle advances.

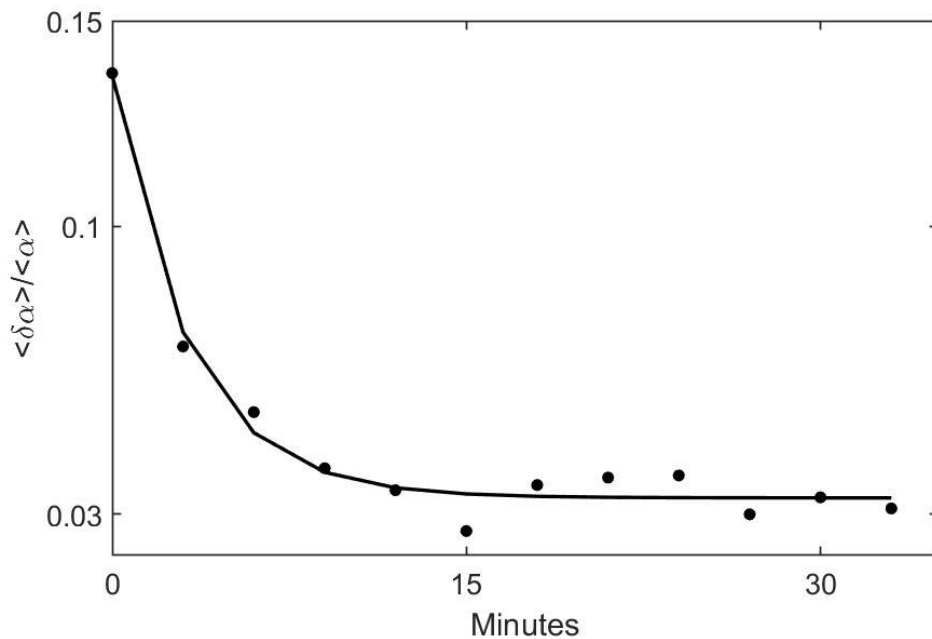


Figure 31 Average growth rate difference between sister cells in first cell cycle. The growth rate difference was calculated by subtracting the growth rate of larger sister from the growth rate of smaller one over a moving time window of 6 minutes throughout the cell cycle. SC that receives a smaller size-fraction from its mother exhibits a larger growth rate immediately after division. The growth rate difference between the small and large sisters, decreases to almost zero by the end of the first cell cycle after separation.

We have also examined how the protein concentration varies over time between the two cells by measuring the concentration of GFP (green fluorescent protein), via its fluorescence intensity, expressed from a constitutive promoter in a medium copy-number plasmid. The variance of fluorescence intensity difference between cell pairs $\delta f(t)$ was calculated as for the growth rate (see Figure 33 for details). Upon division, soluble proteins are partitioned symmetrically with both daughters receiving almost the same protein concentration. As expected, $\sigma_{\delta f_{SCS}}^2$ starts from ~ 0 initially and diverges to reach saturation within 2 generations (Figure 32). On the other hand, NCs and RPs exhibit constant variance throughout the whole time, with $\sigma_{\delta f_{RPs}}^2$ twice as large as $\sigma_{\delta f_{NCs}}^2$ which reflects the influence of the shared environment resulting in additional correlations between NCs. The relatively short-term memory in protein concentration, may be protein specific (Figure 33), or it could reflect the fact that in this case the protein is expressed from a plasmid. Nevertheless, this result indicates that cellular properties are controlled differently and can exhibit distinct memory patterns. It is important therefore to distinguish between different cellular characteristics and to examine their inheritance patterns individually.

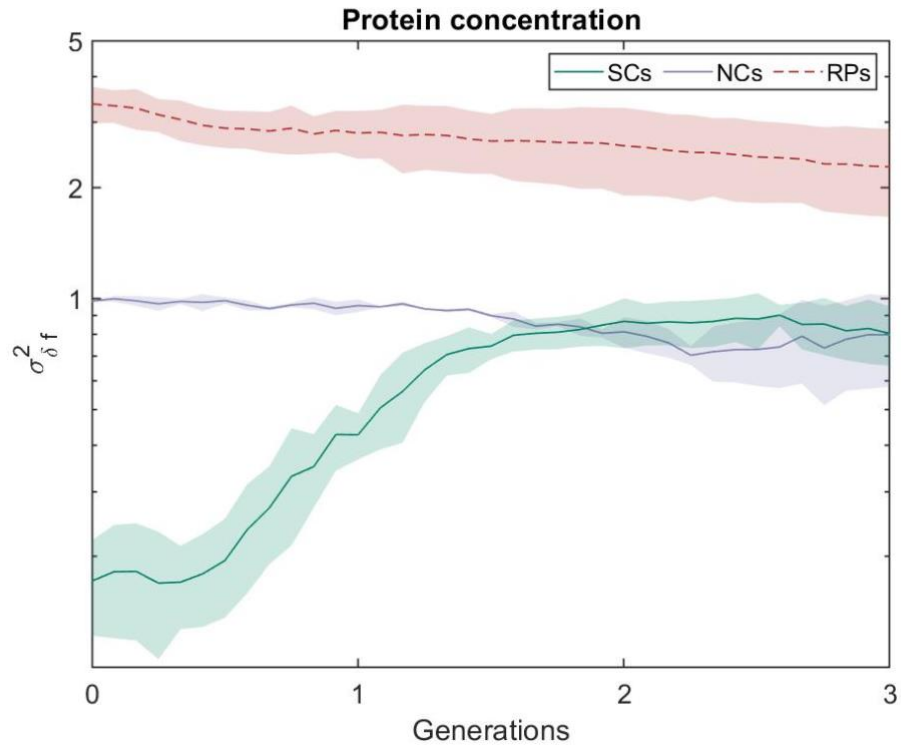


Figure 32 Variance of protein concentration. Unlike $\delta\alpha$, Variance in protein concentration (δf) of SCs increases to its saturation value within ~2 generation (see Figure 33 for the details of the calculation). On the other hand, the variance for NCs, and RPs remain fairly constant throughout. Here, each point represents the average of three different experiments, and the shaded part represents the standard deviation.

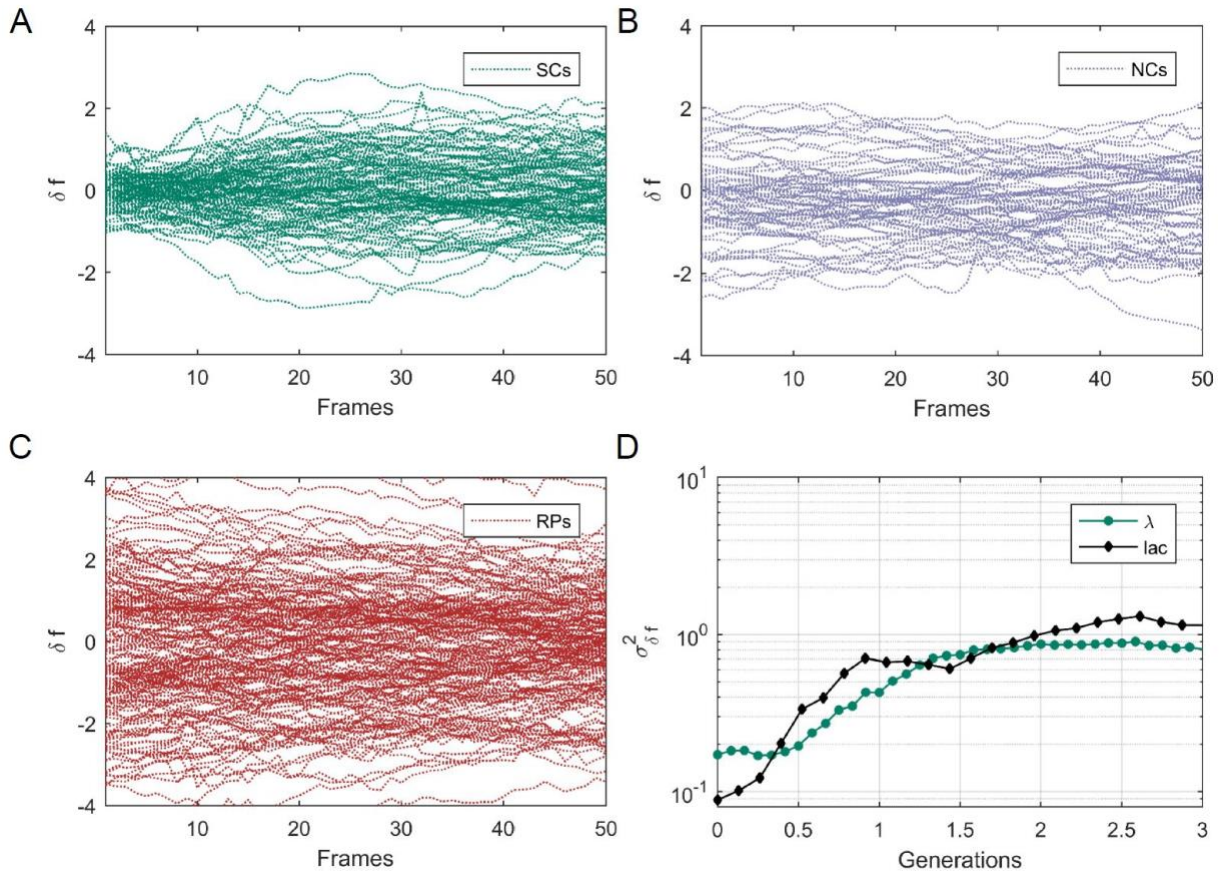


Figure 33 Mean fluorescence variance ($\sigma^2_{\delta f}$) as a function of time. Individual traces showing the difference in mean fluorescence intensity (δf) of *gfp* expressed under the control of λ promoter embedded into the medium copy-number plasmid pZA, in SCs (A), NCs (B), and RPs (C). These traces were used to calculate the variance of δf as described earlier for $\delta\alpha$. (D) The variance ($\sigma^2_{\delta f}$) of GFP expressed under the control of the Lac Operon promoter in lactose medium (metabolically relevant) is compared with that of GFP expressed under the control of the λ Pr promoter in LB medium (metabolically irrelevant). It is clear that both exhibit no significant difference and a very short memory (~2 generations).

3.5 Effect of antibiotics on sisters correlation

Our results in the previous section showed that non genetic memory in bacteria can persist for several generations. Also, the strength and longevity of this memory was similar in different environmental conditions. Motivated by the results of the previous section we explored the robustness of non-genetic inheritance in the presence of stressful environmental conditions. To test this, we decided to probe the strength of correlation between sister cells in the presence of antibiotics. When cells do not have any resistant gene to alleviate the stress introduced due to antibiotics, they cannot survive at very high antibiotic doses. However, at smaller antibiotic doses cells are able to survive the stress to some extent. The mechanism used by the cells to enable their survival under such stressful conditions, can vary depending on the stress type. It has been suggested though, that when the stress is unforeseen before, cells find a solution through a random search algorithm and rearrangement of their gene expression profile^{4,33,89,90}. To investigate it further, we first calculated the minimum inhibitory concentration (MIC) of the cells by growing bacterial cultures with different concentrations of ampicillin. We grew MG1655 *E. coli* bacteria at 32°C in LB with constant shaking at 240 rpm and following day re-diluted the culture in the same medium to an initial OD_{600nm} of 0.01. The culture was then divided into six tubes and each tube was supplemented with a different concentration of ampicillin. Using a plate reader (Infinite 200, TECAN) we measured the OD_{600nm} of the cells every 5 mins for 9 hours to calculate the growth curves of the bacterial cultures at different antibiotic concentrations. Our results showed that bacterial cells could not grow at antibiotic concentrations greater than 1 $\mu\text{g}/\text{ml}$ but managed to grow at concentrations lower than this (Figure 34). Thus, we estimated the MIC of the cells to be 1 $\mu\text{g}/\text{ml}$.

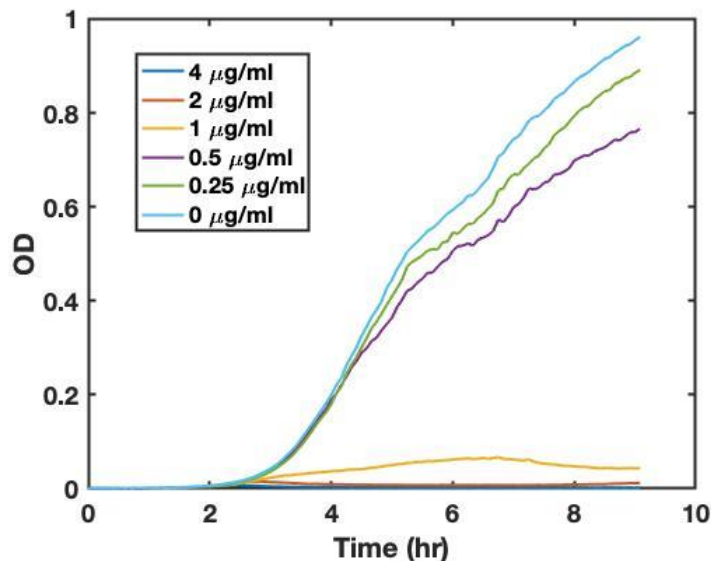


Figure 34 Optical density(O.D.) of bacterial cultures as a function of time at different antibiotic concentrations.

Batch culture experiments show that cells are able to survive ampicillin concentrations below MIC but do not provide information about the cellular response at the single-cell level. To examine the response of the cells in the stressful environment at the single-cell level we performed experiments in our newly developed microfluidic device the “Sisters machine”. Following the standard procedure described previously, we grew bacterial cells without antibiotics and loaded the cells into the microfluidic device. We then subjected these cells to two different ampicillin concentrations, $0.15 \mu\text{g/ml}$ and $0.20 \mu\text{g/ml}$, which are much lower than the MIC to introduce a mildly stressful environment.

We calculated the Pearson Correlation Function (*PCF*) for the cell-cycle time (*T*) of the sister cells. We observed that the correlation strength of the cell-cycle duration was much lower in

the presence of antibiotics (Figure 35). Comparison of the decay rate of the PCF shows that the correlation strength decays faster with the increase in stress level.

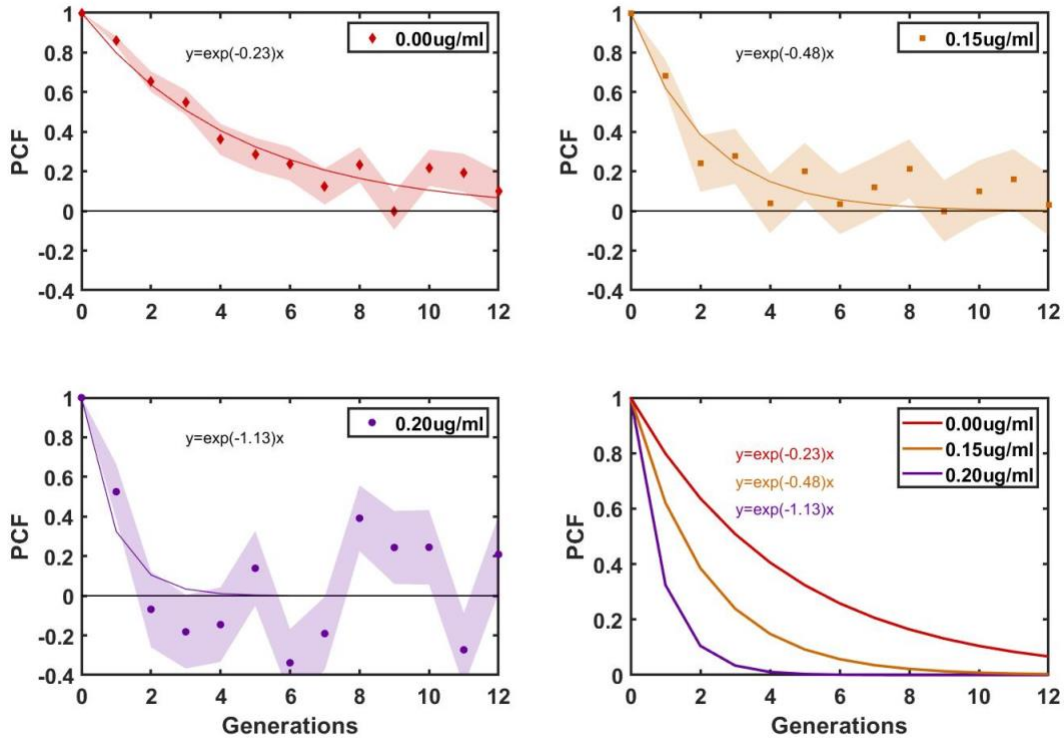


Figure 35 PCF of cell cycle durations at different antibiotic concentrations. In absence of environmental stress, PCF of cell cycle duration between SCs exhibit memory that extends for almost 9 generations but in presence of mild environmental stress the memory is shortened to 4 generation(0.15 $\mu\text{g/ml}$) and 2 generations(0.20 $\mu\text{g/ml}$).

One possible explanation of this behavior is that the genetic network that determines cellular properties, is optimized under normal growth conditions but when challenged with a new stressful condition adopts a wide range of pathways to cope with the situation. This available range

of expression allows the sister cells to respond differently to stressful situations leading to the loss of correlation in their cellular properties. This result demands a thorough investigation of how cells adapt to novel stressful situations by changing the way they express different genes. It also demonstrates how our newly developed method, namely the sisters machine, can contribute to important questions in biology. Understanding how bacteria cope with new stressful conditions and investigating their response dynamics at the single-cell level has been a central goal of biophysics research for decades. The comparison of the response of two sister cells to stressful conditions in a quantitative way, which we present here for the first time, is an important step towards that goal that will aid in future studies of this questions. Further studies following this direction of research are still needed in order to answer this question, some of which are currently being carried out in our lab.

3.6 Conclusions

In this section of the study, we investigated the non-genetic inheritance dynamics in the bacterium *E. coli*. We developed a new experimental method that can trap bacterial sister cells for 10s of generations in the same environment and generate high throughput single cell data of their cell size and protein content. We showed that non genetic bacterial memory cannot be estimated by measuring the average autocorrelation function of cell properties as it can be affected by microniches created in different traps of the experimental setup, as well as by temporal fluctuations in the microenvironment. We compared the PCFs of different cell properties, between sister cells and between cells which are not related to each other to show the contribution of epigenetic inheritance in maintaining the cellular properties over time. Our results show that cells exhibit

different levels of restraint on different properties. Cell size and cell-cycle duration, for example, show long-term memory of about 10 generations, while other properties such as the concentration of a specific protein is not restrained effectively and displays a memory for about 2 generations. We also calculated the difference between the growth rates of sister cells after their birth. We found the difference is maximum immediately after birth but become minimum by the end of the first cell cycle. This difference slowly grows and saturates within the following 8 generations, again emphasizing the effect of epigenetics in restraining the divergence between the growth rates of sister cells. This result also reveals that the division asymmetry plays an important role in determining the growth rate of cells after division. The sister cell receiving the smaller fraction of the mother grows faster than its larger sister. The exact mechanism underlying this effect is a subject of further investigation in our lab and beyond the scope of this study. We can speculate about a possible mechanism however, which is associated with the difference in the DNA concentration between the sister cells. In the smaller sister, DNA is densely packed in a smaller volume in comparison to the other sister. This could affect the process of transcription that depends on the diffusion of RNAP (RNA polymerase) and its binding to the DNA to initiate the production of proteins required for cell growth. A smaller volume may assist the RNAP in its search for target sites and thus drive a faster growth. We also tested the effect of environmental stress on the inheritance dynamics and the strength of the associated non-genetic memory by subjecting sister cells to low antibiotic concentrations. We found that an increase in environmental stress results in a faster decay of non-genetic memory in these cells. We suspect that the faster decay in correlation results from the randomization in the gene expression profiles of the sister cells in the presence of stress. This however, remains to be investigated further in future studies.

Beyond shedding light on the importance of non-genetic inheritance in maintaining cellular properties and restraining the spread of heterogeneity in future generations, this study highlights the usefulness of our new methodology in investigating several central questions in biology. This includes revealing the molecular mechanism controlling the cell's growth rate, as well as understanding the strategies allowing cells to cope with new unforeseen challenges and enabling them to grow in stressful conditions. The full scope of possible studies to which our new method can contribute remain to be seen.

4.0 The contribution of Min proteins and their dynamics to cell size control

Having the right size in a given environment provides survival advantage to different species. Therefore, all species have evolved mechanisms to control their shapes and size to survive, search for food, avoid predators etc. Unicellular organisms like bacteria proliferate in a variety of environments that put selective pressure on their cell size as well. A recent study demonstrated that fitness of bacteria correlates with its cell size in a fluctuating environment⁹¹. Other experimental studies have shown that *E. coli* maintains its size in a very narrow range around a mean value in each environment⁹². These results suggest that there exists a strict mechanism that helps this bacterium maintain its size. Nevertheless, after decades of extensive research, the exact mechanism of size control in bacteria is still unknown. Several phenomenological models, as I discussed in Chapter 1, have been proposed to explain experimental data. These models rely on simple mapping of cellular growth and division dynamics and are successful in explaining experimental observations at the average population level but do not reflect an exact mechanism at the single-cell level. For example, the most accepted model of size homeostasis, the adder model, proposes that cells add a constant volume during their cell cycles irrespective of their birth size which helps them correct for size fluctuations over time. We used our data to verify the adder model and found it to be true at the population level (Figure 36). However, when we compared the difference in volume added by two daughter cells in their cell cycle after birth, we found that the cell that receives a smaller fraction of the mother cell adds more volume during its cell cycle compared to its bigger sibling (Figure 37). This observation reveals that cell size control is a complex process that cannot be fully explained by the adder model at a single-cell level and might combine several mechanisms that operate collectively to bring about the observed behavior.

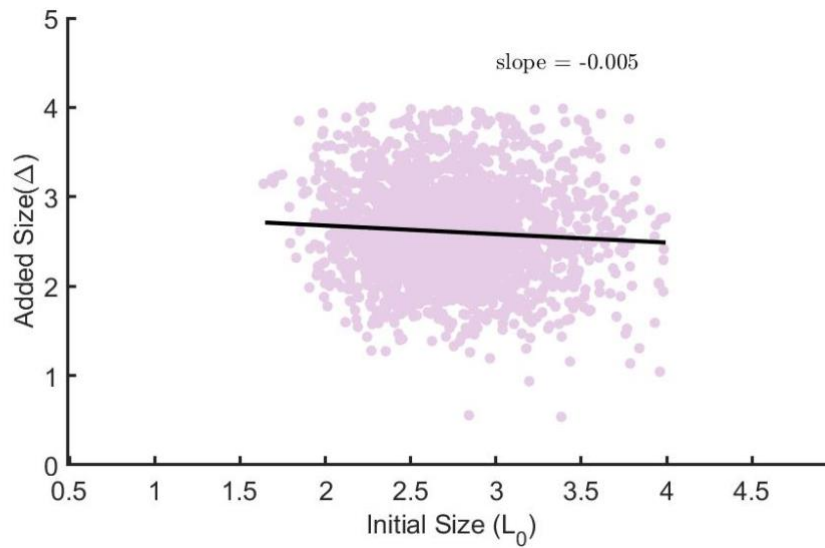


Figure 36 Added size as a function of Initial size. The value of slope very close to 0 suggests that *E. coli* cells, on average, add a fixed size during each cycle irrespective of their birth size. This corroborates the Adder model for cell size homeostasis.

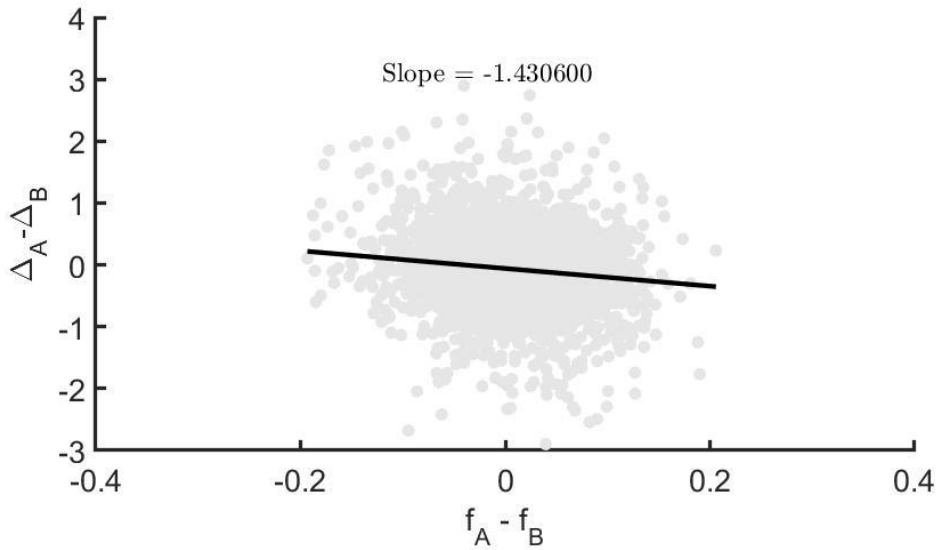


Figure 37 Difference in added size of sister cells as a function of difference in their fractions. Negative slope of the fitted line shows that smaller sister adds more size than its larger sister.

In a recent study it was proposed that the adder phenomenon can be simply explained if there is a specific protein in the cell that accumulates to a threshold amount before the cell can divide. Such protein was suggested, will be able to determine the added size since it will have to reach a specific amount rather than concentration, which depends on cell size. This requirement removes any dependence on the actual cell size and therefore can determine how much volume will a cell add as the protein accumulates in the cell. An obvious candidate protein for such mechanism is the FtsZ, which forms the septal ring and drive cell division. The FtsZ is required in the cell at a certain amount sufficient for completing the septal ring, which upon completion initiates self-contraction in order to form new cellular poles and divide a cell into two daughter cells^{93,94}. Tests of this hypothesis have revealed strong correlations between FtsZ accumulation in the cell and the added volume, which supports a mechanism by which the added size is determined by the need to accumulate FtsZ to a threshold value³⁶. This mechanism, however, fails to explain the difference in added volume that we observe between sisters. Assuming that the FtsZ is divided equally between sister cells, then the time needed for reaching a threshold number of FtsZ molecules required to initiate cell division would be similar for both cells, and therefore, the added volume should be the same for both sisters. Our observation on the other hand shows that smaller sisters add more volume on average than their larger sisters.

Additionally, the FtsZ does not operate independently in the cell. It has been demonstrated in many studies that the placement of FtsZ in the cell is determined by oscillatory dynamics of membrane-associated proteins, collectively termed the Min system. One of these proteins, MinD can be found in two forms, ATP-associated form (MinD-ATP) and ADP-associated form (MinD-ADP). MinD-ATP binds to the cell membrane and recruits MinC, which in turn prevents the binding of FtsZ to the membrane. A third Min protein, namely MinE, chases the MinCD complex

and hydrolyzes MinD-ATP, which breaks this complex and causes it to dissociate from the membrane. Free MinD-ADP and MinC then can diffuse in the cytoplasm, where MinD-ADP can be converted back to MinD-ATP and bind to the membrane at different locations. This interplay between the proteins of the Min system creates surface waves *in vitro*⁹⁵, with specific wavelength that depends on the relative concentrations of the participating components. In the living wild-type cells, this behavior is translated into pole-to-pole oscillations of these proteins that occurs on a timescale of ~40 seconds/oscillation^{43,46,48,96,97}. When averaged over time, the concentration of MinC in the cell, forms a nonlinear gradient whose minimum is at mid-cell and its maximum is at the poles (Figure 38). This is what allows the FtsZ to bind and form the septal ring at mid-cell.

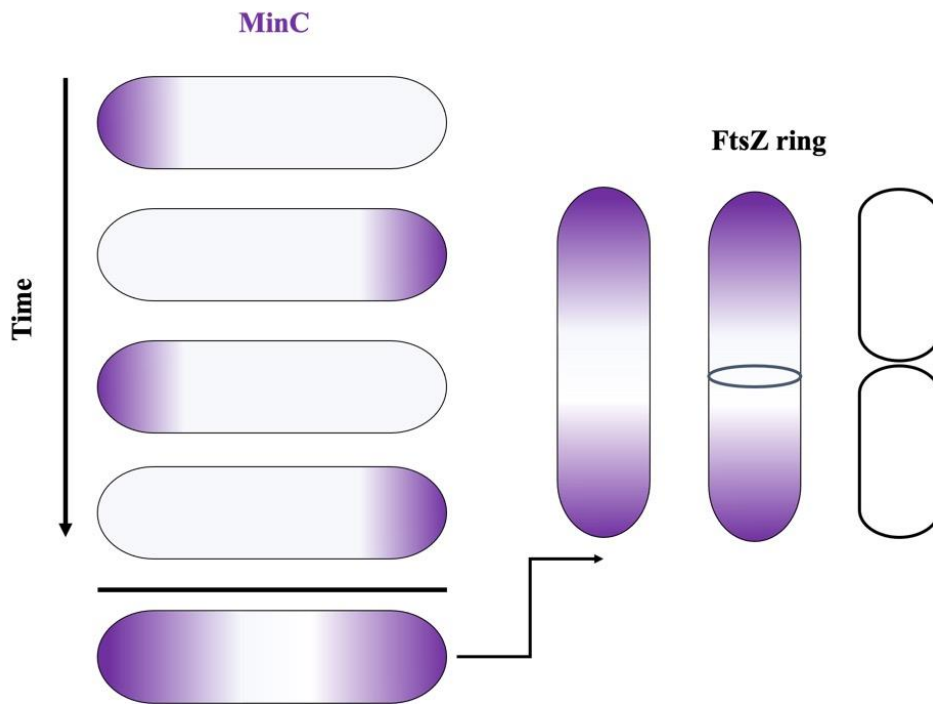


Figure 38 Time averaged concentration of MinC in growing *E. coli* cells. The concentration of MinC forms a non linear gradient in in the cells with a minima at the mid plane that allows FtsZ to form the division ring. Picture adapted from Beatrice *et al* (2019)⁴⁸.

Together, these results both, in vitro and in vivo, emphasize that the oscillations of the Min proteins have an intrinsic wavelength that depends on factors like protein concentration, reaction rates and geometry^{47,49,50,98}. In addition, these oscillations have been also shown to affect the timing of cell division in *E. coli*⁹⁹. Thus, in addition to the need for the FtsZ accumulation to a threshold number, the role of the Min proteins in placing the FtsZ ring can influence cell growth time and thus the cell volume added during the cell cycle.

In order to probe the role of the Min oscillation in cell-size control, we varied parameters known to affect the oscillation's wavelength and observed the effects on cell size. We found that changing the relative concentrations of Min proteins results in a change in the steady state size of the bacterial cell. Our analyses at the single-cell level reveal that the altered ratio of Min proteins, specifically increasing MinE/MinD, delays the FtsZ ring formation until the cell reaches a size that stabilizes the Min system oscillation under the new conditions. These results demonstrate the crucial role of the Min proteins oscillations in determining cell size in *E. coli*.

4.1 Materials and methods

4.1.1 Population level measurements of MinE/MinD effect on cell size

MG1655 bacteria were transformed with plasmids expressing MinE or MinD fused with mEos protein under the control of an arabinose inducible promoter (see Supplementary methods for details). Cells were grown overnight in LB supplemented with the appropriate antibiotics, at 32°C while shaking at 240 rpm. The following morning, the culture was diluted 400-fold in the same medium and regrown for 1 hour. The culture was then induced with arabinose and regrown

at the same conditions for additional 1.5 hours. Six different concentrations of arabinose were used to induce different levels of *minE-mEos* or *mEos-minD* expression in the cells. Following the 1.5 hour of induction, samples were taken and images of the cells were acquired using a Z1 inverted Zeiss microscope in phase contrast mode with a 100x objective in order to measure the cell lengths.

4.1.2 Single-cell experiments in mother machine

MG1655 bacterial strain containing the fluorescent protein, mVenus, integrated within the *ftsZ* gene¹⁰⁰ was transformed with pZA3R-mcherry plasmid. Next, this strain was transformed with plasmids expressing MinE or MinD fused with mEos¹⁰¹ protein under the control of an arabinose inducible promoter. The culture was grown overnight at 32°C in LB with the appropriate antibiotics in an incubator with constant shaking at 240 rpm. The following morning the culture was diluted (1:400) in the same medium and grown until the culture reached an optical density (OD_{600nm}) ~ 0.1. Six ml of the culture was then collected into four 1.5 ml Eppendorf tubes and centrifuged at 3500 rpm for 6 minutes. The supernatant was discarded, and concentrated cells were resuspended in 50 μ l of fresh LB. Next, the cells were loaded into the mother machine and left to grow for 5 hours without induction. Fresh LB medium was streamed through the device at a constant rate of 1ml/hr to supply nutrients to trapped cells and wash excess cells from the device. After 5 hours of growth in normal conditions, the streamed LB medium was supplemented with 0.0025% arabinose to induce expression of *minE-mEos* in the trapped cells. The resulting dynamics of cell-size change was then followed and mapped as we describe later in the results section below.

4.1.3 Real time RTPCR

Bacteria were grown and induced with different levels of inducer concentration as described previously in section 4.1.1. The cultures OD_{600nm} was measured at different time points and 1 ml of each culture was taken from each sample at an OD_{600nm} ~0.3. The samples were then mixed with 2x RNA protect bacteria reagent (QIAGEN) and incubated for 5 min. at room temperature. The mixture was centrifuged at 10,000 rpm. for 10 min. and the supernatant was discarded. The pelleted bacteria were then stored at -80°C until the next day.

The following day, the RNA content of the cells was extracted using the RNeasy mini kit (QIAGEN), by carefully following the extraction protocol provided by the kit manufacturer. The extracted RNA was then used to estimate the ratio of MinE and MinD mRNA at different inducer concentrations using the one-step QuantiTect SYBR green RT-PCR kit (QIAGEN).

The following primers were used to amplify the target sequences of minE and minD mRNAs:

minE_s: CGGCTGCAGATTATTGTTGC

minE_as: TGCTCAAGCTGTACGGTTAC

minD_s: GGTTTGGCCCAGAAGGGAA

minD_as: TTAGCGTTGCATCGCCCTG

The PCR program used for quantifying the mRNA of both targets was:

30 minutes: 50°C (Incubation step to allow cDNA production)

15 minutes: 95°C (incubation to activate taq polymerase)

15 seconds: 94°C	} 45 cycles
30 seconds: 58°C	
30 seconds: 72°C	

Hold: 4 °C

During the PCR process, the amount of amplified DNA of each target sequence was measured by fluorescence at the end of each amplification cycle. The ratio of mRNAs of MinE to MinD was calculated following these steps:

The equation for exponential amplification of PCR can be described simply by:

$$X_n = X_0(1 + E_x)^n$$

Here

X_n = number of target molecules at cycle n

X_0 = initial number of target molecules

E_x = Efficiency of Amplification

n = cycle number at which threshold is reached

Assuming, that amplification efficiency $E_x = 1$, we get $X_n = X_0(2)^n$

For calculating the ratio of mRNAs of the two target genes of interest A and B, we take the number of target molecules to be reached by both genes to be X_T and assume that gene A and B reach the number of target molecules in n_A and n_B cycles respectively. Then:

$$X_T = X_{0,A}(2)^{n_A}$$

$$X_T = X_{0,B}(2)^{n_B}$$

Here, $X_{0,A}$ and $X_{0,B}$ are the initial numbers of molecules in each of the samples.

Equating both equations, gives:

$$X_{0,A}(2)^{n_A} = X_{0,B}(2)^{n_B}$$

And therefore:

$$ratio = \frac{X_{0,A}}{X_{0,B}} = 2^{n_B - n_A}$$

4.1.4 Image acquisition and data analysis

For single cell analysis, cells growing in the microfluidic device (mother machine) were imaged every 1 min in DIC and fluorescence modes using a Hamamatsu ORCA-flash 4.0 camera, mounted on a Nikon Eclipse Ti2 inverted microscope with a 100X objective at 32°C, maintained using the microscope incubator (okolab, H201-1-T-UNIT-BL). Cell length was measured using cell analysis software Oufiti⁶³. Custom MATLAB (MathWorks) programs were developed to analyze acquired data and calculate average statistics.

4.1.5 Z ring intensity measurement

Intensity of the FtsZ ring at the division septum of the cell was estimated by measuring the mean fluorescence intensity inside a $1\ \mu\text{m} \times 1\ \mu\text{m}$ box at the center of the growing cells using image analysis software ImageJ (Figure 39). The mean intensity was corrected by subtracting the mean background illumination from all the images.

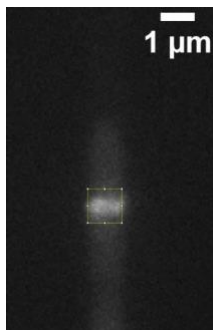


Figure 39 Estimation FtsZ ring intensity in growing *E. coli* cell. Intensity of the z ring was estimated by measuring the mean fluorescence intensity inside the $1\ \mu\text{m}$ square around the mid plane.

4.2 Overexpression of Min proteins and their effect on cell size

The driving hypothesis motivating this section of the research is that for a successful cell division to take place, two conditions must be satisfied. First, the membrane should be free of MinC long enough to allow FtsZ binding to the membrane and initiating the septal ring formation. Second, the FtsZ amount should reach a specific threshold in order to complete the septal ring. The second condition is based on the understanding that the bacterial cell width remains fixed at all times during the cell cycle. Hence, the amount of FtsZ is titrated against the cell perimeter which remains constant for cells of all sizes. This was confirmed through experiments, which demonstrated that FtsZ must reach a fixed threshold amount for a cell to divide successfully, and that reducing the amount of FtsZ or increasing its degradation rate delayed cell division^{35,42,102}.

The first condition on the other hand has never been tested in relation to cell size control. Existing models that describe the Min proteins oscillation suggest that their role is to locate the mid-cell to ensure symmetric division of the cell. However, in order for the FtsZ proteins to bind to the cell membrane at mid-cell, the Min proteins oscillation should be stable, such that the MinC temporal average would exhibit minimum at that location. To achieve this, the relative concentrations of MinC, MinD and MinE should coalesce to produce a stable oscillation and allow the FtsZ binding to the membrane at the right time and location. Thus, the observed natural cell size is that which allows the existing concentrations of Min proteins in the cell to produce stable oscillations. Altering the concentration of one of these proteins would then destabilize the oscillation at that cell size, which will prevent FtsZ binding to the membrane and therefore the cell division would be delayed until the cell reaches a new length that would stabilize the Min oscillation with the new concentrations.

We performed numerical simulations of the Min system oscillation in cells of different lengths similar to the simulations described in previous studies^{44,103}. Typical average profiles of the MinCD concentration along the cell membrane are presented in Figure 40B.

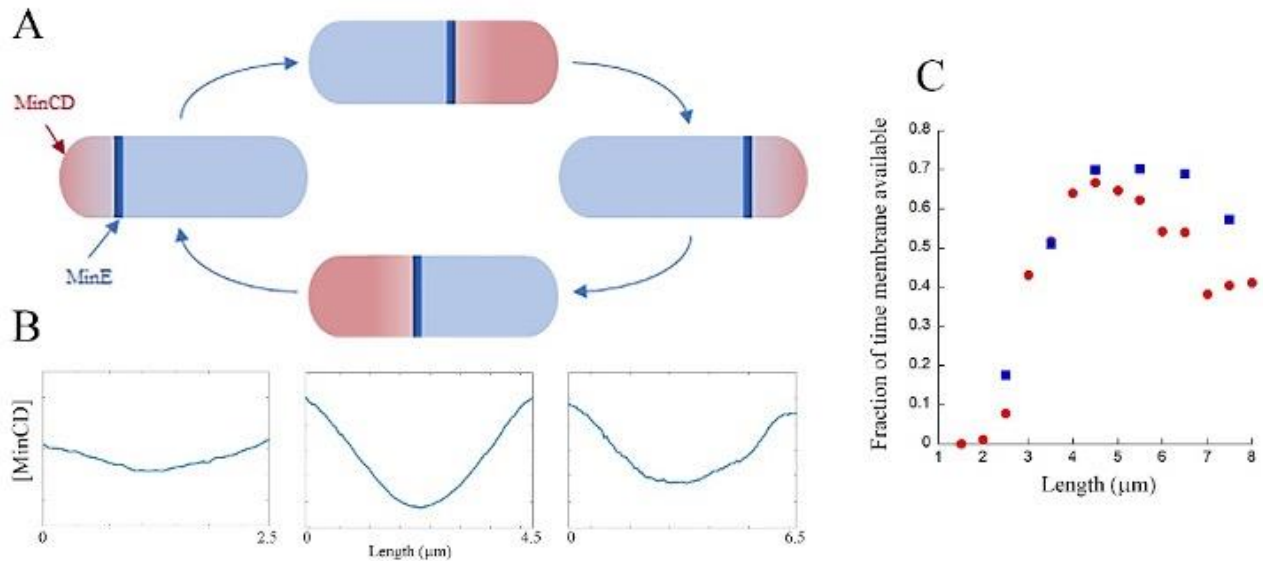


Figure 40 The Min system oscillation. MinCD proteins covers the cell pole and is removed by MinE, which causes them to move to the other pole and spread towards the center until the MinE ring catches up with them again. (B) the temporal average of the MinCD concentration along the cell exhibits a minimum at the middle of the cell. However, this minimum is more pronounced for the optimal cell length. (C) the fraction of time during which the middle of the cell is free of MinCD as a function of cell length. The red circles depict the results of simulations using conditions identical to those used in Huang *et al.*⁴⁴, while the blue squares represent the results of simulations with half of the concentration of MinCD and MinE used in Huang *et al.*⁴⁴.

It is clear from these profiles that there is an optimal cell length, for which the mid-cell has minimal average concentration of MinCD. This can be also seen by calculating the fraction of time during which that location is free of MinCD. The longer that location is free of MinCD, the higher

the probability for the FtsZ protein to initiate the septum formation at that location. Our simulations results show that the time during which that site is available for FtsZ binding is maximized for a specific cell length (Figure 40C). Moreover, this length in which the available time is maximized changes with the concentration of the Min proteins in the cell.

In order to test our hypothesis experimentally, we changed the relative concentration of two key proteins involved in this oscillation. We overexpressed either MinE or MinD in the cells and monitored how the population average cell size changes in response. This was achieved by transforming our cells with plasmids containing arabinose inducible promoter controlling the expression of one of the two genes, *minE-mEos* or *mEos-minD*, which produce MinE or MinD protein fused with the fluorescent protein mEos. Using these constructs, we were able to control the level of over expression of MinE or MinD by inducing the promoter with different arabinose concentrations. In addition, the fluorescence intensity of mEos, enabled us to quantitatively determine the over-expression level of these proteins.

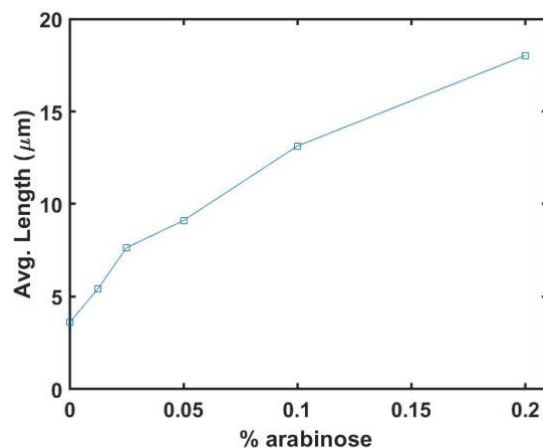


Figure 41 Average population size of cells overexpressing MinD. Average population size increases almost linearly with inducer concentration.

We have induced the expression of MinE and MinD at six different levels as described in details in the Materials and methods section. Images of the cells grown with the various expression levels were acquired and the population's average cell size for cells overexpressing MinD (Figure 41) or MinE (Figure 42) was calculated.

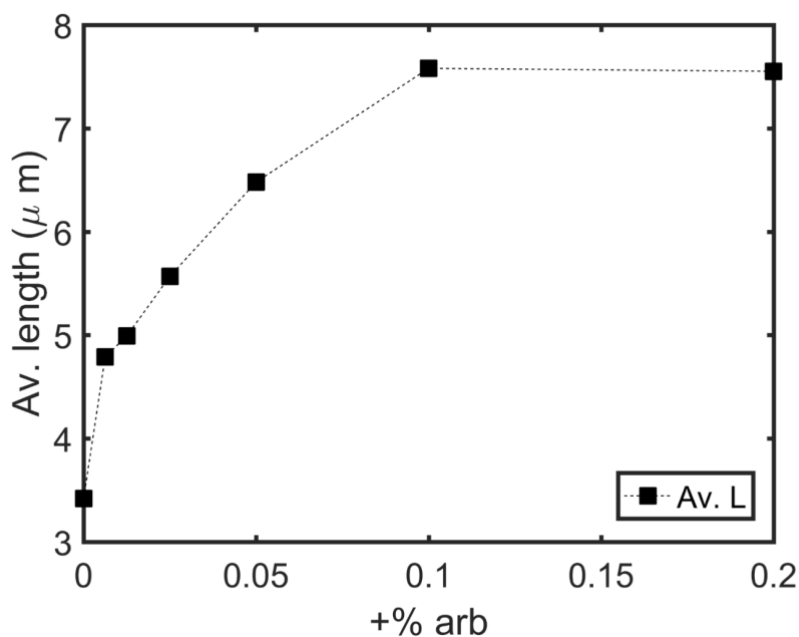


Figure 42 Average population size of cells overexpressing MinE. Average population size increases with inducer concentration before getting saturated to a fixed value.

Our results show that overexpressing MinD or MinE resulted in an increase in the population's average cell size. Cells overexpressing MinD showed a continued increase in average cell size while those over expressing MinE showed a more controlled behavior and saturated to a new size at high inducer concentration. In the case of overexpressing MinD, in addition to

becoming uncontrollably long, MinD appeared to occupy most of the cellular membrane and attached to the cell membrane in random patches (Figure 43). This provides an insight to why cells were growing uncontrollably long at high inducer concentration. MinD is known to recruit MinC and prevent the FtsZ binding to the membrane and the thus cell division. Note as well, that it has also been suggested that proper recruitment of MinD and its organization onto the membrane requires MinE¹⁰⁴. Hence, the presence of MinD in excess amount, while MinE is maintained at its natural concentration, would lead to disordered accumulation of MinD on the cell membrane and hinder the Min oscillations and therefore cell division.

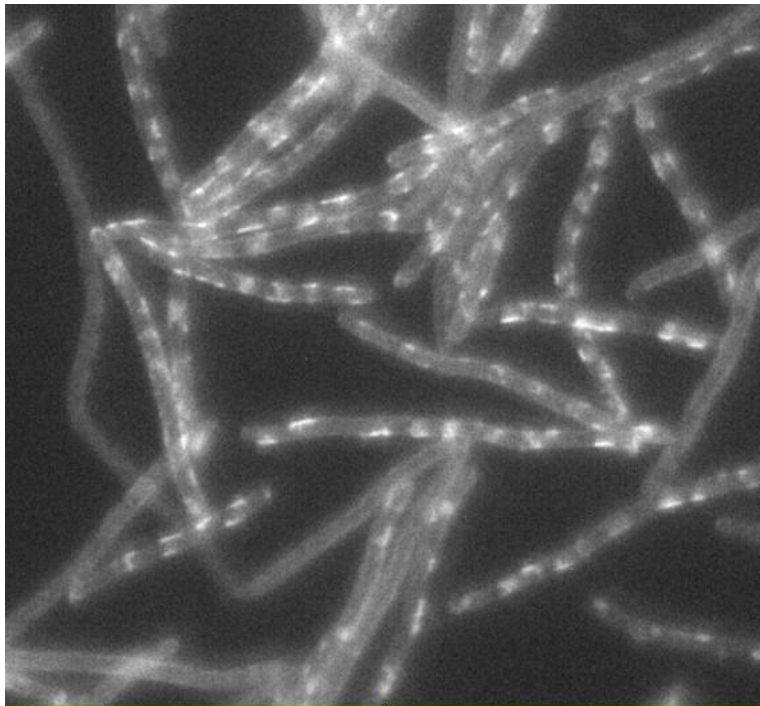


Figure 43 Fluorescence image of cells over expressing MinD. Cells over expressing MinD at 0.2% arabinose show irregular attachment pattern.

To quantify the level of over-expression of MinD and MinE, we measured the mean fluorescence intensity of mEos in the cells. While cells over-expressing mEos-MinD showed an almost linear increase in mEos mean fluorescence intensity similar to cell size (Figure 44), cells overexpressing MinE-mEos on the other hand showed a constant mean fluorescence at the different inducer concentrations (Figure 45).

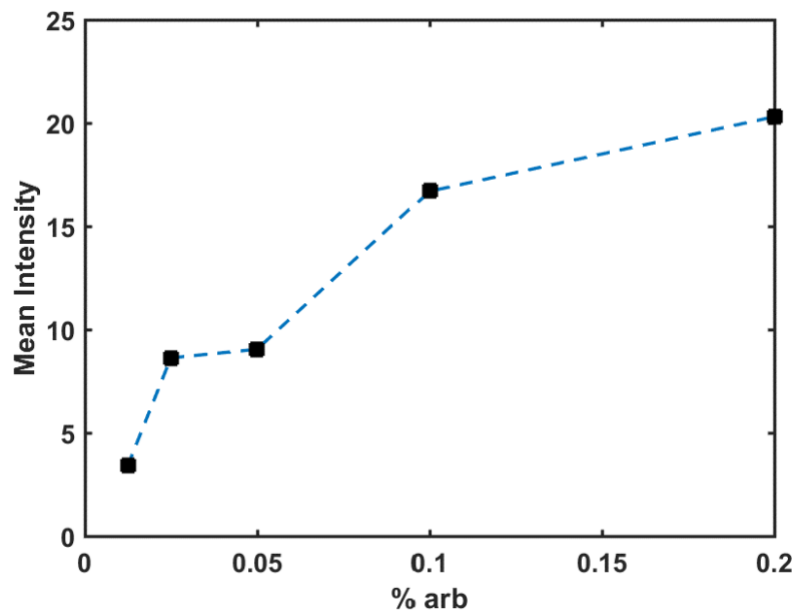


Figure 44 Mean fluorescence intensity of cells over expressing MinD. Similar to cell size, cells over expressing MinD show increase in mean fluorescence intensity with increase in inducer concentration.

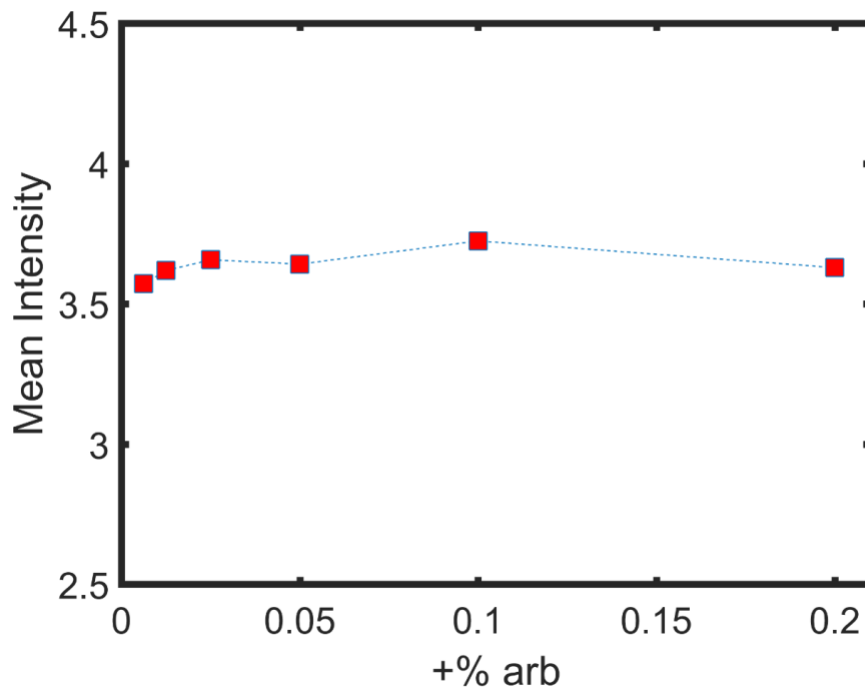


Figure 45 Mean fluorescence intensity of cells over expressing MinE. Cells over expressing MinE show constant mean fluorescence intensity at all inducer concentrations.

These observations led us to further investigate the cells overexpressing MinE. We analyzed individual cell cycles of cells over expressing MinE to see if we can observe an increase in the fluorescence, but even individual cells did not show any difference in fluorescence intensity during their cell cycle (Figure 46 and Figure 47).

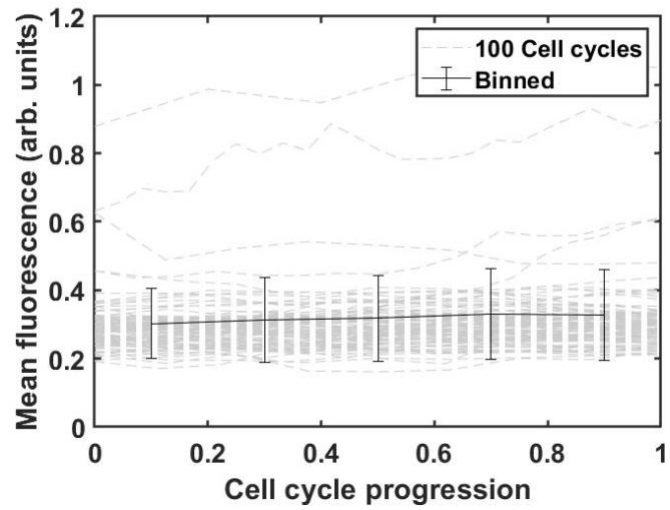


Figure 46 Mean fluorescence intensity of MinE overexpressing cells during cell cycle. Average fluorescence intensity does not change during cell cycle for cell overexpressing MinE at 0.1 percent arabinose concentration.

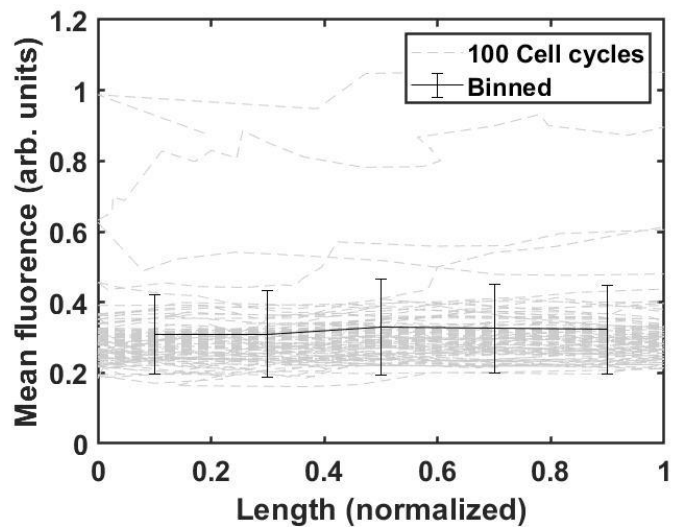


Figure 47 Mean fluorescence intensity of MinE overexpressing cells as a function of size. Same data as Figure 46 but as a function of length.

The results described above suggest that either cells are trying to compensate for the increased production of MinE by increasing their size or the fluorescence signal is too weak to show a significant increase in intensity with the increasing inducer concentration.

To confirm that our induction is leading to increase in MinE protein in the cells, we measured the expression level of MinE relative to that of MinD at the mRNA level using quantitative real time PCR (RT-PCR) as detailed in Materials and methods. The mRNA was extracted from 4 cultures, each of which was induced with a different arabinose concentration to overexpress MinE-mEos at different levels, similar to the population size measurements.

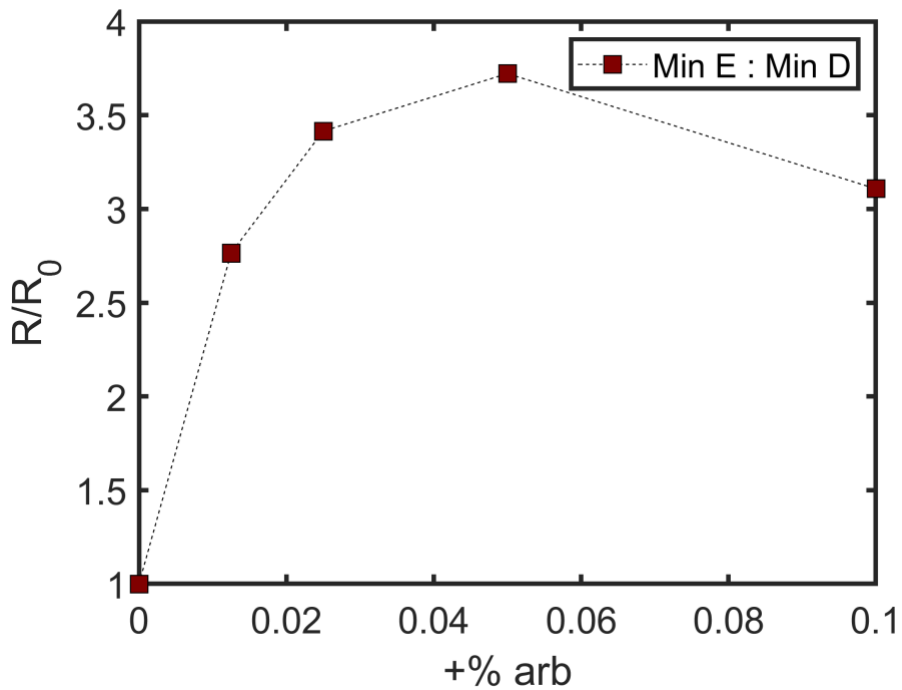


Figure 48 Ratio(R) of MinE to MinD in cells overexpressing MinE relative to the ratio (R_0) in WT cells. Ratio of MinE to MinD calculated using real time RTPCR shows increase in MinE amount relative to MinD with increasing inducer concentration.

Our results confirmed that the ratio of MinE to MinD expression level increases with the increase in inducer concentration (Figure 48). Plotting the average population size as a function of the ratio MinE/MinD (Figure 49) confirmed that the increase in the ratio MinE/MinD increases the population's average cell size.

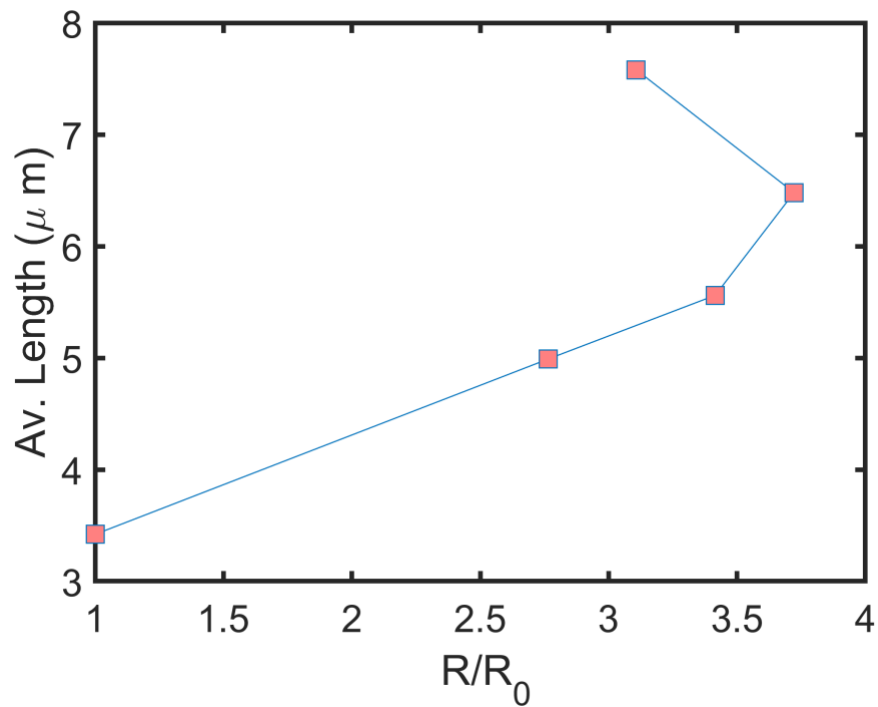


Figure 49 Average cell length as a function of ratio of Min proteins. Average cell size of the population increases with increase in ratio of MinE to MinD in cells.

4.3 Single cell experiments

The results presented in the previous section clearly demonstrate that altering the balance between the Min proteins will cause a shift in the steady state cell size. However, FtsZ has been shown to bind to the membrane early during the cell cycle, within the first quarter of the cell cycle depending on the growth conditions¹⁰⁵⁻¹⁰⁷. The role of the Min oscillation in locating the FtsZ ring should then take place early in the cell cycle, and the oscillation has to be stable soon after a new cell is born. Thus, when the concentration balance of the Min proteins is disturbed, it is expected that the FtsZ binding will be delayed until the cell reaches a size that would stabilize the Min oscillation with the new concentrations. As a result, the cell will also grow to a larger size before it divides again and when it divides it will create two daughter cells, whose birth sizes are larger than the birth size of their mother. In these new larger cells, the Min oscillation should be stable earlier than in the previous cell cycle, and therefore, the FtsZ ring formation will start earlier as well.

The hypothesis detailed above, implies that once the Min proteins reach their final stable concentrations following an induction of over-expression of one of the proteins, as we did in the previous section, the FtsZ ring formation should initiate as early as it did before the induction with the initial concentrations of the Min proteins. In other words, the increase in the birth size of new daughter cells should increase gradually upon inducing the over-expression of one of the Min proteins until it reaches the new steady state cell size. On the other hand, the delay in the FtsZ ring formation should be transient and once the new steady state is achieved it should be exactly the same as before the induction.

To test this hypothesis, we used the microfluidic device, the “mother machine”, to follow size and FtsZ ring formation dynamics simultaneously in single cells while inducing *minE-mEos*

over-expression. Initially, wt MG1655 cells expressing FtsZ-mVenus and carrying the plasmids expressing MinE fused with mEos¹⁰¹ protein, under the control of an arabinose inducible promoter, were loaded into the microfluidic device and grown without inducing the expression of *minE-mEos*. After several hours of growth without induction, the expression of *minE-mEos* was induced by adding arabinose to the feeding solution to a final concentration of 0.0025% w/v (see Materials and methods for further details).

Measurements of the birth size (L_0) of newly born cells after each division reveal as expected, that immediately following the induction of *minE-mEos* expression, cells become longer and their cell cycle duration is extended. Figure 50 shows an example trace of a cell size dynamics during the induction experiment.

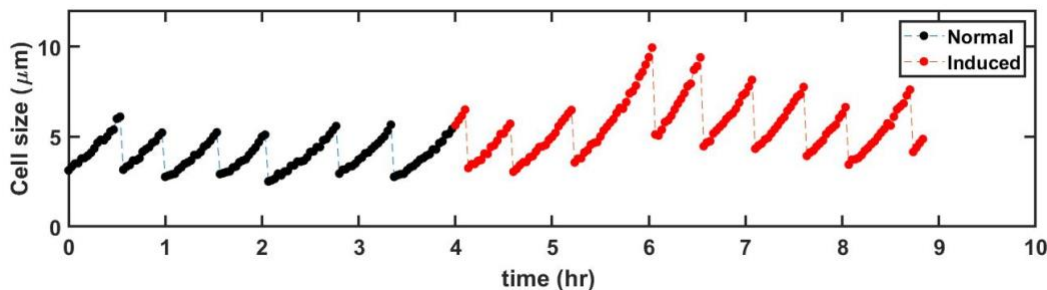


Figure 50 Example trace of cell size during single cell experiment. After induction cell starts to elongate and then successively divide at a size larger than normal.

The cell length following the induction of *minE-mEos* expression, continued to increase gradually until a new steady state cell-length was reached ~5 generation later (Figure 51). This result demonstrates that the new ratio of [MinE]:[MinD] set by the overexpression of *minE-mEos*

leads to a new stable birth size that is longer than the average birth size of the cells observed under normal conditions (Figure 51). It also confirms our above hypothesis regarding the cell size dynamics in response to altering the balance of the Min proteins.

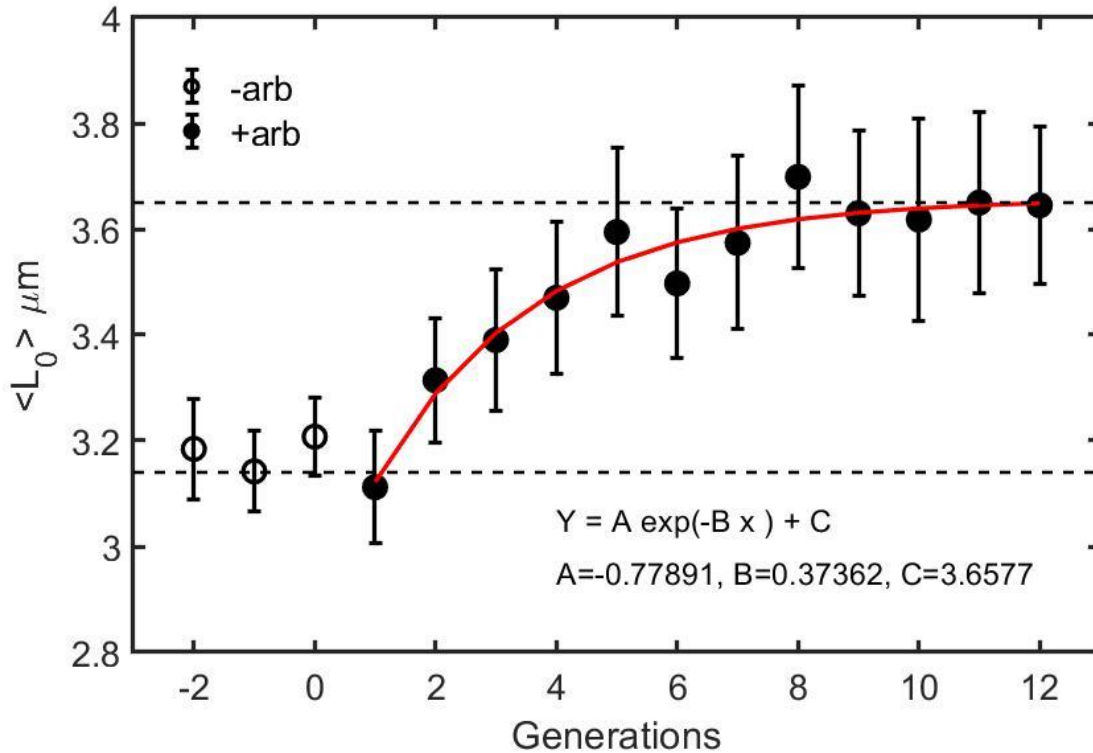


Figure 51 Average cell size as a function of generations with overexpression of MinE. Cell size increases gradually and saturates to new stable size following an overexpression of MinE protein. Here, average is calculated over 37 traces and error bars represent standard error of the mean calculated by bootstrapping the data by randomly choosing 20 traces with replacements for 100 runs.

To investigate the mechanism, through which this increase in protein ratio is changing the cell size, we probed the FtsZ ring formation dynamics during the cell size increase following *minE*-

mEos induction. As mentioned previously, this was achieved using a bacterial strain containing the fluorescent protein, mVenus, integrated within the *ftsZ* gene¹⁰⁰. This integration produces a functional fluorescent FtsZ protein, and this strain has been used previously to visualize the z ring dynamics and does not impair bacterial cell division³⁶ (see Figure 52).

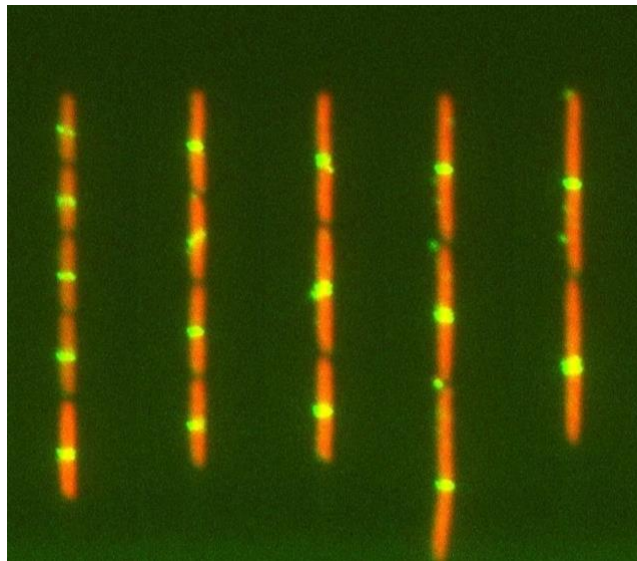


Figure 52 Snapshot of a growth channel at different time points in an experiment. FtsZ ring is visualized using a strain that has mVenus protein integrated in an internal site of *ftsZ* gene.

Using the above-described strain, we measured the fluorescence intensity of the FtsZ ring in cells dividing under normal conditions and in cells elongating following *minE-mEos* induction. On a closer look at the cell cycle, we observed that in cells exhibiting normal division before induction, FtsZ ring formation proceeds as expected soon after cell division and reaches 60% of its maximal intensity within the first quarter of the cell cycle. On the other hand, following *minE-mEos* induction multiple events of ring formation and dissolution were observed before a stable

division septal ring was formed. Furthermore, the 60% of maximal intensity was reached only towards the last one third of the cell cycle (Figure 53). This demonstrates that increase in the ratio of MinE:MinD alter the normal FtsZ ring dynamics in cells elongating after induction. Note that in elongating cells there is enough FtsZ to form the ring, but the cells don't meet the second requirement of stable oscillations to form the ring. This clearly confirms that FtsZ threshold buildup is not sufficient for cell division as suggested by previous studies.

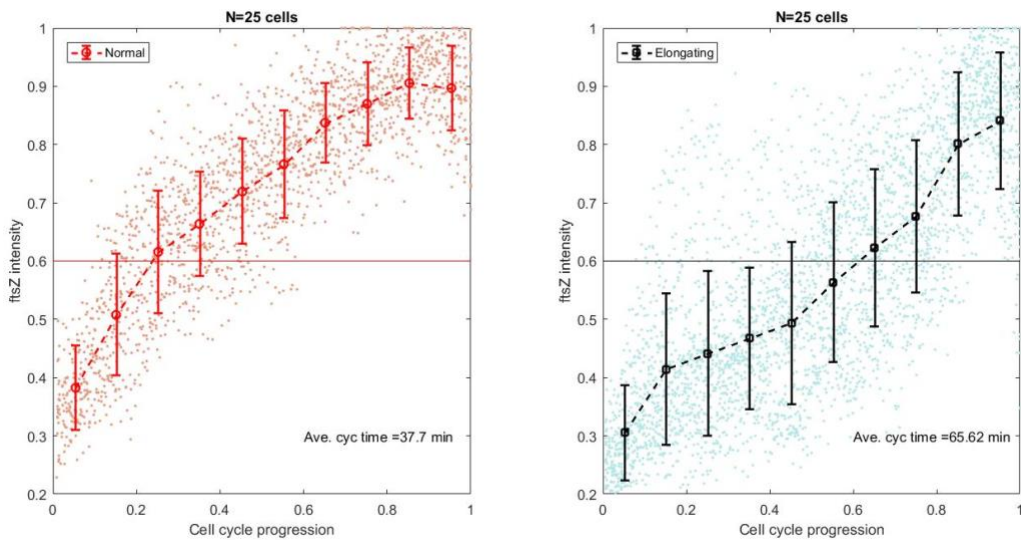


Figure 53 FtsZ ring intensity during cell cycle. FtsZ ring intensity in cells growing under normal conditions reached 60 percent of the maximum in first quarter of the cell cycle while after induction intensity of the FtsZ ring in elongating cells reached 60% of maximum intensity in last quarter of their cell cycles. This shows that binding of FtsZ is significantly delayed by overexpression of MinE protein.

In order to see how the FtsZ ring dynamics correlates with our previous observation of the cell size, we probed the ring dynamics in the cell lineages before and after inducing *minE-mEos*

overexpression. We measured the time required for the fluorescent FtsZ ring to reach 65 % of its maximal intensity (examples are presented in Figure 54). Consistent with our proposed theory we observed that the time to form a stable FtsZ ring is initially delayed in cells overexpressing the MinE protein. However, within ~4 generations after the induction the stable ring formation time decreases back to its initial value observed prior to induction (Figure 55).

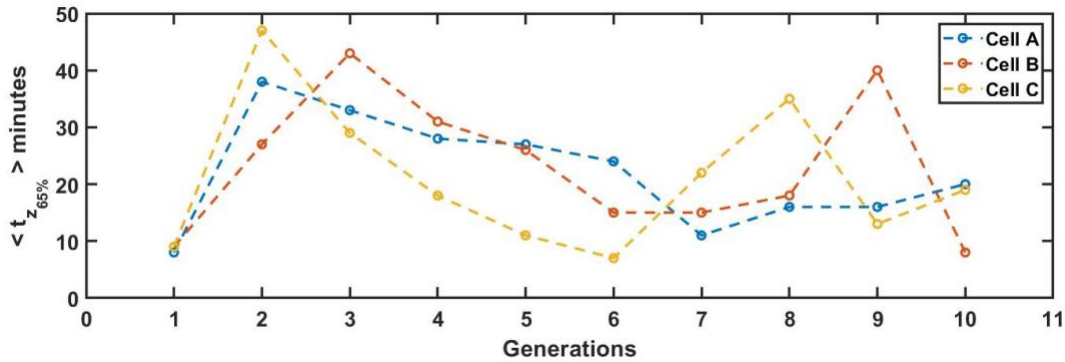


Figure 54 Stable Z ring timing traces as a function of generations after induction. Time to reach 65% of maximal intensity of FtsZ ring in three cells following overexpression of MinE protein increases transiently before coming back to normal levels.

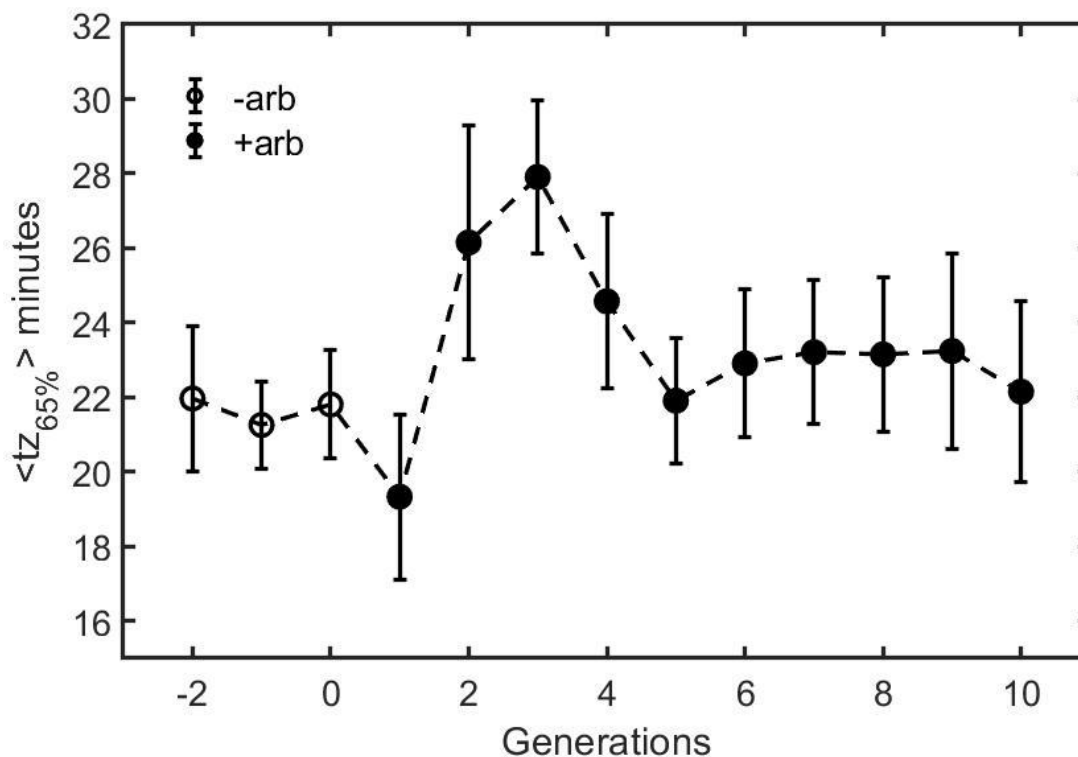


Figure 55 Average stable Z ring timing as a function of generations. Time to reach 65% of maximal FtsZ ring intensity increases transiently following an overexpression of MinE proteins before coming back to normal levels. Here, average is calculated over 37 traces and error bars represent standard error of the mean calculated by bootstrapping the data by randomly choosing 20 traces with replacements for 100 runs.

4.4 Conclusions

The main aim of this section of the study was to explore the role of Min proteins dynamics in determining cell size in bacteria. We showed that increasing the ratio of MinE to MinD proteins results in an increase in the average cell size of *E. coli* at the population level. We performed single cell experiments, in which we increased the expression of MinE proteins relative to MinD proteins in order to understand the mechanism behind the observed increase in cell size. We found that

disturbing the balance of the Min proteins delays the binding of FtsZ proteins to the membrane until the cell reaches a size that stabilizes the Min oscillation with the new concentrations. As a result, the cell grows to a larger size before it divides and produces two daughter cells whose birth sizes are larger than the birth size of the mother. This increase in the birth size of the daughter cells continues until the Min proteins reach their final stable concentration following an induction of over-expression of MinE protein. On the other hand, the delay in the FtsZ ring formation is transient and disappears once the cells reach the new steady state cell size. These results give new insights into cell-size control and dynamics in bacteria and demand further exploration of the role of Min proteins in size homeostasis and variability within a population.

5.0 Discussions and conclusions

In order to proliferate, cells transfer information in the form of DNA and non-genetic material to future generations. Transmission of this information or informational resources from one generation to the next is carried out through genetic and epigenetic inheritance mechanisms. It was a general view for a long time that only the genetic material is informational while other inherited non-genetic components just play a supporting role of decoding this genetic information. Epigenetic or non-genetic inheritance is the process of transmission of various non-genetic materials like proteins, gene transcription level, cell structures, chromatin markings (like DNA methylation and histone modifications), small RNA molecules etc.. Variations in this information and its transfer to future generations are induced either due to environmental fluctuations or as a result of biochemical noise during cell growth. Contrary to the old general view, however, more recent studies have highlighted the non-genetic component's "active" role in forming the observed cellular properties and preserving them over time through inheritance between successive generations, rather than just playing a "passive" role of decoding the information structured in the DNA. Therefore, understanding the contribution of these epigenetic factors to cellular properties and their evolution over time is of paramount importance for understanding the evolution of cellular properties and functions, and for constructing theoretical models able to predict future states of living organisms. In this research, we developed a quantitative approach to study the dynamics of non-genetic inheritance in bacteria in order to understand its role in shaping the cell's properties and restraining their variability over time.

In Chapter 2, we described the fabrication process of a new microfluidic device that provides high quality single cell data of cell growth and division dynamics in sister cells growing

in same environment. This new microfluidic device can differentiate between cellular and environmental effects on cellular properties. This new technique provides high throughput single cell data that allows for quantitative measurement of non-genetic memory in bacteria and reveals its contribution to restraining the variability of cellular properties. This device allows trapping of bacterial cells from birth to death and can also be used to study the process of aging in bacteria more effectively. In Chapter 3, we utilize this new technique to measure the non-genetic memory of bacterial cells for several different traits. Our results reveal important features of cellular memory. We find that different traits of the cell exhibit different memory patterns with distinct timescales. While the cell cycle time (Figure 22) and cell size (Figure 24) exhibit slow exponential decay of their memory that extends over several generations, other cellular features exhibit complex memory dynamics over time. The growth rates of two sister cells, for example, diverge immediately after division, but re-converge towards the end of the first cell cycle and subsequently persist together for several generations (Figure 30). In comparison, the mean fluorescence intensities, reporting gene expression, are identical in both cells immediately after they separate but diverge within two cell cycles (Figure 32). Our results show that the restraining force dynamics vary significantly among different cellular properties, and its effects can extend up to ~10 generations. In addition, the growth rate variation emphasizes the effect of division asymmetry, which can help in understanding the mechanism that controls cellular growth rate. The slow increase in the growth rate variance that follows, reflects the effect of inheritance. Since both cells inherit similar content, which ultimately determines the rate of all biochemical activities in the cell and thus its growth rate, it is expected that both cells would exhibit similar growth rates once they make up for the uneven partitioning of size acquired during division. The short memory we see in the protein concentration on the other hand, suggests that cells are less restrictive of their protein

concentration. This might be protein specific, or for proteins that are expressed from plasmids only. Nevertheless, these results highlight the importance of such studies, and how this new method can help answer fundamental questions about non-genetic memory and variability in cellular properties. These measurements will allow us to understand how non-genetic variability is created and maintained in an isogenic cell population and identify the cellular components responsible for controlling the different traits we observe.

Furthermore, in order to understand and characterize the evolution of population growth rate as it reflects its fitness, there is a need to incorporate inheritance effects, which has been thus far assumed to be short lived. This study confirms that cellular memory can persist for several generations, and therefore limits the variation in certain cellular characteristics, including growth rate. Such memory should be considered in future studies and has the potential of changing our perception of population growth and fitness.

We also performed experiments to test the robustness of non-genetic inheritance in face of environmental challenges and demonstrated that the correlation strength of cellular properties in sister cells remain the same at different temperatures and in different growth media (Figure 23). The cell cycle duration and biochemical activity are highly sensitive to temperature and nutrient conditions but this does not seem to affect the strength of correlations between sister cells' properties. This shows that the nongenetic inheritance dynamics is extremely robust, and that decorrelating noise that erases bacterial memory is mostly contributed by division events. However, when the cells are challenged with unforeseen stressful conditions, the decorrelation between cellular properties in sister cells is expedited. In order to challenge the cells with a new stressful condition, we subjected our cells to different levels of antibiotic concentrations. Here, we found that the strength of correlation between sister cells properties decayed in a dose dependent

manner. It will be interesting to further explore the exact mechanism that makes this correlation weaker in the presence of stress. A possible explanation is that cellular gene expression profile is randomized in the presence of stress and this randomization leads to loss of correlation between sister cells. The search for the exact mechanism is desired but is out of the scope the current work.

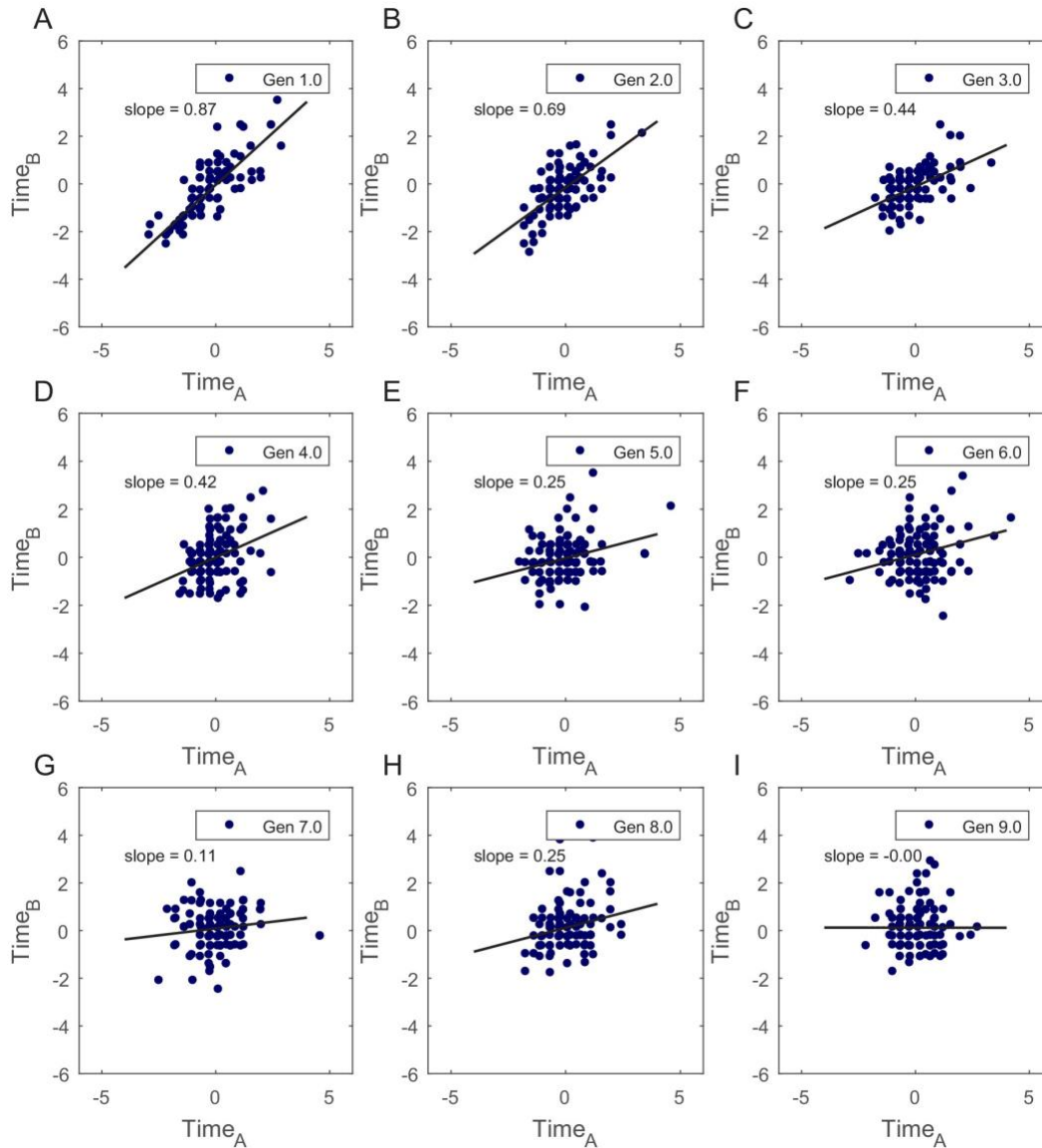
One of the important contributions of this study is to demonstrate that using our novel setup, we were able to separate the contribution of cellular factors to cellular memory from environmental ones. Nevertheless, more research is still needed in order to identify and quantify the sources of variability within the cellular factors. Our new device will allow us to achieve this goal in the near future.

In Chapter 4, we showed that the Min proteins play an important role in determining the steady state bacterial cell size. We demonstrated that changing the ratio of Min proteins affects the timing of the FtsZ ring formation in the bacterial cell. This delay in the stabilization of the ring allows for extra cell growth that results in change in cell size at division. Our results demonstrate that cell division is a complex process and involves an interplay between various proteins and dynamical processes, and is not determined by a single molecular mechanism such as the accumulation of any one protein to a set threshold. These findings raise an important question about the mechanism of cell-size control and cell-size optimization to the growth environment; Do cells naturally alter the concentrations of the Min proteins to achieve the optimal size in different environments? Further experiments are needed to address this question, in which the ratio of the Min proteins can be measured in cells growing in different conditions and their correlation with cell size could be evaluated.

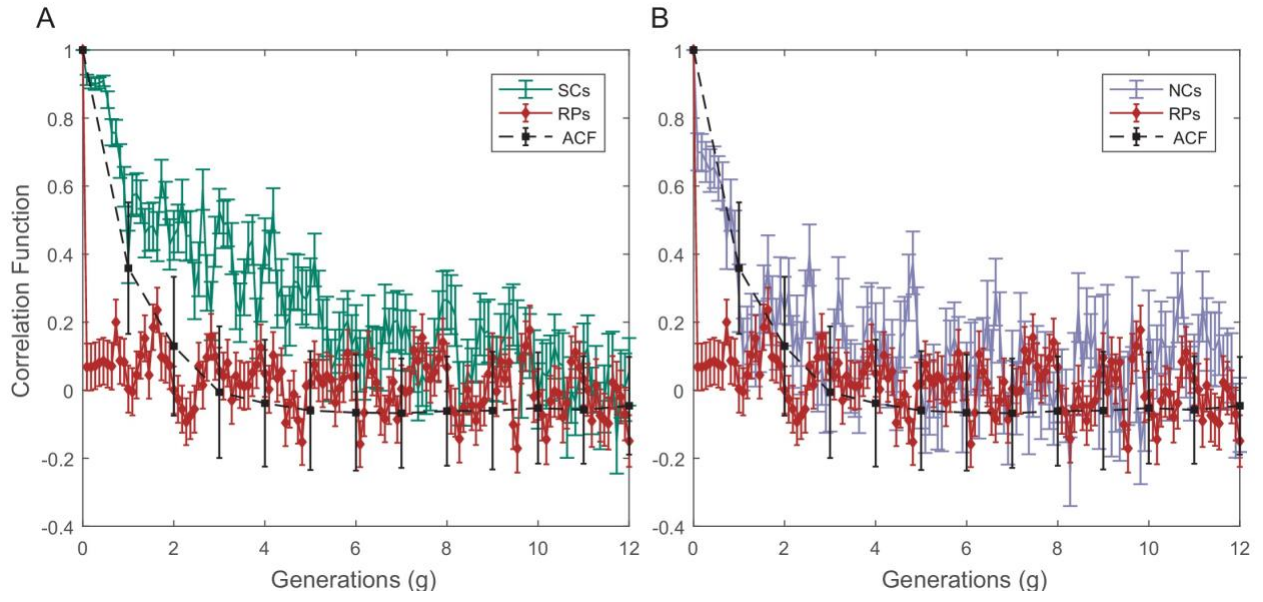
In summary, dynamical processes take place in living organisms at every level of organization, whether it is at the molecular, cellular, or population level. They are fundamental for

achieving order in biological systems, and ensuring that cells are able to fulfill their functional role. Therefore, it is important to study dynamical processes in biology and be able to characterize them quantitatively and understand how they contribute to the observed behavior of the biological system of interest. Here, we demonstrated this by studying two important dynamical processes that occur at vastly different levels of organization. The first occurs at the cellular level. Here, the inheritance dynamics of cellular properties, determined by the cellular content as a whole, was investigated. The second process studied here, was the molecular dynamics that determines a pole-to-pole oscillation used to localize the septal ring in bacteria. Our results summarized above, clearly show the importance of dynamical processes in determining cellular properties, both within a single cell-cycle time and over the duration of several generations. We believe that these results, beyond their contribution to our understanding of the specific phenomena studied here, highlight the importance of studying dynamical processes in biological systems in general.

Appendix A Supplementary figures



Appendix Figure 1 Correlation in cell cycle times (T) for SCs at 32°C was verified by calculating slopes of best fits to the plots of normalized Time_A vs Time_B for the two cells. (A-I) Slopes of the best fit lines for Time_A vs Time_B show that cell cycle times are strongly correlated for first few generations in SCs. This shows existence of non-genetic memory that restrains the divergence of the phenotypes in cells originating from the same mother cell.



Appendix Figure 2 Raw data of PCF of cellsize for SCs, NCs and RPs.

Appendix B Supplementary methods

Appendix B.1 Preparation of electrocompetent cells for transformation

For the purpose of visualization of cells or to modify and/or monitor the expression level of certain proteins in our study, plasmids containing the gene of interest were transferred into the electrocompetent cells prepared by following these steps:

1. Grew the bacterial strain from glycerol stock stored at -80°C in 50 ml LB at 30°C with continuous shaking at 240 rpm overnight.
2. The following morning, re-diluted the overnight culture in 50 ml fresh LB medium to an initial $\text{OD}_{600\text{nm}}$ of ~ 0.05 .
3. Grew the cells for 2 – 3 hours at 37°C until they reach an $\text{OD}_{600\text{nm}}$ of 0.4.
4. Transferred the cells to pre chilled tubes kept on ice.
5. Centrifuged the cells at 4°C for 7 mins at 3000 rpm using a table-top refrigerated centrifuge (Labnet) and discarded the supernatant.
6. Resuspended the cell pellet by adding 10 ml of pre chilled 15% glycerol in H_2O solution.
7. Centrifuged again for 5 minutes at 2500 rpm and discarded the supernatant.
8. Repeated steps 6-7 thrice.
9. Resuspended the cells again by adding 10ml of 15% glycerol solution and left it on ice for 30 minutes.
10. Centrifuged again for 5 minutes at 2500 rpm.
11. Discarded the supernatant and resuspended the cells in 2ml of 15% glycerol solution.
12. Made 100 μl aliquots in 1.5 ml Eppendorf tubes and stored at -80°C .

Appendix B.2 Plasmid extraction

For extracting plasmid DNA, bacterial cells were grown overnight in LB at 30°C while shaking at 240 rpm. Next morning, they were re-diluted in 50 ml fresh LB and grown at 37°C until OD_{600nm} of ~1.0. Extraction was carried out using Plasmid Midi Kit (QIAGEN) by carefully following the extraction protocol supplied with the extraction kit.

Appendix B.3 Transformation of plasmids

Extracted plasmid DNA containing genes of interest was transferred into the different bacterial strains using the process of electroporation. The following steps were carried out for successful transformation:

1. Thawed 100 μ l electrocompetent cells on ice for 10 mins.
2. Added 5 μ l of plasmid DNA(<5ng) to the electrocompetent cells and mixed gently by flicking the Eppendorf tube.
3. Left the mixture on ice for 15 mins.
4. Transferred the Cell-DNA mixture into a prechilled electroporation cuvette.
5. Placed the electroporation cuvette in the MicroPulser (BIO-RAD) and pulsed the bacterial culture in EC2 mode.
6. Added 500 μ l of fresh LB to the cuvette immediately after pulsation and transferred the mixture into a 1.5 mL microcentrifuge tube.
7. Incubated the cells for 1.5 hours at 37°C in a shaking incubator.

8. Following the incubation, centrifuged the cells at 5000 rpm for 5 minutes using a table-top centrifuge (Spectrafuge, Labnet) and discarded the supernatant.
9. Resuspended the pellet in 50 μ l of fresh LB and split the transformed cultured into two aliquots, ~ 45 μ l and ~5 μ l.
10. Plated both the aliquots onto LB agar plates containing the appropriate antibiotic.
11. Incubated the plates overnight at 37°C.
12. The following day, picked an isolated colony to make the glycerol stock to be stored at -80°C.

Appendix C Source codes

```
// 1D code for mind MinE oscillations (Wingreen's equataions)in c++ by Kulveer Singh, Bar-Ilan university, Israel.
```

```
#include <fstream>
#include <iostream>
#include <exception>
#include <cstdio>
#include <cstdlib>
#include <cmath>
#include <time.h>
#include <string>
#include <iomanip>
#include <vector>
#include <complex>
#include <stdbool.h>
#include <random>
#include <chrono>

using namespace std;
#define PI 3.14159265
double dx=0.05;

//to caculate laplacian
double lap(int index, int xSteps, double c0, double c1, double c2)
{
    //computing node is c1
    double cx;

    if(index==1)
    {
        cx=(c2-c1)/(dx*dx);
    }else if(index==xSteps+1)
    {
        cx=(c0-c1)/(dx*dx);
    }else
    {
        cx=(c0-2*c1+c2)/(dx*dx);
    }

    return cx;
}

int main (int argc, char *argv[] )
{

    //input lambda, sigma, omega, time of run
```

```

    if (argc < 4)
    {
        std::cerr << "Usage: " << argv[0] << " L" << " minD_rho" << "
minE_rho" << std::endl;
        return 1;
    }

    //file to store all proteins separately at different times
    ofstream ReadFile;
    char Filename[100];
    sprintf(Filename, "data_L_%f_minD_%f_minE_%f.dat", atof(argv[1]),
atof(argv[2]), atof(argv[3]));
    ReadFile.open(Filename);

    //file to store total minD and minE in entire cell (to check
conservation)
    ofstream ReadFile1;
    char Filename1[100];
    sprintf(Filename1, "total_L_%f_minD_%f_minE_%f.dat", atof(argv[1]),
atof(argv[2]), atof(argv[3]));
    ReadFile1.open(Filename1);

    //file to store protein (total (eg. minD_ADP+minDATP) in bulk and on
surface) at different x
    ofstream ReadFile2;
    char Filename2[100];
    sprintf(Filename2, "data_total_L_%f_minD_%f_minE_%f.dat", atof(argv[1]),
atof(argv[2]), atof(argv[3]));
    ReadFile2.open(Filename2);

    // file to store time average value of proteins at different x
    ofstream ReadFile3;
    char Filename3[100];
    sprintf(Filename3, "data_avg_L_%f_minD_%f_minE_%f.dat", atof(argv[1]),
atof(argv[2]), atof(argv[3]));
    ReadFile3.open(Filename3);

    //parameters. Length is in micrometer, time in sec, conc. = # of
molecule/micrometer
    double sg_D_ADP_ATP, sg_de, sg_D, sg_dD, sg_E, D_D, D_E;
    D_D=2.5;
    D_E=2.5;
    sg_D_ADP_ATP=1.0;
    sg_D=0.025;
    sg_dD=0.0015*10;
    sg_de=0.4;
    sg_E=0.093*10;

    //average concentration of minD, minE in number of molecule per
micrometer
    double ro_D_initial, ro_E_initial;
    ro_D_initial=atof(argv[2]);
    ro_E_initial=atof(argv[3]);

```

```

double D, L, T, dt;
L = atof(argv[1]); //Length of bacteria
T=1000.0; //Time in seconds
dt = 0.0001;//timestep size

int xSteps, tSteps;
xSteps=int(L/dx);//number of lattice points
tSteps=int(T/dt)+1;// Number of timesteps

//array of density at all lattice points
double ro_D_ADPO[xSteps+3], ro_D_ADPl[xSteps+3], ro_E0[xSteps+3],
ro_El[xSteps+3], ro_D_ATPO[xSteps+3], ro_D_ATPl[xSteps+3], ro_d0[xSteps+3],
ro_d1[xSteps+3], ro_de0[xSteps+3], ro_del[xSteps+3];
//double c_x, c_initial=100.0;

//Initializing the concentration at lattice points
for(int j=1; j<=xSteps+1;j++)
{
    ro_D_ADPO[j]=(-j*ro_D_initial*L*2/double((xSteps)*(xSteps+1)) +
ro_D_initial*L*2/double(xSteps));
    ro_E0[j]=(-j*ro_E_initial*L*2/double((xSteps)*(xSteps+1)) +
ro_E_initial*L*2/double(xSteps));

    ro_D_ATPO[j]=0.0;
    ro_d0[j]=0.0;
    ro_d1[j]=0.0;
}

//concentration at redundant lattice points
ro_D_ADPO[0]=0.0;
ro_D_ADPO[xSteps+2]=0.0;
ro_E0[0]=0.0;
ro_E0[xSteps+2]=0.0;
ro_D_ATPO[0]=0.0;
ro_D_ATPO[xSteps+2]=0.0;

ReadFile<<"#<<"x "<<"minD_ADP "<<"minE "<<"minD_ATP "<<"mind "<<"minde
"<<endl;
ReadFile2<<"#<<"minD_total "<<"minE_total "<<"minD_surface
"<<"minE_surface"<<endl;
// checking the initial distribution and total molecule conservation and
writing in files
double total_D=0.0, total_E=0.0, minD_total, minE_total, minD_surface,
minE_surface;
for(int j=1; j<=xSteps+1;j++)
{
    total_D+=ro_D_ADPO[j]+ro_D_ATPO[j]+ro_d0[j]+ro_de0[j];
    total_E+=ro_E0[j]+ro_de0[j];
    minD_total=ro_D_ADPO[j]+ro_D_ATPO[j]+ro_d0[j]+ro_de0[j];
    minE_total=ro_E0[j]+ro_de0[j];
    minD_surface=ro_d0[j]+ro_de0[j];
    minE_surface=ro_de0[j];
}

```

```

        ReadFile<<dx*j<<' '<<ro_D_ADPO[j]<<' '<<ro_E0[j]<<'
'<<ro_D_ATPO[j]<<' '<<ro_d0[j]<<' '<<ro_de0[j]<<endl;
        ReadFile2<<dx*j<<' '<<minD_total<<' '<<minE_total<<'
'<<minD_surface<<' '<<minE_surface<<endl;
    }

    ReadFile<<" "<<endl;
    ReadFile<<" "<<endl;
    ReadFile<<" "<<endl;

    ReadFile2<<" "<<endl;
    ReadFile2<<" "<<endl;
    ReadFile2<<" "<<endl;

    ReadFile1<<<<' '<<total_D<<' '<<total_E<<endl;

    //array to compute average value of proteins at different lattice points
    double avg_minD_total[xSteps+2] = {0.0}, avg_minE_total[xSteps+2] = {0.0},
    avg_minD_surface[xSteps+2] = {0.0}, avg_minE_surface[xSteps+2] = {0.0};
    int count = 0;
    double free_time_minD[xSteps+2] = {0.0}, free_time_minE[xSteps+2] = {0.0};

    for(int i = 1; i<tSteps; i++)
    {

        for(int j=1; j<=xSteps+1; j++)
        {

            //Wingreen's reaction diffusion equations
            ro_D_ADPO[j] = ro_D_ADPO[j] + dt*D_D*lap(j, xSteps, ro_D_ADPO[j-
1], ro_D_ADPO[j], ro_D_ADPO[j+1]) - dt*sg_D_ADP_ATP*ro_D_ADPO[j] +
dt*sg_de*ro_de0[j];
            ro_E1[j] = ro_E0[j] + dt*D_E*lap(j, xSteps, ro_E0[j-1], ro_E0[j],
ro_E0[j+1]) - dt*sg_E*ro_d0[j]*ro_E0[j] + dt*sg_de*ro_de0[j];
            ro_D_ATPO[j] = ro_D_ATPO[j] + dt*D_D*lap(j, xSteps, ro_D_ATPO[j-
1], ro_D_ATPO[j], ro_D_ATPO[j+1]) + dt*sg_D_ADP_ATP*ro_D_ADPO[j] -
dt*sg_D*ro_D_ATPO[j] - dt*sg_dD*(ro_d0[j]+ro_de0[j])*ro_D_ATPO[j];
            ro_d1[j]=ro_d0[j] + dt*sg_D*ro_D_ATPO[j] -
dt*sg_E*ro_d0[j]*ro_E0[j] + dt*sg_dD*(ro_d0[j]+ro_de0[j])*ro_D_ATPO[j];
            ro_del1[j]=ro_de0[j] + dt*sg_E*ro_d0[j]*ro_E0[j] -
dt*sg_de*ro_de0[j];

        }

        //cout<<"#####"<<endl;

        for(int j=1; j<=xSteps+1; j++)
        {
            ro_D_ADPO[j]=ro_D_ADPO1[j];
            ro_E0[j]=ro_E1[j];
            ro_D_ATPO[j]=ro_D_ATPO1[j];
            ro_d0[j]=ro_d1[j];
            ro_de0[j]=ro_del1[j];
        }
    }
}

```

```

    }

    total_D=0.0;
    total_E=0.0;
    if(i%10000==0)
    {
        cout<<i/10000<<endl;
        for(int j=1; j<=xSteps+1; j++)
        {
            total_D+=ro_D_ADPO[j]+ro_D_ATPO[j]+ro_d0[j]+ro_de0[j];
            total_E+=ro_E0[j]+ro_de0[j];

            minD_total=ro_D_ADPO[j]+ro_D_ATPO[j]+ro_d0[j]+ro_de0[j];
            minE_total=ro_E0[j]+ro_de0[j];
            minD_surface=ro_d0[j]+ro_de0[j];
            minE_surface=ro_de0[j];

            ReadFile<<dx*j<<' '<<ro_D_ADPO[j]<<' '<<ro_E0[j]<<'
'<<ro_D_ATPO[j]<<' '<<ro_d0[j]<<' '<<ro_de0[j]<<endl;
            ReadFile2<<dx*j<<' '<<minD_total<<' '<<minE_total<<'
'<<minD_surface<<' '<<minE_surface<<endl;

            if(count>10000)
            {
                avg_minD_total[j]+=minD_total;
                avg_minE_total[j]+=minE_total;
                avg_minD_surface[j]+=minD_surface;
                avg_minE_surface[j]+=minE_surface;
            }

        }

        count++;

        //storing total protein (to check conservation)
        ReadFile1<<i<<' '<<total_D<<' '<<total_E<<'
'<<total_D+total_E<<endl;

        //cout<<endl;

        ReadFile<<" "<<endl;
        ReadFile<<" "<<endl;
        ReadFile<<" "<<endl;

        ReadFile2<<" "<<endl;
        ReadFile2<<" "<<endl;
        ReadFile2<<" "<<endl;
    }
}

ReadFile3<<"#x"<<"minD_total "<<"minE_total "<<"minD_surface
"<<"minE_surface"<<endl;
for(int j=1; j<=xSteps+1; j++)
{
    //storing time average at different x

```

```

        ReadFile3<<dx*j<< ' '<<avg_minD_total[j]/double(count-10000)<<'
'<<avg_minE_total[j]/(count-10000)<<' '<<avg_minD_surface[j]/double(count-
10000)<<' '<<avg_minE_surface[j]/double(count-10000)<<endl;

    }

    cout<<"sD = "<<sg_D<<' '<<"sdD = "<<sg_dD<<' '<<"sde = "<<sg_de<<' '<<"sE
="<<sg_E<<endl;

    return 0;
}

```

%Function to calculate Pearson correlation between sisters
written in MATLAB written by Harsh vashistha

```
function [in,corr,Err]=PC(Vars,range)

for i=1:length(Vars)

sizes(i)=length(Vars{i});

end
Maximum=max(sizes);

%Putting them together
for j=1:length( Vars)
for i=1:length( Vars{j})
Al(i,2*j-1)= Vars{j}(i,1);
Al(i,2*j)= Vars{j}(i,2);
end
Al(i+1:Maximum,2*j-1)= nan;
Al(i+1:Maximum,2*j)= nan;

end

%This part calculates Pearson correlation point by point
for i=1:range
k=1;
for j=1:length(Vars)
if ~isnan(Al(i,(2*j)-1))
A(k)= Al(i,(2*j)-1);
B(k)= Al(i,2*j);
k=k+1;
end
end
R = corrcoef(A,B);
coeff=R(1,2);
PC(i+1,1)=coeff;
SEPC(i+1,1)=((1- (PC(i+1)*PC(i+1))))/sqrt((k));
gen(i+1,1)=i;

clearvars -except Vars PC SEPC i range Al gen dest
end
PC(1,1)=1;
```

```

SEPC(1,1)=0;
gen(1,1)=0;
corr=PC;
Err=SEPC;
in=gen;

```

```
end
```

```
%Function to separate cell cycles
```

```
function[WAT WA NTA NLA]= windowcreate(timeA,LengthA)
```

```

[nn,mm] = size(LengthA);
ee = 1;
ss = 0;
jj = 1;

```

```
%Find WA
```

```

nl = 1;
newtimeA(1)= timeA(1);
newlengthA(1)= LengthA(1);
for ii = 1:nn-1
    if 0.7*LengthA(ii) > LengthA(ii+1)
        newtimeA(nl+1)=timeA(ii+1);
        newlengthA(nl+1)= LengthA(ii+1);
        nl=nl+1;
        for kk = ss+1:ii
            WA(jj,ee) = LengthA(kk);
            WAT(jj,ee) = timeA(kk);

            jj = jj +1;
        end
        ee = ee + 1;
        ss = ii;
        jj = 1;
    end

```

```
end
```

```
end
```

```

last = 0;
[HH,GG] = size(WA);

```

```
%Add the last cycle to WA
```

```

for EE = 1:GG
    for DD = 1:HH
        if WA(DD,EE) ~= 0
            last = WA(DD,EE);
        end
    end
end

t = 1;

for YY = 1:nn
    if LengthA(YY) == last
        for kk = YY+1:nn
            WA(jj,ee) = LengthA(kk);
            WAT(jj,ee) = timeA(kk);
            jj = jj + 1;
        end
        ee = ee + 1;
        jj = 1;
    end
end

NTA=newtimeA;
NLA= newlengthA;

end

```

Bibliography

1. Hodgkin, A. L. & Huxley, A. F. A quantitative description of membrane current and its application to conduction and excitation in nerve. *J. Physiol.* **117**, 500–544 (1952).
2. El Hady, A. & Machta, B. B. Mechanical surface waves accompany action potential propagation. *Nat. Commun.* **6**, 1–7 (2015).
3. López-Maury, L., Marguerat, S. & Bähler, J. Tuning gene expression to changing environments: From rapid responses to evolutionary adaptation. *Nature Reviews Genetics* vol. 9 583–593 (2008).
4. Freddolino, P. L., Yang, J., Momen-Roknabadi, A. & Tavazoie, S. Stochastic tuning of gene expression enables cellular adaptation in the absence of pre-existing regulatory circuitry. *Elife* **7**, (2018).
5. Gómez-Schiavon, M. & Buchler, N. E. Epigenetic switching as a strategy for quick adaptation while attenuating biochemical noise. *PLoS Comput. Biol.* **15**, e1007364 (2019).
6. Mitchison, T. & Kirschner, M. Dynamic instability of microtubule growth. *Nature* **312**, 237–242 (1984).
7. Desai, A. & Mitchison, T. J. Microtubule polymerization dynamics. *Annual Review of Cell and Developmental Biology* vol. 13 83–117 (1997).
8. Fygenson, D. K., Braun, E. & Libchaber, A. Phase diagram of microtubules. *Phys. Rev. E* **50**, 1579–1588 (1994).
9. Gorbsky, G. J., Sammak, P. J. & Borisy, G. G. Microtubule dynamics and chromosome motion visualized in living anaphase cells. *J. Cell Biol.* **106**, 1185–1192 (1988).
10. Alberts, B. *et al.* Molecular Biology of the Cell - NCBI Bookshelf. *Amino Acids* vol. 54 1392 (2007).
11. Adam, M., Murali, B., Glenn, N. O. & Potter, S. S. Epigenetic inheritance based evolution of antibiotic resistance in bacteria. *BMC Evol. Biol.* **8**, 1–12 (2008).
12. Sun, Y. H., Chen, S. P., Wang, Y. P., Hu, W. & Zhu, Z. Y. Cytoplasmic impact on cross-genus cloned fish derived from transgenic common carp (*Cyprinus carpio*) nuclei and goldfish (*Carassius auratus*) enucleated eggs. *Biol. Reprod.* **72**, 510–515 (2005).
13. Bolotin, E. & Hershberg, R. Bacterial intra-species gene loss occurs in a largely clocklike manner mostly within a pool of less conserved and constrained genes. *Sci. Rep.* **6**, 1–9 (2016).

14. Rosche, W. A. & Foster, P. L. Determining mutation rates in bacterial populations. *Methods* **20**, 4–17 (2000).
15. Stewart, F. M., Gordon, D. M. & Levin, B. R. Fluctuation analysis: The probability distribution of the number of mutants under different conditions. *Genetics* **124**, 175–185 (1990).
16. Huh, D. & Paulsson, J. Non-genetic heterogeneity from stochastic partitioning at cell division. *Nature Genetics* vol. 43 95–100 (2011).
17. Avery, S. V. Microbial cell individuality and the underlying sources of heterogeneity. *Nature Reviews Microbiology* (2006) doi:10.1038/nrmicro1460.
18. Van Boxtel, C., Van Heerden, J. H., Nordholt, N., Schmidt, P. & Bruggeman, F. J. Taking chances and making mistakes: Non-genetic phenotypic heterogeneity and its consequences for surviving in dynamic environments. *Journal of the Royal Society Interface* vol. 14 (2017).
19. Bergmiller, T. *et al.* Biased partitioning of the multidrug efflux pump AcrAB-TolC underlies long-lived phenotypic heterogeneity. *Science* (80-.). **356**, 311–315 (2017).
20. Spudich, J. L. & Koshland, D. E. Non-genetic individuality: Chance in the single cell. *Nature* vol. 262 467–471 (1976).
21. Mcadams, H. H. & Arkin, A. Stochastic mechanisms in gene expression. *Proc. Natl. Acad. Sci. U. S. A.* **94**, 814–819 (1997).
22. Stewart, E. J., Madden, R., Paul, G. & Taddei, F. Aging and death in an organism that reproduces by morphologically symmetric division. *PLoS Biol.* **3**, 0295–0300 (2005).
23. Ram, Y. *et al.* Predicting microbial growth in a mixed culture from growth curve data. *Proc. Natl. Acad. Sci. U. S. A.* **116**, 14698–14707 (2019).
24. Wang, P. *et al.* Robust growth of escherichia coli. *Curr. Biol.* (2010) doi:10.1016/j.cub.2010.04.045.
25. Susman, L. *et al.* Individuality and slow dynamics in bacterial growth homeostasis. *Proc. Natl. Acad. Sci. U. S. A.* **115**, (2018).
26. Taheri-Araghi, S. *et al.* Cell-size control and homeostasis in bacteria. *Curr. Biol.* (2015) doi:10.1016/j.cub.2014.12.009.
27. Amir, A. Cell size regulation in bacteria. *Phys. Rev. Lett.* (2014) doi:10.1103/PhysRevLett.112.208102.
28. Ho, P. Y., Lin, J. & Amir, A. Modeling Cell Size Regulation: From Single-Cell-Level Statistics to Molecular Mechanisms and Population-Level Effects. *Annual Review of Biophysics* (2018) doi:10.1146/annurev-biophys-070317-032955.

29. Vashistha, H., Kohram, M. & Salman, H. Non-genetic inheritance restraint of cell-to-cell variation. *Elife* **10**, 1–21 (2021).
30. Wisser, M. J., Ribeck, N. & Lenski, R. E. Long-term dynamics of adaptation in asexual populations. *Science* (80-.). **342**, 1364–1367 (2013).
31. Scheuerl, T. *et al.* Bacterial adaptation is constrained in complex communities. *Nat. Commun.* **11**, 1–8 (2020).
32. Stern, S., Dror, T., Stolovicki, E., Brenner, N. & Braun, E. Genome-wide transcriptional plasticity underlies cellular adaptation to novel challenge. *Mol. Syst. Biol.* **3**, 106 (2007).
33. Katzir, Y., Stolovicki, E., Stern, S. & Braun, E. Cellular Plasticity Enables Adaptation to Unforeseen Cell-Cycle Rewiring Challenges. *PLoS One* **7**, e45184 (2012).
34. Facchetti, G., Chang, F. & Howard, M. Controlling cell size through sizer mechanisms. *Current Opinion in Systems Biology* vol. 5 86–92 (2017).
35. Si, F. *et al.* Mechanistic Origin of Cell-Size Control and Homeostasis in Bacteria. *Curr. Biol.* **29**, 1760-1770.e7 (2019).
36. Si, F. *et al.* Mechanistic Origin of Cell-Size Control and Homeostasis in Bacteria. *Curr. Biol.* **29**, 1760-1770.e7 (2019).
37. Teather, R. M., Collins, J. F. & Donachie, W. D. Quantal behavior of a diffusible factor which initiates septum formation at potential division sites in *Escherichia coli*. *J. Bacteriol.* **118**, 407–413 (1974).
38. Bi, E. & Lutkenhaus, J. FtsZ regulates frequency of cell division in *Escherichia coli*. *J. Bacteriol.* **172**, 2765–2768 (1990).
39. Lutkenhaus, J. & Addinall, S. G. Bacterial cell division and the Z ring. *Annu. Rev. Biochem.* **66**, 93–116 (1997).
40. Bi, E. & Lutkenhaus, J. FtsZ ring structure associated with division in *Escherichia coli*. *Nature* **354**, 161–164 (1991).
41. Dai, K. & Lutkenhaus, J. *ftsZ* Is an essential cell division gene in *Escherichia coli*. *J. Bacteriol.* **173**, 3500–3506 (1991).
42. Tétart, F. & Bouché, J. -P. Regulation of the expression of the cell-cycle gene *ftsZ* by DicF antisense RNA. Division does not require a fixed number of FtsZ molecules. *Mol. Microbiol.* **6**, 615–620 (1992).
43. Raskin, D. M. & De Boer, P. A. J. Rapid pole-to-pole oscillation of a protein required for directing division to the middle of *Escherichia coli*. *Proc. Natl. Acad. Sci. U. S. A.* **96**, 4971–4976 (1999).

44. Huang, K. C., Meir, Y. & Wingreen, N. S. Dynamic structures in *Escherichia coli*: Spontaneous formation of MinE rings and MinD polar zones. *Proc. Natl. Acad. Sci. U. S. A.* (2003) doi:10.1073/pnas.2135445100.
45. Raskin, D. M. & De Boer, P. A. J. The MinE ring: An FtsZ-independent cell structure required for selection of the correct division site in *E. coli*. *Cell* **91**, 685–694 (1997).
46. Lutkenhaus, J. Assembly Dynamics of the Bacterial MinCDE System and Spatial Regulation of the Z Ring. *Annu. Rev. Biochem.* **76**, 539–562 (2007).
47. Kretschmer, S., Ganzinger, K. A., Franquelim, H. G. & Schwille, P. Synthetic cell division via membrane-transforming molecular assemblies. *BMC Biology* vol. 17 1–10 (2019).
48. Ramm, B., Heermann, T. & Schwille, P. The *E. coli* MinCDE system in the regulation of protein patterns and gradients. *Cellular and Molecular Life Sciences* vol. 76 4245–4273 (2019).
49. Howard, M., Rutenberg, A. D. & De Vet, S. Dynamic compartmentalization of bacteria: Accurate division in *E. coli*. *Phys. Rev. Lett.* **87**, 2781021–2781024 (2001).
50. Wu, F., van Schie, B. G. C., Keymer, J. E. & Dekker, C. Symmetry and scale orient Min protein patterns in shaped bacterial sculptures. *Nat. Nanotechnol.* **10**, 719–726 (2015).
51. Moseley, J. B. & Nurse, P. Cell Division Intersects with Cell Geometry. *Cell* vol. 142 189–193 (2010).
52. Hu, J. *et al.* Portable microfluidic and smartphone-based devices for monitoring of cardiovascular diseases at the point of care. *Biotechnology Advances* vol. 34 305–320 (2016).
53. Rashid, S. *et al.* Adjustment in tumbling rates improves bacterial chemotaxis on obstacle-laden terrains. *Proc. Natl. Acad. Sci. U. S. A.* **116**, (2019).
54. Livak-Dahl, E., Sinn, I. & Burns, M. Microfluidic chemical analysis systems. *Annual Review of Chemical and Biomolecular Engineering* vol. 2 325–353 (2011).
55. Bišová, K. & Zachleder, V. Cell-cycle regulation in green algae dividing by multiple fission. *Journal of Experimental Botany* (2014) doi:10.1093/jxb/ert466.
56. Mata, A., Fleischman, A. J. & Roy, S. Characterization of Polydimethylsiloxane (PDMS) Properties for Biomedical Micro/Nanosystems. *Biomed. Microdevices* **7**, 281–293 (2005).
57. Toepke, M. W. & Beebe, D. J. PDMS absorption of small molecules and consequences in microfluidic applications. *Lab on a Chip* vol. 6 1484–1486 (2006).
58. Jenkins, G. Rapid prototyping of PDMS devices using su-8 lithography. *Methods Mol. Biol.* (2013) doi:10.1007/978-1-62703-134-9_11.

59. Rodrigo Martinez-Duarte and Marc J. Madou. *Microfluidics and Nanofluidics Handbook*. *Microfluidics and Nanofluidics Handbook* (CRC Press, 2016). doi:10.1201/b11188.
60. Rohm and Haas Electronic Materials. Microposit S1800 G2 Series Photoresists. *Data Sheet* 1–6 (2006).
61. Epoxy, P. & Photoresist, N. SU-8 2000 Permanent Epoxy Negative Photoresist PROCESSING GUIDELINES FOR : *Exposure* (2000).
62. Lutz, R. & Bujard, H. Independent and tight regulation of transcriptional units in escherichia coli via the LacR/O, the TetR/O and AraC/I1-I2 regulatory elements. *Nucleic Acids Res.* (1997) doi:10.1093/nar/25.6.1203.
63. Paintdakhi, A. *et al.* Oufiti: An integrated software package for high-accuracy, high-throughput quantitative microscopy analysis. *Mol. Microbiol.* (2016) doi:10.1111/mmi.13264.
64. Lambert, G. & Kussell, E. Memory and Fitness Optimization of Bacteria under Fluctuating Environments. *PLoS Genet.* **10**, e1004556 (2014).
65. Robert, L. *et al.* Pre-dispositions and epigenetic inheritance in the Escherichia coli lactose operon bistable switch. *Mol. Syst. Biol.* (2010) doi:10.1038/msb.2010.12.
66. Casadesus, J. & Low, D. Epigenetic Gene Regulation in the Bacterial World. *Microbiol. Mol. Biol. Rev.* (2006) doi:10.1128/mmbr.00016-06.
67. Chen, C. *et al.* Convergence of DNA methylation and phosphorothioation epigenetics in bacterial genomes. *Proc. Natl. Acad. Sci. U. S. A.* (2017) doi:10.1073/pnas.1702450114.
68. Turnbough, C. L. Regulation of Bacterial Gene Expression by Transcription Attenuation. *Microbiol. Mol. Biol. Rev.* (2019) doi:10.1128/mmbr.00019-19.
69. Bryant, J., Chewapreecha, C. & Bentley, S. D. Developing insights into the mechanisms of evolution of bacterial pathogens from whole-genome sequences. *Future Microbiology* (2012) doi:10.2217/fmb.12.108.
70. Robert, L. *et al.* Mutation dynamics and fitness effects followed in single cells. *Science* (80- .). (2018) doi:10.1126/science.aan0797.
71. Casadesús, J. & Low, D. A. Programmed heterogeneity: Epigenetic mechanisms in bacteria. *Journal of Biological Chemistry* (2013) doi:10.1074/jbc.R113.472274.
72. Huh, D. & Paulsson, J. Non-genetic heterogeneity from stochastic partitioning at cell division. *Nature Genetics* (2011) doi:10.1038/ng.729.
73. Norman, T. M., Lord, N. D., Paulsson, J. & Losick, R. Memory and modularity in cell-fate decision making. *Nature* **503**, 481–486 (2013).

74. Veening, J.-W. *et al.* Bet-hedging and epigenetic inheritance in bacterial cell development. *Proc. Natl. Acad. Sci.* **105**, 4393–4398 (2008).
75. Ackermann, M. A functional perspective on phenotypic heterogeneity in microorganisms. *Nature Reviews Microbiology* (2015) doi:10.1038/nrmicro3491.
76. Elowitz, M. B., Levine, A. J., Siggia, E. D. & Swain, P. S. Stochastic gene expression in a single cell. *Science* (80-.). (2002) doi:10.1126/science.1070919.
77. Govers, S. K., Adam, A., Blockeel, H. & Aertsen, A. Rapid phenotypic individualization of bacterial sister cells. *Sci. Rep.* **7**, 8473 (2017).
78. Chai, Y., Norman, T., Kolter, R. & Losick, R. An epigenetic switch governing daughter cell separation in *Bacillus subtilis*. *Genes Dev.* (2010) doi:10.1101/gad.1915010.
79. Sandler, O. *et al.* Lineage correlations of single cell division time as a probe of cell-cycle dynamics. *Nature* (2015) doi:10.1038/nature14318.
80. Mosheiff, N. *et al.* Inheritance of Cell-Cycle Duration in the Presence of Periodic Forcing. *Phys. Rev. X* (2018) doi:10.1103/PhysRevX.8.021035.
81. Wakamoto, Y., Ramsden, J. & Yasuda, K. Single-cell growth and division dynamics showing epigenetic correlations. *Analyst* **130**, 311–317 (2005).
82. Brenner, N. *et al.* Single-cell protein dynamics reproduce universal fluctuations in cell populations. *Eur. Phys. J. E. Soft Matter* **38**, 102 (2015).
83. Tanouchi, Y. *et al.* A noisy linear map underlies oscillations in cell size and gene expression in bacteria. *Nature* (2015) doi:10.1038/nature14562.
84. Yang, D., Jennings, A. D., Borrego, E., Retterer, S. T. & Männik, J. Analysis of Factors Limiting Bacterial Growth in PDMS Mother Machine Devices. *Front. Microbiol.* **9**, 871 (2018).
85. Kohram, M., Vashistha, H., Leibler, S., Xue, B. & Salman, H. Bacterial Growth Control Mechanisms Inferred from Multivariate Statistical Analysis of Single-Cell Measurements. *Curr. Biol.* (2020) doi:https://doi.org/10.1016/j.cub.2020.11.063.
86. Godin, M. *et al.* Using buoyant mass to measure the growth of single cells. *Nat. Methods* (2010) doi:10.1038/nmeth.1452.
87. Soifer, I., Robert, L. & Amir, A. Single-cell analysis of growth in budding yeast and bacteria reveals a common size regulation strategy. *Curr. Biol.* (2016) doi:10.1016/j.cub.2015.11.067.
88. Nordholt, N., van Heerden, J. H. & Bruggeman, F. J. Biphasic Cell-Size and Growth-Rate Homeostasis by Single *Bacillus subtilis* Cells. *Curr. Biol.* **30**, 2238–2247.e5 (2020).

89. David, L., Stolovicki, E., Haziz, E. & Braun, E. Inherited adaptation of genome-rewired cells in response to a challenging environment. <http://dx.doi.org/10.2976/1.3353782> **4**, 131–141 (2010).
90. Zhu, Z. *et al.* Entropy of a bacterial stress response is a generalizable predictor for fitness and antibiotic sensitivity. *Nat. Commun.* 2020 **11**, 1–15 (2020).
91. Monds, R. D. *et al.* Systematic Perturbation of Cytoskeletal Function Reveals a Linear Scaling Relationship between Cell Geometry and Fitness. *Cell Rep.* **9**, 1528–1537 (2014).
92. Cullum, J. & Vicente, M. Cell growth and length distribution in *Escherichia coli*. *J. Bacteriol.* **134**, 330–337 (1978).
93. Xiao, J. & Goley, E. D. Redefining the roles of the FtsZ-ring in bacterial cytokinesis. *Curr. Opin. Microbiol.* **34**, 90–96 (2016).
94. Stricker, J., Maddox, P., Salmon, E. D. & Erickson, H. P. Rapid assembly dynamics of the *Escherichia coli* FtsZ-ring demonstrated by fluorescence recovery after photobleaching. *Proc. Natl. Acad. Sci.* **99**, 3171–3175 (2002).
95. Loose, M., Fischer-Friedrich, E., Ries, J., Kruse, K. & Schwille, P. Spatial Regulators for Bacterial Cell Division Self-Organize into Surface Waves in Vitro. *Science (80-.)*. **320**, 789–792 (2008).
96. de Boer, P. A. J., Crossley, R. E. & Rothfield, L. I. A division inhibitor and a topological specificity factor coded for by the minicell locus determine proper placement of the division septum in *E. coli*. *Cell* **56**, 641–649 (1989).
97. Hale, C. A. Dynamic localization cycle of the cell division regulator MinE in *Escherichia coli*. *EMBO J.* **20**, 1563–1572 (2001).
98. Zieske, K. & Schwille, P. Reconstitution of self-organizing protein gradients as spatial cues in cell-free systems. *Elife* **3**, (2014).
99. Jia, S. *et al.* Effect of the Min system on timing of cell division in *Escherichia coli*. *PLoS One* **9**, 103863 (2014).
100. Moore, D. A., Whatley, Z. N., Joshi, C. P., Osawa, M. & Erickson, H. P. Probing for binding regions of the FtsZ protein surface through site-directed insertions: Discovery of fully functional FtsZ-fluorescent proteins. *J. Bacteriol.* **199**, (2017).
101. Wiedenmann, J. *et al.* EosFP, a fluorescent marker protein with UV-inducible green-to-red fluorescence conversion. *Proc. Natl. Acad. Sci.* **101**, 15905–15910 (2004).
102. Weart, R. B. & Levin, P. A. Growth rate-dependent regulation of medial FtsZ ring formation. *J. Bacteriol.* **185**, 2826–2834 (2003).
103. Wehrens, M. *et al.* Size Laws and Division Ring Dynamics in Filamentous *Escherichia coli*

- cells. *Curr. Biol.* **28**, 972-979.e5 (2018).
104. Vecchiarelli, A., Li, M., Mizuuchi, M., Ivanov, V. & Mizuuchi, K. MinE recruits, stabilizes, releases, and inhibits MinD interactions with membrane to drive oscillation. *bioRxiv* 109637 (2017) doi:10.1101/109637.
 105. Stricker, J., Maddox, P., Salmon, E. D. & Erickson, H. P. Rapid assembly dynamics of the Escherichia coli FtsZ-ring demonstrated by fluorescence recovery after photobleaching. *Proc. Natl. Acad. Sci.* **99**, 3171–3175 (2002).
 106. Bisson-Filho, A. W. *et al.* Treadmilling by FtsZ filaments drives peptidoglycan synthesis and bacterial cell division. *Science (80-.)*. **355**, 739–743 (2017).
 107. Walker, B. E., Männik, J. & Männik, J. Transient Membrane-Linked FtsZ Assemblies Precede Z-Ring Formation in Escherichia coli. *Curr. Biol.* **30**, 499-508.e6 (2020).